High-throughput Designing of Magnetic Antiperovskites for Multifunctional Applications

Zur Erlangung des Grades eines Doktors der Naturwissenschaften (Dr. rer. nat.)
Genehmigte Dissertation von Harish Kumar Singh aus Khekra, Uttar Pradesh, Indien
Tag der Einreichung: July 25, 2023, Tag der Prüfung: October 24, 2023

1. Gutachten: Prof. Dr. Oliver Gutfleisch
2. Gutachten: PD Dr. Manuel Richter
3. Gutachten: Prof. Dr. Karsten Albe
4. Gutachten: Prof. Dr. Christina Birkel
Darmstadt, Technische Universität Darmstadt

TECHNISCHE
UNIVERSITÄT
DARMSTADT

Materials and Earth
Sciences Department

Institute of Materials
Science

High-throughput Designing of Magnetic Antiperovskites for Multifunctional Applications

Accepted doctoral thesis by Harish Kumar Singh

1. Review: Prof. Dr. Oliver Gutfleisch
2. Review: PD Dr. Manuel Richter
3. Review: Prof. Dr. Karsten Albe
4. Review: Prof. Dr. Christina Birkel

Date of submission: July 25, 2023
Date of thesis defense: October 24, 2023

Darmstadt, Technische Universität Darmstadt

Bitte zitieren Sie dieses Dokument als:
URN: urn:nbn:de:tuda-tuprints-247758
URL: http://tuprints.ulb.tu-darmstadt.de/24775
Jahr der Veröffentlichung der Dissertation auf TUprints: 2024

Erklärungen laut Promotionsordnung

§8 Abs. 1 lit. c PromO

Ich versichere hiermit, dass die elektronische Version meiner Dissertation mit der schriftlichen Version übereinstimmt.

§8 Abs. 1 lit. d PromO

Ich versichere hiermit, dass zu einem vorherigen Zeitpunkt noch keine Promotion versucht wurde. In diesem Fall sind nähere Angaben über Zeitpunkt, Hochschule, Dissertationsthema und Ergebnis dieses Versuchs mitzuteilen.

§9 Abs. 1 PromO

Ich versichere hiermit, dass die vorliegende Dissertation selbstständig und nur unter Verwendung der angegebenen Quellen verfasst wurde.

§9 Abs. 2 PromO

Die Arbeit hat bisher noch nicht zu Prüfungszwecken gedient.

Darmstadt, July 25, 2023

Harish Kumar Singh

Contents

Abstract

Antiperovskite (AP) materials exhibit various interesting physical properties and have been investigated for various technological applications, including spintronics, superconductivity, and energy storage. Antiperovskites (APs) have a cubic structure that is similar to perovskites, but with an inverted arrangement of anions and cations. Despite their potential, the AP family is not as robust as perovskites, and there is still much to be understood about their stability and magnetic properties. Motivated by the intriguing magnetic properties of AP compounds, the main objective of this thesis was to explore these magnetic multifunctional phenomena in existing AP compounds and in newly predicted AP compounds.

First objective of our study was to predict new magnetic APs with magnetic elements (Cr, Mn, Fe, Co, and Ni) as M in the chemical formula M_3XZ, where X is C and N, and Z are elements from Li to Bi except noble gases and 4f rare-earth metals. To achieve this, we considered three stability criteria: thermodynamic, mechanical, and dynamical. We conducted a high-throughput screening for 630 APs and evaluated their stabilities using density functional theory (DFT) calculations. Our analysis resulted in the prediction of 11 new magnetic APs that fulfilled all three stability criteria. Additionally, we verified the stabilities of 76 experimentally known APs.

AP compounds have been reported to display various magnetic structures such as non-collinear (Γ_{4g} and Γ_{5g} configurations, represented by irreducible notations) antiferromagnetic (AFM), collinear AFM, and ferromagnetic (FM) structures. Therefore, it is necessary to know their magnetic ground state before determining their magnetic properties. We analyzed the magnetic ground state for 54 APs, consisting of 11 newly predicted and 43 experimentally known magnetic APs, by considering seven magnetic configurations. Our analysis revealed that 15 AP compounds have either Γ_{4g} or Γ_{5g} non-collinear AFM as the lowest energy state. While a non-collinear structure was previously reported for Mn-based APs, our study found that Cr-based APs (Cr_3IrN and Cr_3PtN) also stabilized in the Γ_{4g} non-collinear AFM state. We also found that 6 APs exhibit a collinear AFM structure, and 33 APs stabilize in the FM ground state.

Next, we focused on non-collinear magnetic properties that are influenced by strong magnetostructural coupling, negative thermal expansion (NTE), and the piezomagnetic effect (PME). We investigated NTE phenomenon by analyzing the relative change in lattice constant ($\Delta a/a_0$) between the paramagnetic state and ordered AFM state. To obtain better agreement with experimentally observed ($\Delta a/a_0$), we propose the use of the PM state obtained based on the disordered local moment (DLM) approach, rather than using a non-magnetic state as a substitute for the PM state. We studied the PME of non-collinear AFM APs under compressive and tensile biaxial strains. In a few AP compounds, PME induces a phase transition between two non-collinear states $\Gamma_{4g} \leftrightarrow \Gamma_{5g}$ states.

At last, we analyzed the topological transport properties, including the anomalous Hall conductivity (AHC) and anomalous Nernst conductivity (ANC), for non-collinear AFM and FM APs. For the FM APs, the largest AHC and ANC of 1128 S/cm and 6.31 A/mK are obtained in Co_3LiN and Co_3PtN, respectively. In general, FM compounds exhibits a larger AHC and ANC than non-collinear AFM compounds. The large AHC and ANC originate due to the presence of Weyl points near the Fermi energy, as illustrated for Co_3PtN. Moreover, AHC can also be fine-tuned by tuning the energies of Weyl nodes by applying biaxial strain, as demonstrated in the case of Mn_3PdN.

Overall, this study sheds light on the validation of stability for experimentally known AP compounds and the prediction of new AP compounds. Furthermore, it investigates the magnetic properties of the stable magnetic APs, thus offering new insights for potential technological applications.

Zusammenfassung

Antiperovskit (AP)-Materialien weisen verschiedene interessante physikalische Eigenschaften auf und wurden für verschiedene technologische Anwendungen wie Spintronik, Supraleitung und Energiespeicherung untersucht. APs haben eine kubische Struktur, die der von Perovskiten ähnelt, jedoch mit einer invertierten Anordnung von Anionen und Kationen. Trotz ihres Potenzials ist die AP-Familie nicht so robust wie Perowskite, und ihre Stabilität und magnetischen Eigenschaften sind noch nicht vollstanding verstanden. Motiviert durch die faszinierenden magnetischen Eigenschaften von AP-Verbindungen bestand das Hauptziel dieser Arbeit darin, diese magnetischen multifunktionalen Phänomene in bestehenden AP-Verbindungen und neu vorhergesagten AP-Verbindungen zu erforschen.

Das erste Ziel unserer Studie war es, neue magnetische APs mit magnetischen Elementen (Cr, Mn, Fe, Co und Ni) als M in der chemischen Formel M_3XZ vorherzusagen, wobei X die Elemente C und N darstellt und Z die Elemente von Li bis Bi mit Ausnahme der Edelgase und der 4f-Seltenerdmetalle sind. Um dies zu erreichen, haben wir drei Stabilitätskriterien berücksichtigt: thermodynamische, mechanische und dynamische Stabilität. Wir führten ein Hochdurchsatz-Screening für 630 APs durch und bewerteten ihre Stabilität mithilfe von Dichtefunktionaltheorie (DFT)-Berechnungen. Unsere Analyse führte zur Vorhersage von 11 neuen magnetischen APs, die alle drei Stabilitätskriterien erfüllten. Darüber hinaus haben wir die Stabilität von 76 experimentell bekannten APs verifiziert.

Von AP-Verbindungen wurde berichtet, class sie verschiedene magnetische Strukturen aufweisen, wie beispielsweise nicht-kollineare (Γ_{4g} und Γ_{5g}-Konfigurationen, dargestellt durch irreduzible Notationen) antiferromagnetische (AFM), kollineare AFM- und ferromagnetische (FM) Strukturen. Daher ist es erforderlich, ihren magnetischen Grundzustand zu kennen, bevor ihre magnetischen Eigenschaften bestimmt werden können. Wir haben den magnetischen Grundzustand für 54 AP-Verbindungen analysiert, darunter 11 neu vorhergesagte und 43 experimentell bekannte magnetische APs, und dabei sieben magnetische Konfigurationen berücksichtigt. Unsere Analyse ergab, dass 15 AP-Verbindungen entweder den Γ_{4g} oder Γ_{5g} nicht-kollinearen AFM-Zustand als energetisch günstigsten Zustand aufweisen. Während eine nicht-kollineare Struktur zuvor für Mn-basierte APs berichtet wurde, zeigte unsere Studie, dass auch Cr-basierte APs (Cr_3IrN und Cr_3PtN) im

Γ_{4g} nicht-kollinearen AFM-Zustand stabil sind. Wir haben auch festgestellt, dass 6 APs eine kollineare AFM-Struktur aufweisen und 33 APs sich im FM-Grundzustand befinden.

Anschließend konzentrierten wir uns auf die nicht-kollinearen magnetischen Eigenschaften, die von einer starken magnetostrukturellen Kopplung, negativer thermischer Ausdehnung (NTE) und dem piezomagnetischen Effekt (PME) beeinflusst werden. Wir untersuchten das NTE-Phänomen, indem wir die relative Veränderung der Gitterkonstante ($\Delta a/a_0$) zwischen dem paramagnetischen Zustand und dem geordneten AFM-Zustand analysierten. Um eine bessere Übereinstimmung mit experimentell beobachteten ($\Delta a/a_0$)-Werten zu erzielen, schlagen wir vor, den PM-Zustand, der auf der Methode der ungeordneten lokalen Momente (DLM) basiert, anstelle eines nichtmagnetischen Zustands als Ersatz für den PM-Zustand zu verwenden. Wir untersuchten den PME von nicht-kollinearen AFM-APs unter Druck- und Zugbelastung. In einigen AP-Verbindungen löst der PME einen Phasenübergang zwischen den beiden nicht-kollinearen Zuständen $\Gamma_{4g} \leftrightarrow \Gamma_{5g}$ aus.

Zuletzt haben wir die topologischen Transporteigenschaften, einschließlich der anomalen Hall-Leitfähigkeit (AHC) und der anomalen Nernst-Leitfähigkeit (ANC), für nicht-kollineare AFM- und FM-APs analysiert. Bei den FM-APs wurden die größten AHC- und ANC-Werte von 1128 S/cm bzw. 6.31 A/mK in Co_3LiN bzw. Co_3PtN erzielt. Im Allgemeinen weisen FM-Verbindungen eine größere AHC und ANC auf als nicht-kollineare AFM-Verbindungen. Die hohe AHC und ANC sind auf das Vorhandensein von Weyl-Punkten in der Nähe der Fermi-Energie zurückzuführen, wie am Beispiel von Co_3PtN veranschaulicht wird. Darüber hinaus kann die AHC durch die Einstellung der Energien der Weyl-Knoten durch Anwendung von biaxialer Spannung feinabgestimmt werden, wie im Fall von Mn_3PdN demonstriert wird.

Insgesamt wirft diese Studie Licht auf die Validierung der Stabilität für experimentell bekannte AP-Verbindungen und die Vorhersage neuer AP-Verbindungen. Darüber hinaus untersucht sie die magnetischen Eigenschaften der stabilen magnetischen APs und bietet somit neue Erkenntnisse für potenzielle technologische Anwendungen.

Abbreviations

AP Antiperovskite

APs Antiperovskites

AFM Antiferromagnetic

AHC Anomalous Hall conductivity

ANC Anomalous Nernst conductivity

AHE Anomalous Hall effect

ANE Anomalous Nernst effect

cAFM Collinear antiferromagnetic

ΔE_h Convex hull distance

COHP Crystal Orbital Hamilton Population

DFT Density functional theory

DLM Disordered local moment

FM Ferromagnetic

E_f Formation energy

ICOHP Integrated crystal Orbital Hamilton Population

MVE Magneto-volume effect

MAE Magnetocrystalline anisotropy energy

ME Magnetoelectric

NM Non-magnetic

NTE Negative thermal expansion

PME Piezomagnetic effect

PM Paramagnetic

$\Delta a/a_0$ Relative change in lattice constant

SOC Spin-orbit coupling

Acknowledgments

I would like to express my gratitude to the examination members, Dr. Manuel Richter, Prof. Oliver Gutfleisch, Prof. Karsten Albe, and Prof. Christina Birkel, for being part of my Ph.D. examination committee. I thank them for their valuable time to grade my thesis work.

I would like to thank Ms. Maria Walker for providing all the official help and support in preparing the working contract and arranging the visa letter. She has been incredibly kind and helpful in everyday life, providing valuable suggestions and guidance that made a significant difference.

I would like to thank my colleagues: Dr. Ingo Opahle, Dr. Ilias Samathrakis, Nuno Miguel dos Santos Fortunato, Dr. Chen Shen, Dr. Qiang Gao, Dr. Teng Long, Dr. Ruiwen Xie, Dr. Ye Han, Dr. Jürgen Weischenberg, Dr. Tingting Lin, Dr. Xinru Li, Niloofar Hadaeghi, Yixuan Zhang, Mian Dai, Yaqian Guo, Amit Sehrawat, Shwetha Hegde, Ling Fan, and Marie Joëlle Charrier, for their valuable scientific discussions and collaborations. I am grateful for the friendly and supportive environment provided by them.

I would like to thank Dr. Manuel Richter for providing the funding to write my Ph.D. thesis and for his guidance and support throughout the thesis writing process.

I would also like to thank Ms. Grit Rötzer for providing official assistance in preparing the contract and helping me with general matters during my stay at IFW Dresden. I extend my thanks to Ms. Ulrike Nitzsche for her technical support. Furthermore, I extend my thanks to Prof. Jeroen van den Brink for granting me the opportunity to work at IFW Dresden and for providing financial support.

I would like to thank my funding sources, NOVAMAG, LOEWE Response Project, and the State of Hesse, for their support and funding, which made it possible to carry out my research thesis project and provided financial support for my salary. I would like to express my gratitude and acknowledge TU Darmstadt's Lichtenberg cluster for providing the high-performance supercomputer computational resources and facilities used in con-

ducting the calculations for this thesis project.

Last but not least, I would like to thank all my family members for their unwavering support and patience throughout my Ph.D. journey. Their encouragement and understanding have been invaluable in helping me complete this milestone.

Publications

First author

1. **Singh, Harish K.** *et al.* High-throughput screening of half-antiperovskites with a stacked kagome lattice: *Acta Materialia*, **2023**, 242, 118474.

2. **Singh, Harish K.** *et al.* Giant anomalous Hall and anomalous Nernst conductivities in antiperovskites and their tunability via magnetic fields: *Physical Review Materials*, **2022**, 5, 045402.

3. **Singh, Harish K.** *et al.* Multifunctional antiperovskites driven by strong magnetostructural coupling: *npj Computational Materials*, **2021**, 7, 98.

4. **Singh, Harish K.** *et al.* High-throughput screening of magnetic antiperovskites: *Chemistry of Materials*, **2018**, 30, 6983.

Contributing Author

5. Shen, Chen and Samathrakis, Ilias and Hu, Kun and **Singh, Harish K.** *et al.* Thermodynamical and topological properties of metastable Fe_3Sn: *npj Computational Materials*, **2022**, 8, 248.

6. Reitz, Andreas and Pazniak, Hanna and Shen, Chen and **Singh, Harish K.** *et al.* Cr_3GeN: A Nitride with Orthorhombic Antiperovskite Structure: *Chemistry of Materials*, **2022**, 34, 10304.

7. Samathrakis, Ilias and Fortunato, Nuno and **Singh, Harish K.** *et al.* Tunable anomalous Hall and Nernst effects in MM'X compounds: *Journal of Physics: Condensed Matter*, **2022**, 51, 025703.

8. Shen, Chen and Hadaeghi, Niloofar and **Singh, Harish K.** *et al.* Two-dimensional buckling structure induces the ultra-low thermal conductivity: a comparative study of the group GaX (X= N, P, As): *Journal of Materials Chemistry C*, **2022**, 4, 1436.

9. Johnson, F and Boldrin, D and Zemen, J and Pesquera, D and Kim, J and Moya, X and **Singh, Harish K.** *et al.* Strain dependence of Berry-phase-induced anomalous Hall effect in the non-collinear antiferromagnet Mn_3NiN: *Applied Physics Letters*, **2021**, 119, 22.

10. Samathrakis, Ilias and Long, Teng and Zhang, Zeying and **Singh, Harish K.** *et al.* Enhanced anomalous Nernst effects in ferromagnetic materials driven by Weyl nodes: *Journal of Physics D: Applied Physics*, **2021**, 55, 074003.

11. Sharma, Shalini and Zintler, Alexander and Günzing, Damian and Lill, Johanna and Meira, Debora Motta and Eilhardt, Robert and **Singh, Harish K.** *et al.* Epitaxy Induced Highly Ordered Sm_2Co_{17}–$SmCo_5$ Nanoscale Thin-Film Magnets: *ACS Applied Materials & Interfaces*, **2021**, 13, 32415.

12. Shen, Chen and Gao, Qiang and Fortunato, Nuno M and **Singh, Harish K.** *et al.* Designing of magnetic MAB phases for energy applications: *Journal of Materials Chemistry A*, **2021**, 9, 8805.

13. Ye, Xinglong and **Singh, Harish K.** *et al.* Giant voltage-induced modification of magnetism in micron-scale ferromagnetic metals by hydrogen charging: *Nature communications*, **2020**, 11, 4849.

14. Opahle, Ingo and **Singh, Harish K.** *et al.* Effect of N, C, and B interstitials on the structural and magnetic properties of alloys with Cu_3Au structure: *Physical Review Research*, **2020**, 2, 023134.

15. Chopra, Uday and Zeeshan, Mohd and Pandey, Shambhawi and Dhawan, Rakshanda and **Singh, Harish K.** *et al.* First-principles study of thermoelectric properties of Li-based Nowotony–Juza phases: *Journal of Physics: Condensed Matter*, **2019**, 31, 505504.

16. Ohmer, Dominik and Opahle, Ingo and **Singh, Harish K.** *et al.* Stability predictions of magnetic M_2AX compounds: *Journal of Physics: Condensed Matter*, **2019**, 31, 405902.

17. Ohmer, Dominik and Qiang, Gao and Opahle, Ingo and **Singh, Harish K.** *et al.* High-throughput design of 211-M_2AX compounds: *Physical Review Materials*, **2019**, 3, 053803.

18. Liang, Song-Mao and **Singh, Harish K.** *et al.* Phase equilibria of the Zn-Ti system: experiments, first-principles calculations and Calphad assessment: *Calphad*, **2019**, 64, 213.

1 Introduction

The first perovskite material, calcium titanate ($CaTiO_3$), was discovered by Gustav Rose in 1839 and as a tribute to the Russian mineralogist Count Lev Aleksevich von Perovski, Rose named the compound after him [118]. In 1934, F.R. Morral discovered the generalized cubic antiperovskite (AP) structure Fe_3AlC [109]. Thus, antiperovskites (APs) received their name due to the fact that they are electronic counterpart of the previously known perovskites. The APs constitute a diverse class of crystalline compounds. The most common structure of APs is cubic, with space group $Pm\bar{3}m$ (space group number 221). APs can be represented by the chemical formula M_3XZ and possess a cubic structure similar to perovskites, but with an inverted arrangement of anions (X and Z) and cations (M). In the cubic structure, the M atoms occupy the face-centered positions, while the X and Z atoms are located at the corners and in the body-centered position, respectively (Figure 4.1). However, other crystalline phases such as tetragonal [116, 20, 96, 163, 166, 97], orthorhombic [214, 20], and hexagonal phases [6] are also known.

Extensive research has been conducted on perovskite materials, while APs have not been explored to the same extent. However, in recent years, there has been a significant increase in the study of APs, as evidenced by the bar graph showing a rise in the number of publications (Figure 1.1). APs are versatile materials capable of accommodating various combinations of elements in their chemical formula. The substitution of different elements within the chemical formula results in distinct electronic and magnetic properties, making APs an intriguing subject of research in the field of materials science.

APs have recently garnered significant research interest due to their adaptable versatility and have been explored for various technological applications, including spintronics, superconductivity, and energy storage. Various interesting physical properties have been reported for both magnetic and non-magnetic AP materials. For instance, non-magnetic APs materials exhibit properties such as superconductivity [64, 189, 128], thermoelectric [98, 133], solid-state battery [211, 194], and topological insulator behavior [70, 77, 204]. For instance, Ni_3MgC is known as one of the oxygen-free superconductors with a perovskite structure, exhibiting a critical temperature of 8 K [64].

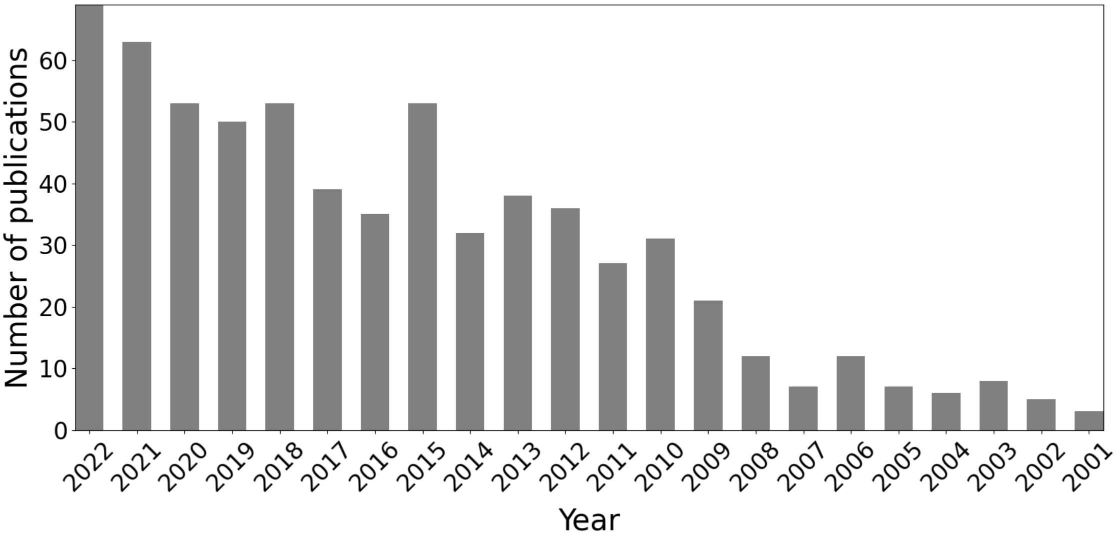

Figure 1.1: The number of manuscripts published on antiperovskites since the year 2000, based on data obtained from the Web of Science by searching the term “antiperovskite”) [187].

APs have been frequently studied as a new class of promising magnetic materials that exhibit a wide range of remarkable magnetic properties. These properties include the barocaloric effect [106], magnetocaloric effect [84, 85], magnetostriction [4, 148, 208], magnetoresistance [58, 91], spin-glass behavior [100, 153, 182], piezomagnetism [103], negative thermal expansion [170], anomalous Hall effect [135], and anomalous Nernst effect [212]. Intriguingly, the majority of research conducted thus far has primarily focused on investigating the magnetic properties of Mn-based magnetic antiperovskites [174], with research starting in the 1960s [142, 24]. In Mn-based APs, the positioning of Mn atoms at the face center plays a crucial role in generating these intriguing physical properties, resulting from the cooperative interplay between the degrees of freedom of the lattice, spin, and charge [91]. Particularly, this thesis focuses on exploring the magnetic properties of APs, which exhibit a wide range of intriguing magnetic phenomena. In the subsequent sections, detailed discussions are presented on several magnetic properties that are the subject of this thesis research.

1.1 Negative Thermal Expansion (NTE)

Positive thermal expansion (PTE) is a common property observed in most materials when they are heated. However, there are certain materials that demonstrate a counterintuitive phenomenon, known as negative thermal expansion (NTE), where the volume actually decreases instead of expanding with an increase in temperature. Thermal expansion is generally measured by the coefficient of linear or volume thermal expansion [5], $\alpha_L = (1/L_0)(\partial L/\partial T)$ or $\alpha_V = (1/V_0)(\partial V/\partial T)$. The coefficients α_L and α_V are commonly expressed in units of 10^{-6} K^{-1}, which corresponds to parts per million (ppm) K^{-1} or MKK^{-1}. For isotropic cubic materials, the coefficient α_V is equal to three times the coefficient α_L.

NTE materials have gained increasing attention due to their industrial merit and potential applications in various fields such as high-precision optics [42], cooker hobs [129], dental fillings [81], etc. NTE behavior has been reported across a wide range of materials for wide temperature ranges. Among them, Mn-based AP nitrides (Mn_3XN) are one of the most studied NTE materials [170]. These materials display a unique isotropic NTE behavior and undergo an AFM-to-PM transition, representing a transition from an ordered to a disordered phase.

The NTE properties of Mn_3XN (X = Ga, In, Ni, Zn, etc.) [170] were initially overlooked due to the presence of a sharp lattice contraction near the transition temperature. However, the potential for applications arises only if this sharp contraction can be broadened and made more continuous. Takenaka et al. found that controllable continuous NTE behavior for wide temperature ranges can be effectively achieved by doping the X-sites. As an example, in $Mn_3Zn_{1-x}Ge_xN$, doping Ge at Zn-sites (specifically in $Mn_3Zn_{0.50}Ge_{0.50}N$) leads to a broadened sharp change in lattice contraction. This doping results in negative thermal expansion behavior, with an α_L value of -7.15 $\times 10^{-6}$ K^{-1}, observed for the temperature range of 348 to 448 K (ΔT = 100 K) [162]. Another example is Mn_3CuN, where doping Ge at the Cu-site induces negative thermal expansion behavior. In the case of $Mn_3Cu_{0.53}Ge_{0.47}N$, the material exhibits an α_L value of -1.2 $\times$ 10^{-5} K^{-1} within the temperature range of 267-342 K (ΔT = 75 K) [167, 170].

Furthermore, the NTE temperature range for Mn_3XN can be broadened by doping the N site, which can only be achieved through the concurrent codoping of the X site with a relaxant element. For instance, in the case of Mn_3ZnN, by substituting Zn and N sites with Sn and C in $Mn_3Zn_{0.4}Sn_{0.6}N_{0.85}C_{0.15}$, the value of α_L is -2.3 $\times$ 10^{-5} K^{-1} within a temperature range from 270 to 336 K (ΔT = 76 K) [154]. In addition, Takenaka et al. [169, 168, 170] demonstrated the tuning of continuous negative thermal expansion (NTE) behavior over a wide temperature range through an extensive investigation of $Mn_3Cu_{1-x}X_xN$ compounds (X = Ag, Co, Ga, Ge, In, Ni, Pd, Rh, Sn, and Zn). For a more comprehensive information, valuable insights can be obtained by referring to a review article on negative thermal expansion (NTE) materials, with a specific focus on Mn-based antiperovskites [168, 170, 31, 174, 155].

The origin of a large NTE in Mn_3XN is attributed to significant changes in crystal volume resulting from variations in the magnetic moment, known as the magneto-volume effect (MVE). As an example, $Mn_3Zn_{0.9}Ge_{0.1}N$ exhibits the largest MVE among other AP compounds, characterized by a volumetric contraction of 1.4% and a α_L of -2.28 $\times$ 10^{-4} K^{-1} (<202 K < T < 222 K) [162]. The spontaneous volume magnetostriction (ω_s) is a fundamental aspect of the MVE, representing the interplay between magnetism and volume change due to a magnetic phase transition. It can be used as a quantitative measure to characterize the MVE.

1.2 Piezomagnetic effect (PME)

The piezomagnetic effect (PME) is most prominently observed in antiferromagnetic (AFM) materials, where the zero net magnetization transforms into a finite magnetization upon the application of external strain [104, 206]. Advanced materials, such as multiferroic materials, that exhibit strong interactions between different physical properties, such as mechanical, electronic, and magnetic, hold great potential for engineering cutting-edge devices in fields ranging from sensors and transducers to memory storage and spintronics [41, 156, 185]. Antiperovskite (AP) compounds exhibit two desirable characteristics of multiferroics: the PME and magnetoelectric (ME) coupling. AP compounds with non-collinear AFM structure (Γ_{4g} and Γ_{5g}) exhibit PME, the application of biaxial strain can induce a net magnetization, driven by the presence of frustrated exchange interactions. This phenomenon has been experimentally observed in Mn_3NiN [17] and theoretically predicted in Mn_3SnN [206], demonstrating a large PME in these compounds.

The induced PME in non-collinear antiferromagnetic (AFM) AP compounds can be utilized to form ME composites by integrating the PME AP compound with ferroelectric (piezoelectric) perovskite compounds due to their comparable lattice parameters [103, 17, 144], which are coupled through interfacial strain [132]. This two-phase heterostructure composite offers an enhanced ME effect compared to the relatively small intrinsic ME effect observed in bulk antiferromagnetic material Cr_2O_3 [34]. For instance, a heterostructure composite formed by epitaxially growing a Mn_3NiN film on a ferroelectric $BaTiO_3$ compound ($Mn_3NiN/BaTiO_3$) exhibits a giant PME and a ME coefficient (α) of 0.018 G cm/V (α = dB/dE) [17], which is 1000 times larger than that of Cr_2O_3.

The magnetization in the epitaxial heterostructures can be manipulated using an external electric field, which is achieved by altering the direction of ferroelectric polarization [103]. In this context, the interfacial magnetoelectric coupling achieved through heterostructures containing non-collinear antiferromagnets and ferroelectric materials shows promise in enabling magnetization switching [144, 103]. For instance, the epitaxial heterostructure consisting of $Mn_3GaN/BaTiO_3$ demonstrates an intriguing phenomenon. By switching the ferroelectric polarization, the net magnetization of Mn_3GaN undergoes a rotation of approximately 20, effectively manipulating the non-collinear magnetic moments [144].

1.3 Caloric effect

Caloric materials are in the focus of interest as potential candidates for future energy-efficient and environmentally friendly cooling technologies that have advantages over the established vapour-compression refrigeration technology [33].[1] The two most important parameters for caloric materials are adiabatic temperature changes (ΔT_{ad}) and large isothermal entropy changes (ΔS_{iso}). Caloric effects are usually thermal effects that occur due to phase transitions controlled by external fields. One of the phenomena is the magnetocaloric effect, which is characterized by the heating and cooling of the magnetic material when a magnetic field is applied and removed, resulting in an adiabatic temperature change due to entropy changes [44].

Most APs with magnetocaloric properties are Mn-based carbides Mn_3XC (X= Al, In, Ga, Sn, and Zn), which exhibit significant magnetocaloric effect comparable to typical magnetocaloric materials [203, 183, 181]. For example, Mn_3GaC undergoes a first-order metamagnetic phase transition from antiferromagnetic (AFM) to canted ferromagnetic (FM) at 165 K [84, 85]. It exhibits a magnetic entropy change (ΔS_M) of approximately 15 $J/kg^{-1}K^{-1}$ at an applied magnetic field of 2 T, and the corresponding ΔT_{ad} value reaches 5.4 K [173]. In another example, a second-order FM to paramagnetic (PM) phase transition occurs in Mn_3AlC at T_C of 287 K, with a maximum ΔS_M of 3.28 $J/kg^{-1}K^{-1}$ for an applied magnetic field of 4.5 T and relative cooling power of 328 J/kg^{-1}, which is nearly 1.5 times larger than in Mn_3GaC [183].

Another caloric effect exhibited by APs is the barocaloric effect, which is driven by hydrostatic pressure [33]. Mn-based antiperovskites manifest a barocaloric effect closely related to the isostructural transition from the AFM to the PM state near the Neel temperature (T_N). A large barocaloric effect is expected for materials with a significant magnetovolume effect. The magnetically frustrated antiferromagnetic Mn-based AP nitrides are well

---

[1] The caloric properties are not discussed in this thesis.

documented because of their large magnetovolume effect. As a result, Mn-based nitrides Mn_3XN (X = Ga, In, Ni, Pd, and Zn) exhibit a barocaloric effect with a significantly large entropy change [106, 171, 18, 16]. For example, Mn_3GaN is a well-known barocaloric material that undergoes a magnetic transition from AFM to PM at 290 K, followed by a volume reduction of nearly 1%, showing a huge barocaloric effect with an entropy change of 22.3 $J/kg^{-1}K^{-1}$ for an applied hydrostatic pressure of 139 MPa [106]. In the case of Mn_3NiN, the isothermal entropy change is 35 $J/kg^{-1}K^{-1}$ at 280 MPa close to the transition from AFM to PM at 262 K [18].

1.4 Topological Transport Properties

The anomalous Hall effect (AHE) and anomalous Nernst effect (ANE) are two well-known transport phenomena of great significance that exhibit topological characteristics. These phenomena have applications in spintronic devices, such as energy-efficient data storage, sensors, etc [66, 217]. Recent studies have shown that materials possessing a kagome lattice and Weyl points near the Fermi energy exhibit large Anomalous Hall Conductivity (AHC) and Anomalous Nernst Conductivity (ANC), as exemplified in $Co_3Sn_2S_2$. Antiperovskite compounds possess both of these properties, consisting of a kagome lattice in the (111) plane and characterized by the presence of Weyl points [75].

1.4.1 Anomalous Hall Effect

The Anomalous Hall Effect (AHE) is defined as the generation of a transverse voltage perpendicular to the applied longitudinal electric current in the absence of an external magnetic field. It encompasses extrinsic and intrinsic contributions, which arise from impurity scattering (skew scattering, side jump) and the properties of the band structure, respectively [114]. In our thesis work, we evaluated the intrinsic contribution derived from the Berry curvature. AHE is an intriguing electrical transport phenomenon that was initially believed to be directly proportional to the magnetization, leading to its observation primarily in ferromagnetic materials [57]. However, further research revealed that AHE is derived from the summation of the Berry curvature $\Omega_n(\mathbf{k})$ across all occupied bands below the Fermi energy (Equation 9.2) [114, 26].

FM compounds exhibit a finite AHE due to the absence of time-reversal symmetry in the presence of spin-orbit coupling. Two recent high-throughput studies have reported large AHC values in various FM materials [205, 141]. For example, Pt_3Cr shows the highest AHC value of 2060 S/cm [141], while $MnInRh_2$ exhibits an AHC value of 5214 S/cm [205].

Moreover, it has been demonstrated that the AHC in ferromagnetic (FM) compounds is influenced by the magnetization axis. For instance, in hcp-Co, the AHC value decreases from 481 to 116 S/cm when the magnetization axis changes from the easy axis along the c-axis to the ab plane. Similarly, in CoPt, a change in the magnetization axis from [001] to [110] results in a tuning of the AHC sign and magnitude from -119 to 107 S/cm [207]. This behavior can be explained by considering the symmetry of the system, as changing the magnetization axis leads to a modification in the magnetic space group, thereby altering the band topology and causing a change in both the sign and magnitude of the AHC.

Recently, Chen *et al.* discovered that AHE can be realized in the non-collinear AFM cubic compound Mn_3Ir in the presence of spin-orbit coupling [30]. Later, it was reported in non-collinear AFM hexagonal compounds Mn_3X (X = Ga, Ge, and Sn) [209, 115]. Experimental investigations on Mn_3Ge have reported an AHC value of 500 S/cm at 2K and 50 S/cm at room temperature[119]. AP compounds possess a similar structure to Mn_3Ir and exhibit a non-zero AHC. For instance, in the cubic structure, APs with a non-collinear Γ_{5g} configuration exhibit zero AHC, whereas the Γ_{4g} state results in a finite AHC. Several theoretical studies have reported the presence of AHC in non-collinear AP compounds [140, 75, 212, 59, 152], while some experimental studies have also observed AHC in these materials [202, 15, 61]. In the case of Mn_3GaN, Samathrakis et al. [140] demonstrated that the AHC can be manipulated by controlling the magnetic ordering of non-collinear structures, resulting in a transition from zero or small values of AHC to significant finite values of AHC. However, when subjected to applied biaxial strain, both non-collinear antiferromagnetic (AFM) states Γ_{4g} and Γ_{5g} exhibit finite AHC, as reported in both theoretical studies [175, 140] and experimental observations [202, 15, 83].

1.4.2 Anomalous Nernst Effect

The anomalous Nernst effect (ANE) is characterized by the generation of a transverse electric current in response to an applied temperature gradient that is perpendicular to both the temperature gradient and the magnetization direction (Figure 7.1) [120]. ANE has received significant attention due to its potential applications in thermoelectric power generation [21]. It is also known as spin caloritronics, a field of research that combines the fundamental aspects of spintronics and thermoelectrics. This emerging field, often referred to as “green spintronics,” holds promise for energy-efficient applications [7]. In contrast to conventional thermoelectric devices based on the Seebeck effect, where the electric current is generated in the direction of the thermal gradient, Nernst devices offer several advantages, including a simpler design and the absence of a requirement for p-type and n-type materials. Further benefits are summarized in this review article [108].

ANE, which is closely linked to the Berry curvature of the material's bands near the Fermi energy [196], is a thermomagnetic effect that can be observed in both ferromagnetic and antiferromagnetic materials. It has been extensively studied in various ferromagnetic compounds [32, 3, 198], where some exhibit significant ANE values. For instance, an experimental study on the ferromagnetic cubic compound Co_2MnGa demonstrates a large ANC of 4.0 A/mK, attributed to the presence of Weyl points near the Fermi energy [136]. Similarly, investigations on iron-based binary ferromagnetic compounds, such as Fe_3Al and Fe_3Ga, report significant ANC values of 2.0 Am/K and 4.0 A/mK, respectively, at room temperature [137]. Furthermore, a recent high-throughput study reports an enhanced ANC value of -7.24 Am/K in the ferromagnetic compound Ni_3Pt [141].

Non-collinear antiferromagnetic (AFM) materials also exhibit ANE which was initially reported in hexagonal compounds such as Mn_3X (X = Sn, Ge, and Ir)[193, 76]. In the case of non-collinear antiferromagnetic APs, theoretical studies have focused on investigating ANE in Mn_3XN compounds (X = Ag, Ga, Ni, and Zn) [212]. Among these compounds, Mn_3NiN was predicted to exhibit a significant ANE of 1.80 Am/K at 200 K. Moreover, in a recent experimental study, an ANE signal was observed for Mn_3SnN thin films oriented along the (001) plane at 100 K. The study also demonstrated that ANE can be regulated by applying biaxial strain, which induces changes in the non-collinear antiferromagnetic (AFM) configurations due to the piezomagnetic effect [201]. In another experimental investigation [82], Mn_3NiN thin films deposited on $SrTiO_3$ substrates exhibit the ANE.

1.5 Thesis Chapter Layout

This thesis work is organized into nine chapters. Chapter 1 provides an introduction to the various magnetic properties of AP materials. In Chapter 2, we focus on the methods, discussing topics such as the theory of three stability parameters, and the workflow of our high-throughput environment (HTE). Chapter 3 delves into the stability analysis of APs. In Chapter 4, we present a detailed analysis of the magnetic ground state. Moving on to Chapter 5, we explore the magnetostructural coupling and discuss associated properties, including negative thermal expansion (NTE) and the piezomagnetic effect (PME). Chapters 6 and Chapter 7 are centered around the topological transport properties, specifically the anomalous Hall conductivity (AHC) and the anomalous Nernst conductivity (ANC). In Chapter 8, a summary and outlook for the thesis are provided. The final chapter, Chapter 9, presents the computational details, including supporting Figures and Tables.

2 Methods

In this chapter, we first explain the fundamentals of three stability criteria that are used to determine the stability of experimentally known APs and predict new AP compounds.[1] Next, we discuss the workflow for evaluating the stability and transport properties.

2.1 Thermodynamical stability

Thermodynamic stability is one of the condition for designing new materials. It is evaluated in two steps. In the first step, the formation energy (E_f) is calculated for antiperovskites, which is determined using the following equation:

$$\mathrm{E}_f = \mathrm{E}_{\mathrm{M_3XZ}} - (3\mathrm{E}_\mathrm{M} + \mathrm{E}_\mathrm{X} + \mathrm{E}_\mathrm{Z}) \tag{2.1}$$

where, $\mathrm{E}_{\mathrm{M_3XZ}}$ represents the total energy of the AP compound, while E_M, E_X, and E_Z represent the energies of the bulk phase of the constituent elements. The second step includes the evaluation of convex hull distance ($\Delta\mathrm{E}_h$). $\Delta\mathrm{E}_h$ is evaluated using all the available competing phases in our in-house developed high-throughput database and the Materials Project database [80]. Our in-house database contains approximately 3900 experimentally reported relevant binary and ternary phases with 3d elements (M = Cr, Co, Fe, Mn, and Ni) suitable for this study, and an additional approximately 5200 phases are considered from the Materials Project database. For a compound to be thermodynamically stable, it must satisfy the conditions $\mathrm{E}_f < 0$ and $\Delta\mathrm{E}_h = 0$. The first condition, $\mathrm{E}_f < 0$, guarantees stability against the decomposition of the given compound into its individual elements, as described by equation 2.1. On the other hand, the second condition, $\Delta\mathrm{E}_h = 0$, ensures stability against the decomposition of the given compound into any possible combination of binary and ternary known phases. For example, in the case of $\mathrm{Co_3PdN}$, as depicted in the Figure 2.1, E_f is -0.084 eV/atom and $\Delta\mathrm{E}_h$ is zero, indicating the thermodynamic stability of the compound.

---

[1] The theoretical part is taken from our published work [151, 150].

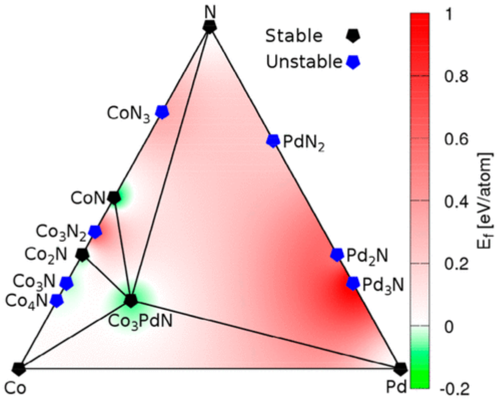

Figure 2.1: The ternary phase diagram of Co_3PdN.

2.2 Mechanical stability

In some cases, a distorted structure may exhibit a lower total energy under mechanical strain. This aspect can be assessed through mechanical stability analysis, which is defined by the strain energy (W). The strain energy (W) quantifies the energy difference between the strained state (E_{str}) and the unstrained state (E_{unstr}), based on the elastic constants.

$$W = E_{str} - E_{unstr} = \frac{1}{2}\sum_{i,j} C_{i,j}\epsilon_i\epsilon j, \tag{2.2}$$

where ϵ represents strain and $C_{i,j}$ denote second-order elastic tensor compounds. If a given compound satisfies the Born stability conditions, it is considered mechanically stable [22, 23, 56, 111]. According to these conditions, the strain energy (W) must be positive, indicating that all eigenvalues of the Cij matrix should also be positive. For cubic Laue class m$\bar{3}$m, there are three independent elastic constants: C_{11}, C_{12}, and C_{44}. Hence, the elastic tensor matrix is given as follows:

$$\begin{pmatrix} C_{11} & C_{12} & C_{12} & 0 & 0 & 0 \\ C_{12} & C_{11} & C_{12} & 0 & 0 & 0 \\ C_{12} & C_{12} & C_{11} & 0 & 0 & 0 \\ 0 & 0 & 0 & C_{44} & 0 & 0 \\ 0 & 0 & 0 & 0 & C_{44} & 0 \\ 0 & 0 & 0 & 0 & 0 & C_{44} \end{pmatrix} \tag{2.3}$$

In addition, according to Mouhat et al. [111], the Born stability condition for mechanical stability of a cubic compound can be stated as follows:

$$C_{11} - C_{12} > 0 \tag{2.4a}$$

$$C_{11} + 2C_{12} > 0 \tag{2.4b}$$

$$C_{11} > 0 \tag{2.4c}$$

$$C_{44} > 0 \tag{2.4d}$$

A cubic compound is regarded as mechanically stable if it satisfies all the conditions mentioned in equations 2.4a-2.4d.

2.3 Dynamical stability

The dynamical stability of a given compound describes its stability under vibrational or dynamic state. It assesses whether the compound's atomic positions and lattice structure are energetically favorable and capable of withstanding atomic displacements or thermal vibrations without undergoing structural transition. The dynamical stability is evaluated by analyzing the phonon dispersion, which is calculated using the harmonic approximation, and the total energy can be expressed as follows [123]:

$$E = E_0 + \frac{1}{2} \sum_{\boldsymbol{R},\sigma} \sum_{\boldsymbol{R}',\sigma'} D_{\boldsymbol{R}\sigma} \Phi^{\sigma\sigma'}_{\boldsymbol{R}\boldsymbol{R}'} D_{\boldsymbol{R}'\sigma'} \tag{2.5}$$

where $\boldsymbol{R}$ and σ represents atomic-position and direction of atomic lattice. $\Phi^{\sigma\sigma'}_{\boldsymbol{R}}$ denotes interatomic force constant matrix. The dynamical matrix $D(\boldsymbol{q})$ is derived by performing a Fourier transformation of $\boldsymbol{\Phi}(\boldsymbol{R})$, resulting in the following expression:

$$D(\boldsymbol{q}) = \frac{1}{M} \sum_{\boldsymbol{R}} \boldsymbol{\Phi}(\boldsymbol{R}) e^{-i\boldsymbol{q}\boldsymbol{R}} \tag{2.6}$$

where $\boldsymbol{q}$ denotes phonon wave-vector. By diagonalizing the dynamical matrix $D(\boldsymbol{q})$, one can determine the eigenvectors and eigenvalues $\omega_n^2(\boldsymbol{q})$. A compound is considered dynamically stable when the dynamical matrix $D(\boldsymbol{q})$ is positive. Consequently, every eigenvalue $\omega_n^2(\boldsymbol{q})$ is positive, ensuring that every frequency $\omega_n(\boldsymbol{q})$ is a real value.

2.4 High-throughput workflow

High-throughput screening (HTP) is a well-organized approach that accelerates the search for novel materials. In this context, HTP calculations are systematically performed to evaluate the stability of APs and determine transport properties such as AHC and ANC, as illustrated in the workflow discussed in the following subsections.

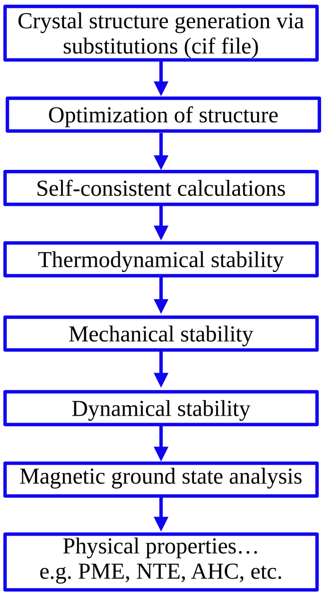

Figure 2.2: Workflow for evaluating the stability and properties of AP compounds.

2.4.1 Stability

The stability of AP compounds is calculated following a step-by-step calculation scheme as illustrated in Figure 2.2. Thermodynamical stability (step 1-4) is assessed using in-house python code developed by Ingo Opahle, which has been verified in numerous studies [151, 150, 145, 127, 124, 125].

1. The crystal structure files (POSCAR) are generated using a CIF file by substituting the elements.

2. The lattice parameters are optimized using VASP, with the calculation setup mentioned in Chapter 9.1.1.

3. The self-consistent field (scf) spin-polarized calculations are performed to obtain the total energies of the AP compounds.

4. Thermodynamic stability is obtained in two steps. First, the formation energy E_f is determined, and then ΔE_h is evaluated using an in-house developed database.

5. The mechanical stability is calculated for the thermodynamical stable AP compounds.

6. Next, the dynamical stability is analyzed for those AP compounds, which are both mechanically and thermodynamically stable.

7. Then, the magnetic ground state of stable magnetic APs is determined by considering seven magnetic configurations.

8. Finally, various physical properties of APs are analyzed in their respective lowest energy magnetic states, see next section.

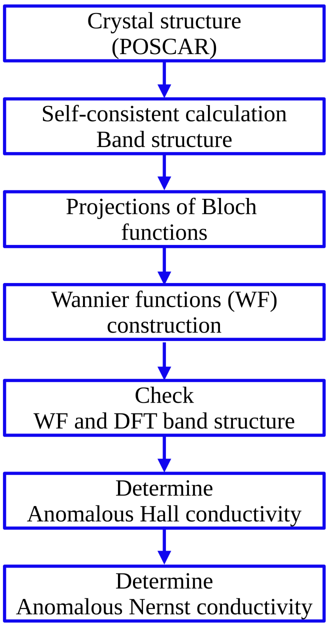

Figure 2.3: Workflow to determine the anomalous Hall conductivity (AHC) and anomalous Nernst conductivity (ANC).

2.4.2 Transport properties

The AHC and ANC of non-collinear AFM and FM AP compounds are calculated using a combination of Bash and Python codes, following a step-by-step calculation scheme as illustrated in Figure 2.3.

1. The self-consistent field (scf) spin-polarized calculations are performed using the VASP code [92], with the calculation setup mentioned in Chapter 9.1.1.
2. The band structure calculations are performed using the charge density obtained from the scf step.
3. In this step, an interface is established between VASP and Wannier90 [110]. The Bloch functions obtained from VASP are projected onto the selected orbitals, which are then used as input for the subsequent Wannier90 calculation in the next step.
4. Wannier functions are constructed using the Wannier90 code, with the disentanglement window set at 3 eV above the Fermi energy for all calculations.
5. The calculated DFT and Wannier function band structures are compared, and it is observed that they exhibit complete overlap for all the calculations. This demonstrates a high level of accuracy in the analysis, as confirmed through visualization.
6. Next, the anomalous Hall conductivity (AHC) is computed using the WannierTools code [192].
7. Finally, the anomalous Nernst conductivity (ANC) is determined using an in-house developed code (Ilias Samathrakis [141]) based on the data obtained from the AHC calculations.

3 Designing of magnetic antiperovskites

In order to predict new magnetic antiperovskites (APs) and validate experimentally known APs, a high-throughput screening is conducted using three stability criteria: thermodynamical stability, mechanical stability and dynamical stability (theory and methods are discussed in the Chapter 2). In total, 630 magnetic APs were studied with the chemical formula M_3XZ (M are the magnetic transition metal atoms Cr, M Fe, Co, and Ni; X are the elements from Li to Bi except noble gases and 4f rare- earth metals (Figure 3.4); and Z are C and N). Out of the 630 compounds investigated, 76 have already been synthesized experimentally and can be divided into three categories based on their crystal structure and composition: 50 stoichiometric cubic (Table 9.1), 14 non-stoichiometric cubic (Table 9.2), and 12 tetragonal/orthogonal (Table 9.3). In this chapter, the stabilities of the 76 known compounds are systematically verified and 11 new cubic APs are predicted. First, the thermodynamical stability of APs is discussed, which is calculated using the formation energy together with the convex hull. To understand the trend of the thermodynamical stability, a detailed analysis of the chemical bonds is conducted using the Crystal Orbital Hamilton Population (COHP) [38] approach implemented in the LOBSTER code [105]. Next, we analyzed the mechanical and dynamic stabilities, which were evaluated using the elastic constants and phonon dispersion, respectively. All calculations are performed considering the cubic structure in the ferromagnetic state, even for the APs that are experimentally reported in non-cubic structure. However, we have also performed calculations in non-cubic structure to verify the stability of some compounds that are explicitly mentioned in the text and tables.[1]

3.1 Thermodynamical stability

3.1.1 Formation energy (E_f) of reported APs

As listed in the Table 9.1, all the experimentally reported bulk stoichiometric cubic APs satisfy the formation energy criteria ($E_f < 0$) except for Ni_4N (0.008 eV/atom), Fe_3ZnC (0.01 eV/atom), and Mn_3InC (0.02 eV/atom). These positive E_f values are smaller

---

[1] The results discussed in this chapter are based on our published work [151].

Table 3.1: The validation of stability from our calculations for the experimentally synthesized APs in stoichiometric cubic, non-stoichiometric cubic, and non-cubic structures. The number of APs satisfying each stability criterion as formation energy (E_f < 0 meV/atom), distance to the convex hull (ΔE_h < 50 meV/atom), mechanical stability ($C_{11} > 0$, $C_{11} - C_{12} > 0$, $C_{11} + 2C_{12} > 0$, and $C_{44} > 0$), and dynamical stability (ω_n^2 (**q**) > 0).

Compounds composition	Stoichiometric cubic	Non-stoichiometric cubic	Non-cubic/ thin-film
Total compounds	50	14	12
$E_f < 0$ meV/atom	47	12	9
$\Delta E_h < 50$ meV/atom	37	8	2
Mechanically stable	48	14	11
Dynamically stable	44	9	1

than $k_B T$ at room temperature. Thus, several factors such as the magnetic structure, temperature effects, and reduction of systematic errors in the DFT calculations are likely to further reduce the total energy of the compounds. For the reported non-stoichiometric cubic APs (Table 9.2), a total of 12 out of 14 meet the $E_f < 0$ criteria with the exception of Co_3GeC (0.055 eV/atom) and Co_3SnC (0.013 eV/atom), which is not unexpected since the E_f were calculated using the stoichiometric composition instead of the reported non-stoichiometric C-deficient composition ($Co_3GeC_{0.25}$ [73] and $Co_3SnC_{0.7}$ [158]). For the experimentally reported non-cubic APs, a positive E_f is obtained for 3 out of 12 compounds when calculated in the cubic $Pm\bar{3}m$ space group structure (Table 9.3). However, the formation energy is negative ($E_f < 0$) when calculated in the reported crystal structure. For example, Cr_3PC has an orthorhombic crystal structure (*Cmcm*) [214] and the calculated E_f in the $Pm\bar{3}m$ and *Cmcm* structures are 0.108 eV/atom and -0.286 eV/atom, respectively.

3.1.2 Convex hull distance (ΔE_h) of reported APs

The convex hull distance (ΔE_h) is calculated by considering all competing phases stored in our in-house HTE database [126]. Our database incorporates about 3900 experimentally reported binary and ternary phases and about 5200 phases from the Materials Project database[80] relevant for ternary phase diagrams for the 3d magnetic elements M = Cr, M Fe, Co, and N. We define all compounds to be stable against decomposition up to a tolerance limit of $\Delta E_h < 50$ meV/atom. This definition takes into account constraints in the exchange-correlation functional, thermal effects, and numerical approximations. This tolerance range is considered on the basis of recent high-throughput studies, which use a threshold of 30-100 meV/atom [126, 51].

Most stoichimetric cubic APs (Table 9.1) meet the criteria of $\Delta E_h < 50$ meV/atom, with exceptions such as Cr_3XN (X = Sn and Pd) [116], Mn_3XN (X = Al [95], Ni [47], Cu [169], Rh [116], Ag [37], In [164], and Ir [116]) [158], Mn_3InC [88], Mn_3SnC [86], and Ni_3GeC [73]. As discussed in the next chapter, certain Cr and Mn-based APs exhibit an antiferromagnetic (AFM) ground state. For instance, the collinear AFM configuration is the most energetically favourable state for Cr_3SnN and Mn_3InC, and the non-collinear AFM configuration is the for Mn_3XN (Ag, In, Ni, Rh, and Ir) and Mn_3SnC, leading to a decrease in total energy and ΔE_h. For example, the distance to the convex hull ΔE_h decreases from 0.059 eV/atom to 0.0 eV/atom when considering the total energy of the non-collinear AFM state (Γ_{4g}) in Mn_3NiN thus making it thermodynamically stable. However, a large ΔE_h of 0.318 eV/atom is observed for Ni_3GeC [73], showing a substantial 6% deviation between the experimentally reported (3.58 Å) and calculated lattice parameters (3.81 Å). The reported lattice parameter for Ni_3GeC (3.58 Å) is close to that of Ni_3Ge (3.57 Å), which is thermodynamically stable according to our HTE database, indicating that the reported phase is probably C-deficient.

Furthermore, all reported compounds in non-cubic structures are found to be thermodynamically unstable when calculated in the cubic $Pm\bar{3}m$ structure. However, they prove to be thermodynamically stable when analyzed in their corresponding reported crystal structures (Table 9.3). As for the non-stoichiometric cubic APs, a total of 6 out of 14 compounds exhibit $\Delta E_h > 50$ meV/atom, indicating that they are thermodynamically unstable (Table 9.2). The number of APs satisfying the specific stability criteria are listed in Table 3.1.

In total, 178 cubic APs that have not been synthesized , hitherto, have a negative formation energy ($E_f < 0$), only 22 of these compounds meet the criterion for thermodynamical stability with $\Delta E_h < 50$ meV/atom and are thus suitable candidates for synthesis (Table 9.4). We believe that it is crucial to consider all possible competing phases to ensure the stability of the predicted new compounds.

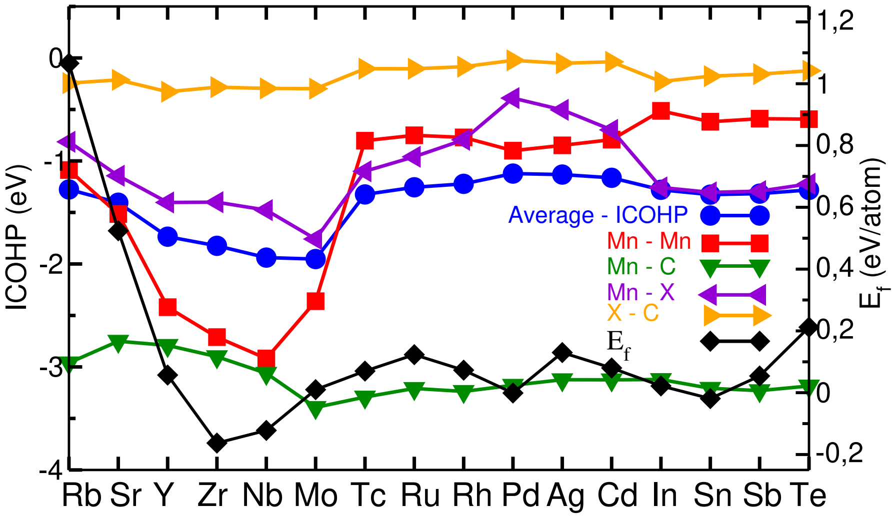

Figure 3.1: The calculated integrated crystal orbital Hamilton population (ICOHP) and formation energy (E$_f$) of Mn_3XC APs, where X corresponds to the elements present on the X-axis.

3.1.3 Crystal Orbital Hamilton Population (COHP)

The chemical bond analysis of Mn_3XC APs (where X stands for elements of the fifth period) is conducted using the COHP approach to understand the trend of formation energy. To identify which bonds contribute to stability, four bonds are selected for analysis: Mn-M Mn-C, Mn-X, and X-C. As illustrated in Figure 3.1, the Mn-Mn integrated COHP (ICOHP) contributes significantly to the average ICOHP has nearly similar trend as the formation energy. The average ICOHP analysis shows that the most stable composition is achieved for X elements Zr and Nb which is also consistent with the trend observed for the formation energy. In additio the Mn-C bonds have the largest contribution to the average ICOHP, whereas the X-C bonds have the smallest contributio suggesting that they are the weakest link and have the least influence on the stability of Mn_3XC compounds. Next, we calculated the ICOHP values for the perovskite copound $SrTiO_3$ and compared them with AP's Mn_3XC. The calculated ICOHP values for the Ti-O, Ti-Sr, O-Sr, and O-O bonds of $SrTiO_3$ are -3.12, -0.96, -0.69, and -0.033 eV/bond, respectively. It can be noticed that the most stable bond in Mn_3XC is Mn-C, while in perovskite $SrTiO_3$ the most stable bond is Ti-O. This indicates that the bonds between the face-centered ions and the body-centered ions are the most stable bonds for both APs (M-C) and perovskites (Ti-O). However, the least stable bonds are different in $SrTiO_3$, where O-O bonds are the least stable, while in APs the X-C bonds are the least stable.

3.2 Mechanical stability

The mechanical stability is calculated only for 76 experimentally synthesized APs and 22 newly predicted APs through thermodynamical stability criteria. Thermodynamical stability of the 22 predicted new APs does not guarantee that these APs will remain in a cubic phase. Their energy may further decrease due to a structural distortion to a non-cubic phase due to mechanical or dynamical instabilities. Note that the mechanical stability calculations were performed considering only the cubic phase for the experimentally reported APs, even though some known APs have a non-cubic structure. Since we focus mainly on cubic APs in this study, a detailed analysis of non-cubic APs is saved for future studies. Concisely, cubic systems have three independent elastic constants, C_{11}, C_{12}, and C_{44}. The mechanical stability of these systems is determined by the following conditions: $C_{11} > 0$, $C_{11} - C_{12} > 0$, $C_{11} + 2C_{12} > 0$, and $C_{44} > 0$.

All 22 predicted novel APs satisfy the mechanical stability criteria and are thus mechanically stable in the considered cubic structure. Similarly, all experimentally synthesized compounds are stable, except Ni_3FeN which was reported as a thin film [166] that does not meet $C_{44} > 0$, and two cubic stoichiometric APs Mn_3InC and Mn_3In which do not meet the criteria for $C_{11} - C_{12} > 0$. It is assumed that Mn_3InC and Mn_3InN are mechanically unstable because the calculations were performed considering the ferromagnetic state instead of their lowest energy configurations, collinear AFM and non-collinear AFM, respectively.

3.3 Dynamical stability

The dynamical stability calculations are performed for the 22 novel APs that meet the thermodynamical and mechanical stability criteria, as well as for the experimentally reported APs. Among the latter, for the stoichiometric cubic APs, 44 out of 50 compounds have no imaginary mode in the whole Brillouin zone, indicating that they are dynamically stable. However, six compounds are dynamically unstable. Five of them show imaginary modes at specific q-points indicated in parentheses (Figure not shown), such as Cr_3RhN (Γ, R), Mn_3CuN (X, M), Mn_3InN (M), Ni_3GaC (M), Cr_3IrN (Γ, R-M-R), while Ni_3GeC shows imaginary modes throughout the Brillouin zone and is also found to be thermodynamically unstable. Five non-stoichiometric APs are dynamically unstable, such as Co_3AlC (data missing), Co_3GaC (M), Co_3GeC (throughout the Brillouin zone), Mn_3CoN (X-M, R), and Ni_3AlC (M). However, Mn_3InN, Mn_3CoN, and Cr_3IrN have a non-collinear antiferromagnetic ground state as their lowest energy configuration. Since the phonon calculations are performed considering the ferromagnetic state, this could be the reason for the dynamical instability.

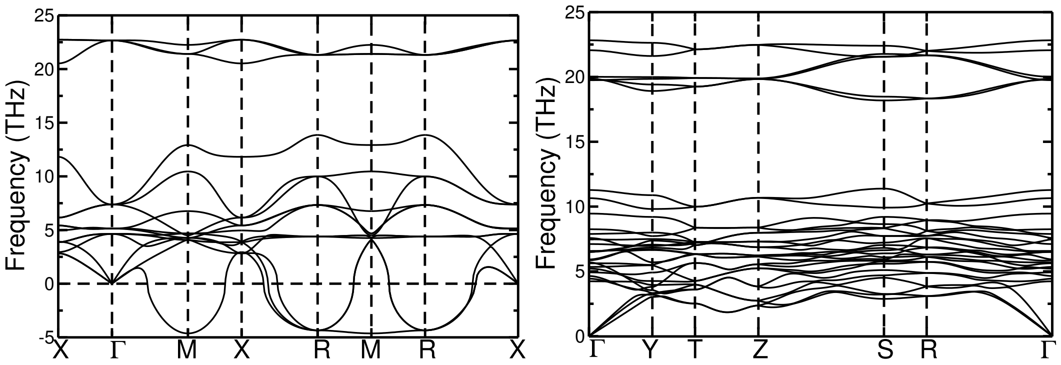

Figure 3.2: Calculated phonon dispersion for Cr_3GeC in $Pm\bar{3}m$ (left) and in *Cmcm* (right) space groups.

Eleven APs reported in non-cubic crystal structures have the space groups *Cmcm, I4/mcm,* $P42_1m$ *and P4/mmm* (Table 9.3). These compounds exhibit dynamical instability when their phonon dispersion is calculated in a cubic structure, with the exception of Ni_3FeN. The space groups *Cmcm* and *I4/mcm* are subgroups of $Pm\bar{3}m$ [160]. If R_4^+ and M_3^+-R_4^+ imaginary modes exist in the cubic structure $Pm\bar{3}m$, then a crystal can be stabilized according to the eigen-modes of the imaginary phonons in subgroups such as *Cmcm* and *I4/mcm*. This is shown by the example of Cr_3GeC (Figure 3.2), which has an orthorhombic crystal structure with the space group *Cmcm* and has imaginary modes at M_3^+-R_4^+ with a frequency of nearly 5 THz in the cubic crystal structure $Pm\bar{3}m$. However, when the phonon dispersion is calculated in the *Cmcm* crystal structure, it does not show any imaginary mode.

Finally, of 22 potentially novel APs predicted to be stable in the cubic structure based on thermodynamic and mechanical stability, only 11 were found to exhibit lattice dynamic stability (Figures not shown). The remaining 11 dynamically unstable APs can be stabilized in distorted structures by freezing the imaginary eigen-modes, as shown in the case of Cr_3GeC which is saved for future investigations.

Table 3.2: The list of newly predicted cubic APs satisfying all three stability criteria (thermodynamical, mechanical, and dynamical) and their calculated lattice constant (Å), formation energy E_f (eV/atom), distance to the convex hull ΔE_h (eV/atom), and magnetic moment M (μ_B/f.u.).

Compounds	a (Å)	E_f (eV/atom)	ΔE_h (eV/atom)	M (μ_B/f.u.)
Co_3LiN	3.72	-0.134	0.031	2.90
Co_3AuN	3.83	-0.051	0.000	4.36
Co_3GaN	3.75	-0.230	0.040	2.60
Co_3PdN	3.80	-0.084	0.000	5.13
Co_3PtN	3.80	-0.103	0.000	5.14
Co_3RhN	3.78	-0.007	0.041	6.07
Co_3SnN	3.85	-0.077	0.009	2.22
Co_3ZnN	3.74	-0.184	0.000	2.85
Fe_3CuN	3.79	-0.105	0.036	6.96
Fe_3IrN	3.83	-0.104	0.037	7.81
Ni_3LiC	3.75	-0.063	0.000	0.70

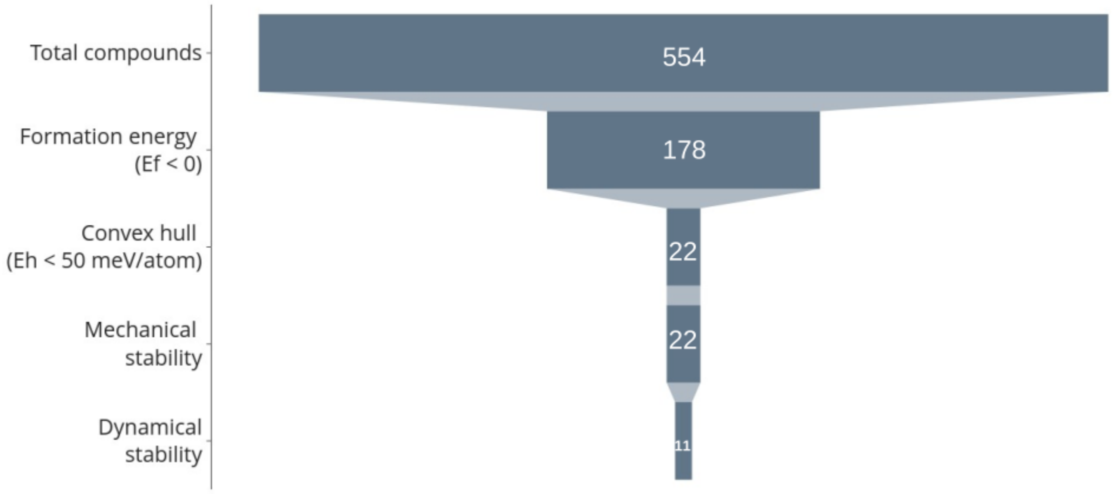

Figure 3.3: The number of novel cubic APs reduces at each level of stability criteria.

3.4 Predicted APs and their experimental validation

In summary, Figure 3.3 displays the decrease in the number of APs at each level of stability criteria. Out of 554 unknown APs, only 178 have negative formation energy ($E_f < 0$), which is further reduced to 22 after considering the convex hull distance and are therefore thermodynamically stable. All 22 thermodynamically stable compounds are mechanically stable, but only 11 meet the criteria for dynamic stability (Table 3.2). All predicted compounds exhibit magnetic behavior and possess a metallic electronic structure in the considered FM state and all are nitrides except Ni_3LiC (Table 3.2). Remarkably, three of the predicted APs, namely Co_3SnN [65], Co_3ZnN [54], and Fe_3IrN [161], were successfully synthesized after our publication confirming the significance of our predictions. All three APs have a FM ground state, which we found out in our detailed analysis of the magnetic ground state (discussed in the next Chapter 4). Therefore, in our view, a systematic investigation of all three stability criteria is crucial for the prediction of novel compounds by means of high-throughput design.

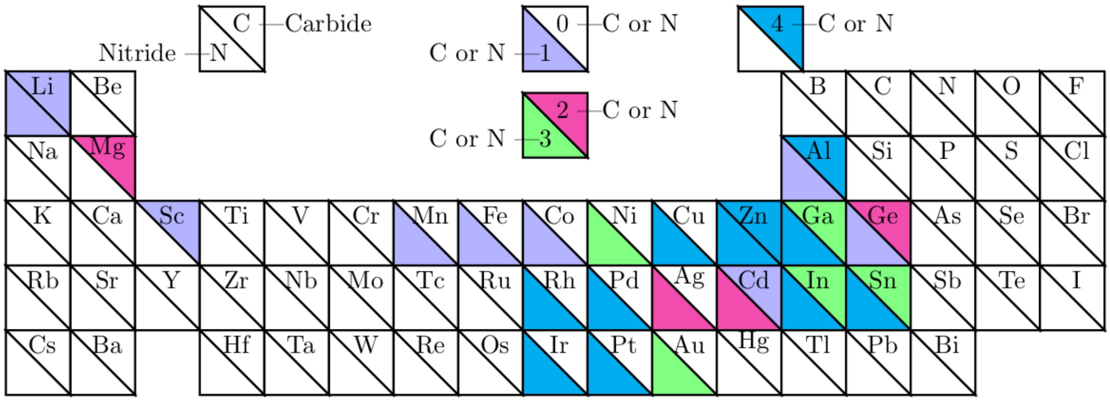

Figure 3.4: The periodic table shows the distribution of the X elements that form the stable APs with the chemical formula M_3XZ. The upper right and lower left triangular corners correspond to the AP carbides and nitrides, respectively. The coloured triangles indicate the number of stable phases each X-element forms.

Furthermore, we have illustrated the distribution of X elements (M_3XZ) for stable APs, including both known and novel APs (Figure 3.4). Several d-block transition metals of groups 9th-11th, namely Au, Cu, Ir, Pd, Pt, and Rh form the highest number of stable APs, with each of them forming four stable AP nitrides. Also, p-block elements from the 13th and 14th groups (Ga, In, and Sn) each form four stable AP nitrides, while only Li and Mg from the s-block elements form stable AP compounds.

4 Magnetic ordering in antiperovskites

The magnetic ground state analysis is carried out for 54 stable APs, comprising 43 experimentally reported compounds (excluding the non-stoichiometric cubic, non-cubic, and non-magnetic APs from the list of 76 experimentally known APs) and 11 new APs predicted using the three stability criteria discussed in the previous chapter. To obtain the magnetic ground state, seven magnetic configurations are considered, consisting of two non-collinear antiferromagnetic characterized by irreducible representation (Γ_{4g} and Γ_{5g}), three collinear AFM (cAFM-1, cAFM-2, and cAFM-3), one non-collinear ferrimagnetic (M-1), and a ferromagnetic (FM) state (Figure 4.1 (a-g)). We found that 15 APs are stabilized in a non-collinear AFM structure, while 6 APs exhibit a collinear AFM structure as the lowest energy state (Table 9.6). The remaining 33 APs are found to possess a ferromagnetic ground state (Table 9.6). Next, a detailed analysis is performed for non-collinear AFM APs to investigate their magnetic ordering by evaluating the change in spin-orbit coupling (SOC) energy (ΔE_{SOC}) between Γ_{5g} and Γ_{4g} configurations. Finally, the magnetic anisotropy energy (MAE) for the 35 ferromagnetic APs[1] are calculated by considering three crystalline magnetization directions [001], [110], and [111] that define MAE in cubic materials. The SOC was taken into account for all the calculations.[2]

4.1 Magnetic structures

APs exhibit various magnetic structures, and some of them have been observed experimentally. These structures are discussed and compared with the calculated magnetic ground state in our study.

4.1.1 Non-collinear AFM

In the cubic structure of APs, the magnetic transition metal atoms occupy the face-centered positions, forming a magnetically frustrated kagome lattice in the (111)-plane (Figure 4.1

---

[1] Ni_3CuC was overlooked in the magnetic ground state analysis. On the other hand, Mn_3AlC exhibits a c-AFM2 magnetic ground state; however, experimentally, it is reported as FM. Therefore, we analyzed Mn_3AlC properties in the FM state.

[2] The work presented in this chapter is part of our published papers [152, 149].

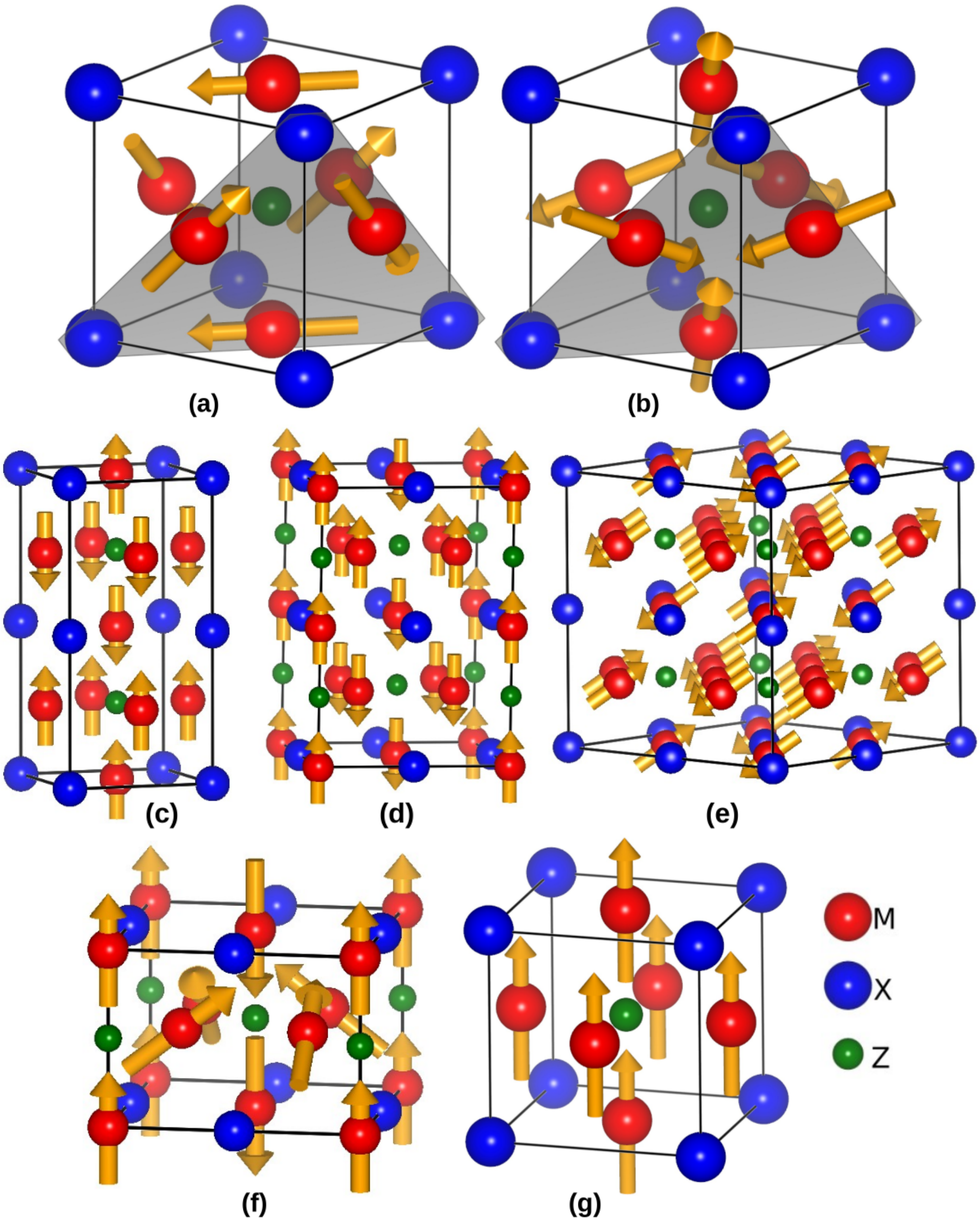

Figure 4.1: The considered magnetic structures of antiperovskites (M_3XZ) in Pm$\bar{3}$m space group (221): (a) Γ_{5g}, (b) Γ_{4g}, (c) c-AFM-1, (d) c-AFM-2, (e) c-AFM-3, (f) M-1, and (g) FM. M atoms form a kagome lattice in the (111) plane (highlighted in gray). The spin moments depict magnetization direction. Note, that the orientation of the spins with respect to the lattice was chosen arbitrarily for the initial screening, as depicted.

(a-b)). The Γ_{4g} and Γ_{5g} states are two common non-collinear AFM configurations reported for Mn-based AP nitrides (Mn_3XN). As shown in Figure 4.1 (a-b), in the case of Γ_{5g} three magnetic atoms in form a 120° angle within the (111) kagome lattice plane, while the simultaneous rotation of the spin moments of three metal atoms by 90° within the (111) plane leads to the Γ_{4g} state. 15 APs are stabilized in either the Γ_{4g} or Γ_{5g} state and all are nitrides except Mn_3SnC, which has the Γ_{5g} state (Table 4.1). However, we have excluded Mn_3SnC from the list of non-collinear AFM structures because a complicated ferrimagnetically ordered structure is reported for Mn_3SnC in the experiments [45, 39, 71], which is not considered in our magnetic ground state analysis.

Table 4.1: The list of APs (M_3XZ) exhibiting either Γ_{4g} or Γ_{5g} non-collinear magnetic ground state ("magGS"). The calculated change in atomically resolved SOC energy (δE_{SOC}) between the Γ_{5g} and Γ_{4g} states are summarized for M and X atoms. The change in total energy ΔE_{tot} and SOC energy ΔE_{SOC} between Γ_{5g} and Γ_{4g} are enumerated using equations 4.1 and 4.2, respectively. The second last column lists the experimentally (Exp.) reported magnetic ground state. The measured Néel temperature (T_N) data is taken from Reference [170]. All energies are given in meV/atom.

M_3XZ	magGS	$^M(\delta E_{SOC})$	$^X(\delta E_{SOC})$	ΔE_{SOC}	ΔE_{tot}	Exp. magGS	T_N
Cr_3IrN	Γ_{4g}	-0.122	4.532	1.041	0.437		
Cr_3PtN	Γ_{4g}	-0.312	5.639	1.175	0.574		
Mn_3AgN	Γ_{4g}	0.133	-0.2486	0.038	0.013	$\Gamma_{4g}+\Gamma_{5g}$ [45]	276
Mn_3AuN	Γ_{5g}	0.402	-4.353	-0.787	-0.334		
Mn_3CoN	Γ_{4g}	0.002	1.716	0.430	0.244		252
Mn_3GaN	Γ_{5g}	-0.370	1.10	-0.277	-0.058	Γ_{5g} [45, 106]	288
Mn_3HgN	Γ_{5g}	-0.249	-3.691	-1.109	-0.310		
Mn_3InN	Γ_{5g}	-0.245	-0.224	-0.239	-0.370		366
Mn_3IrN	Γ_{4g}	0.200	19.705	5.076	2.110		
Mn_3NiN	Γ_{4g}	0.405	-0.87	0.086	0.029	$\Gamma_{4g}+\Gamma_{5g}$ [45]	256
Mn_3PdN	Γ_{4g}	0.431	-1.115	0.044	0.071		316
Mn_3PtN	Γ_{5g}	1.291	-13.877	-2.501	-0.994		
Mn_3RhN	Γ_{4g}	-0.007	3.482	0.865	0.340		226
Mn_3ZnN	Γ_{5g}	-0.252	-0.105	-0.215	-0.290	Γ_{5g} [45, 36]	170

Validation on experimentally observed Γ_{4g} and Γ_{5g} phases

For some compounds, the non-collinear AFM Γ_{4g} and Γ_{5g} phases have been observed in experiments. We found that Mn_3GaN and Mn_3ZnN exhibit a Γ_{5g} phase, which agrees well with experimental measurements [106, 45, 36]. In our calculations, Mn_3AgN and Mn_3NiN display the Γ_{4g} phase as the lowest energy state, whereas in experiments, both compounds exhibit mixed phases consisting of both Γ_{4g} and Γ_{5g} configurations [45]. For Mn_3AgN a mixed phase (Γ_{4g} + Γ_{5g}) subsists below 55 K, and a single Γ_{5g} phase exists between 55 K and 290 K, followed by a magnetic phase transition to the PM phase at 290 K [45]. Similarly, Mn_3NiN also shows mixed phases between 163 K and 266 K [45]. These mixed phases can be attributed to the difference in total energy (ΔE_{tot}) between the Γ_{5g} and Γ_{4g} phases, which is calculated using the following equation:

$$\Delta E_{tot} = E_{\Gamma_{5g}} - E_{\Gamma_{4g}} \tag{4.1}$$

where, E is the total energy of the given magnetic phases. The positive and negative values of ΔE_{tot} correspond to the Γ_{4g} and Γ_{5g} state, respectively. The ΔE_{tot} values for Mn_3AgN and Mn_3NiN are 0.013 and 0.029 meV/atom, respectively. Therefore, we assume that ΔE_{tot} values larger than 0.05 meV/atom are likely to indicate a pure Γ_{4g} or Γ_{5g} phase, as observed for Mn_3GaN and Mn_3ZnN.

Validation on Mn-Based AP nitrides reported theoretically

Seven Mn-based AP nitrides (Mn_3X X = Ni, Z Ga, Pt, I Pd, and Ir), which are also included in our analysis were examined in a recent study [75]. Our calculated magnetic ground states agree with their observations for Mn_3XN (X = Ga, Ni, Pt, and Zn), but not for Mn_3XN (X = I Pd, and Ir). In our study (in the study by Huyen *et al.*), it was found that Mn_3InN exhibits Γ_{5g} (Γ_{4g}) state, while Mn_3XN (X= Ir and Pd) exhibit Γ_{4g} (Γ_{5g}) state. In our calculations (in the calculation by Huyen *et al.*), the calculated ΔE_{tot} for Mn_3InN is -1.84 (74.6) meV/f.u., which is significantly higher than our calculated value and can only be expected for compounds with strong SOC. To clarify the inconsistency, we calculated the ΔE_{tot} using the Quantum Espresso (QE) code [52] with similar calculation parameters as those considered in the Huyen *et al.* study. We obtained the same magnetic ground state for Mn_3XN (X= I Ir, and Pt) from both QE and VASP codes, which contradicts the results of Reference [75].

Prediction of new non-collinear magnetic APs

Based on our systematic magnetic ground state analysis, we predicted four unreported AP compounds to show a non-collinear AFM ground state. Two of them are Cr-based AP nitrides, Cr_3IrN and Cr_3PtN exhibiting Γ_{4g} as the lowest energy magnetic state. The other two compounds are Mn-based AP nitrides, Mn_3AuN and Mn_3HgN with Γ_{5g} as their magnetic ground state. There are no reported neutron diffraction measurements for the predicted AP nitrides, which could be interesting candidates for future synthesis and experimental investigations.

SOC analysis

To understand the origin of ΔE_{tot}, we conducted a detailed analysis of the SOC energy. First, we evaluated the change in the total energy of SOC (ΔE_{SOC}), i.e. the difference between the SOC energy (E_{SOC}) of Γ_{5g} and Γ_{4g} phases [2]:

$$\Delta E_{\mathrm{SOC}} = E_{SOC(\Gamma_{5g})} - E_{SOC(\Gamma_{4g})} \tag{4.2}$$

Further, change in the atomically resolved SOC energy (δE_{SOC}) is defined for M and X atoms (Table 4.1). It is observed that both ΔE_{tot} and ΔE_{SOC} have the same sign indicating that they exhibit the same magnetic ordering and are equally applicable in characterizing the magnetic ground states (Table 4.1). For instance, the calculated ΔE_{tot} and ΔE_{SOC} for Cr_3IrN are 0.437 meV/atom and 1.041 meV/atom, respectively, indicating a Γ_{4g} magnetic ground state. Moreover, the atomically resolved δE_{SOC} of Ir (4.532 meV/atom) is larger than that of Cr (-0.122 meV/atom), resulting from the strong SOC energy of Ir. It means that the δE_{SOC} of Ir is a determining factor for the sign of both ΔE_{tot} and ΔE_{SOC}. Next, we analyzed SOC strength of X elements and its role for larger ΔE_{tot}. In this respect, we considered Mn_3XN (X= Co, Rh, and Ir, elements of the 9th group) as an example. The calculated ΔE_{tot} values for Mn_3CoN, Mn_3RhN, and Mn_3IrN are 0.244, 0.340, and 2.110 meV/atom, respectively, while the SOC strength for the corresponding X elements, Co, Rh, and Ir, is about 0.065, 0.152, and 0.452 eV, respectively [134]. This clearly indicates that an increase in the SOC strength of X elements leads to a larger ΔE_{tot} for the corresponding AP compounds.

Moreover, the main contribution to ΔE_{tot} arises from the spin-orbit coupling (SOC) energy. This is because the energy difference between the exchange energies ($\Delta E_{exchange}$) of the Γ_{5g} and Γ_{4g} phases is very small. For example, the $\Delta E_{exchange}$ values for Mn_3GaN, Mn_3IrN, and Mn_3NiN are 0.0016, 0.0022, and 0.0036 meV/atom, respectively. Therefore, it can be concluded that ΔE_{tot} is primarily due to the SOC energy.

4.1.2 Collinear AFM

We considered three collinear AFM configurations cAFM-1, cAFM-2, and cAFM-3 in our analysis (Figure 4.1 (c-e)).[3] Based on our calculations, we found that six APs have a collinear AFM ground state (Table 9.6). We found that cAFM-2 is the lowest energy configuration for Mn_3GaC. However, Fruchart *et al.* [46, 45], reported that Mn_3GaC has a cAFM-3 configuration and undergoes several phase transitions: a first-order transition from AFM to canted FM at 160 K, followed by a second-order transition from canted FM to collinear FM at 164 K, and finally another second-order phase transition from collinear FM to a PM phase with a T_C of 249 K [89, 87]. Interestingly, Mn_3AlC and Mn_3InC with the same number of valence electrons as Mn_3GaC also stabilize in the cAFM-2 phase, while experimentally it is reported that both have a ferromagnetic ground state [87, 183]. Such inconsistency might be due to the temperature effect, suggesting a strong interaction between crystal structure and magnetism at finite temperatures. For Mn_3AlC and Mn_3InC, there is no experimental data available at low temperatures. This allows us to suggest that temperature-driven phase transitions similar to Mn_3GaC should occur for Mn_3AlC and Mn_3InC. Such discrepancies might be attributed to the temperature effect, indicating a strong interplay between magnetism and crystal structures at finite temperatures. Moreover, Cr_3SnN and Mn_3SnN exhibit cAFM-3 structure. Experimental studies show that Mn_3SnN undergoes various magnetic and crystallographic phase transitions [49, 45], whereas there is no magnetic structure reported for Cr_3SnN experimentally. Co_3GeC displays a cAFM-2 structure, but there have been no experimental studies conducted to investigate its magnetic structure.

4.1.3 Ferrimagnetic M-1 phase

The ferrimagnetic M-1 phase is a combination of collinear AFM and non-collinear spin configuration (Figure 4.1 (f))[4]. Mn_3GaN has a Γ_{5g} magnetic ground state [45] and the ferrimagnetic M-1 phase coexists with the Γ_{5g} state in $Mn_3Ga_{0.95}N_{0.94}$ in the temperature range 6-50 K under pressure [146]. It is found that none of the APs has a non-collinear M-1 phase as the lowest energy configuration. Therefore, it is still an interesting question to investigate the temperature effect and in particular how the magnetic interactions can be

---

[3] The cAFM-1 and c-AFM-3 collinear AFM configurations are achieved by generating a $1 \times 1 \times 2$ and $2 \times 2 \times 2$ supercells, respectively (Figure 4.1 (c and e)). The cAFM-2 configuration is obtained by generating $\sqrt{2} \times \sqrt{2} \times 2$ supercell together with a shift of the atomic position by one-half in the x-direction (Figure 4.1 (d)).

[4] The M-1 phase is obtained by generating a $\sqrt{2} \times \sqrt{2} \times 1$ supercell and shifting the atomic position by one-half in the x-direction.

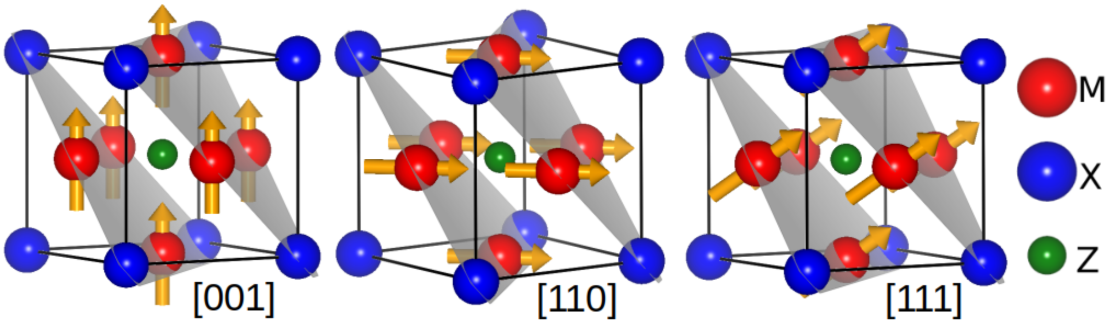

Figure 4.2: The different magnetization direction of ferromagnetic (FM) APs, where the spin moments represent [001], [110], and [111] magnetization directions. The Kagome lattice, which exists in the (111) plane, is highlighted in grey.

tailored by doping and pressure/strain in such a class of compounds. For some compounds, it is noted that the M-1 state converges to either ferromagnetic or antiferromagnetic states, suggesting that it is a metastable phase (Table 9.6).

4.1.4 Ferromagnetic (FM)

The 35 APs have the FM state as the lowest energy configuration (Table 9.5). Here, we have analyzed the magnetocrystalline anisotropy energy (MAE) calculated for three crystalline axes (Figure 4.2) and the MAEs are compiled in Table 9.5.

MAE of FM cubic APs

The MAE refers to the energy difference between two different magnetization axes:

$$MAE = E_{\mathrm{e1}} - E_{\mathrm{e2}} \tag{4.3}$$

where e1 and e2 are magnetization axes and [001], [110], and [111] magnetization axes are considered to determine the MAE of the cubic APs. Cubic compounds typically exhibit relatively small MAE values around a few μeV/atom. For instance, body-centered cubic (bcc) iron Fe shows a MAE of -0.4 μeV/atom with an easy axis aligned along [001] direction [60]. Likewise, the MAE of 28 of the 35 cubic APs is less than 10 μeV/atom (0.2-10 μeV/atom, Table 9.5). However, some APs such as Co_3LiN, Co_3PtN, Fe_3IrN, and Fe_3PdN show considerable MAE (41-59 μeV/atom, Table 9.5), with Fe_3IrN exhibiting the largest MAE (E_{001}-E_{111}) of -59.8 μeV/atom with [001] as an easy axis.

The magnetization direction of FM compounds can be aligned in a preferred direction using an external magnetic field [102]. The strength of the magnetic field required depends on the size of the MAE which is relatively small for cubic compounds. Therefore, the magnetization direction and thus the magnetic properties can be manipulated easily by an external magnetic field. For example, as shown for $Co_{60}Fe_{20}B_{20}$ [143], the measurement of the planar Hall effect shows that the transport properties can be altered by switching the magnetization directions. Therefore, we also investigated the anomalous Hall/Nernst conductivity (AHC/ANC) of FM cubic APs along the [001], [110], and [111] magnetization directions, which are discussed in Chapter 6 and Chapter 7.

5 Magnetostructural coupling

Magnetostructural coupling is a phenomenon in which the magnetic and structural properties of a material are interrelated, *i.e.*, a change in the crystal structure or lattice parameters induces change in magnetic properties, and vice versa. AP compounds exhibit strong magnetostructural coupling which is prominent in the cubic-to-cubic first-order transition wherein a change in the crystal volume brings about a change in the frustrated magnetic states [173]. In a recent study, the magnetostructural coupling of Mn_3NiN was explored through its spin-phonon coupling behavior [43]. In another study, a high-throughput screening was conducted to evaluate magnetostructural coupling in materials by examining the effect of the local magnetic configuration on the atomic forces [28]. In this chapter, we investigated the negative thermal expansion (NTE) and piezomagnetic effect (PME) in all 14 antiperovskite compounds with non-collinear magnetic ground states. These properties arise from the significant magnetostructural coupling exhibited by these materials. The NTE and PME are effects related to isotropic and anisotropic magnetostructural coupling, respectively. First, we modeled a paramagnetic (PM) state based on the disordered local moment (DLM) approach and verified the experimentally reported negative thermal expansion (NTE) behavior of non-collinear APs. We found that the PM state is crucial and cannot be approximated as a non-magnetic (NM) state. Second, we studied the PME by applying 0.5% and 1% of compressive and tensile biaxial strains. We found that APs exhibit a large net magnetization under 1% tensile strain and a few APs undergo a magnetic phase transition between Γ_{4g} and Γ_{5g}. [1]

5.1 Negative thermal expansion (NTE)

5.1.1 Modeling of paramagnetic state

The NTE behavior of AP materials is studied by evaluating the relative change in the lattice constants ($\Delta a/a_0$) between non-collinear magnetic ground state and PM state. In the given formula $\Delta a/a_0$, Δa represents the difference in the lattice constant between the PM and non-collinear state (Γ_{4g} or Γ_{5g}), and a_0 represents the lattice constant of

---

[1] The work presented in this chapter is part of our published papers [152].

the non-collinear state (Γ_{4g} or Γ_{5g}). The PM state is approximated using two different models. First, the PM state is approximated as a non-magnetic (NM) state. Second, the PM state is modeled based on the disordered local moment (DLM) approach, where a 2×2×2 supercell is generated using the Alloy Theoretic Automated Toolkit code (Figure 5.1) [179]. Within the DLM supercell approach, the PM state is modeled by treating the disordered moments as collinear AFM moments in a random up/down configuration (Figure 5.1) which corresponds to an $A_{50}B_{50}$ random alloy special quasi-random structure [216], where the pair correlations vanish for the strongest exchange interactions between the nearest neighbor sites [1]. The PM state, modeled based on the DLM supercell approach, provides a realistic representation and is sufficient to capture the volume effects.

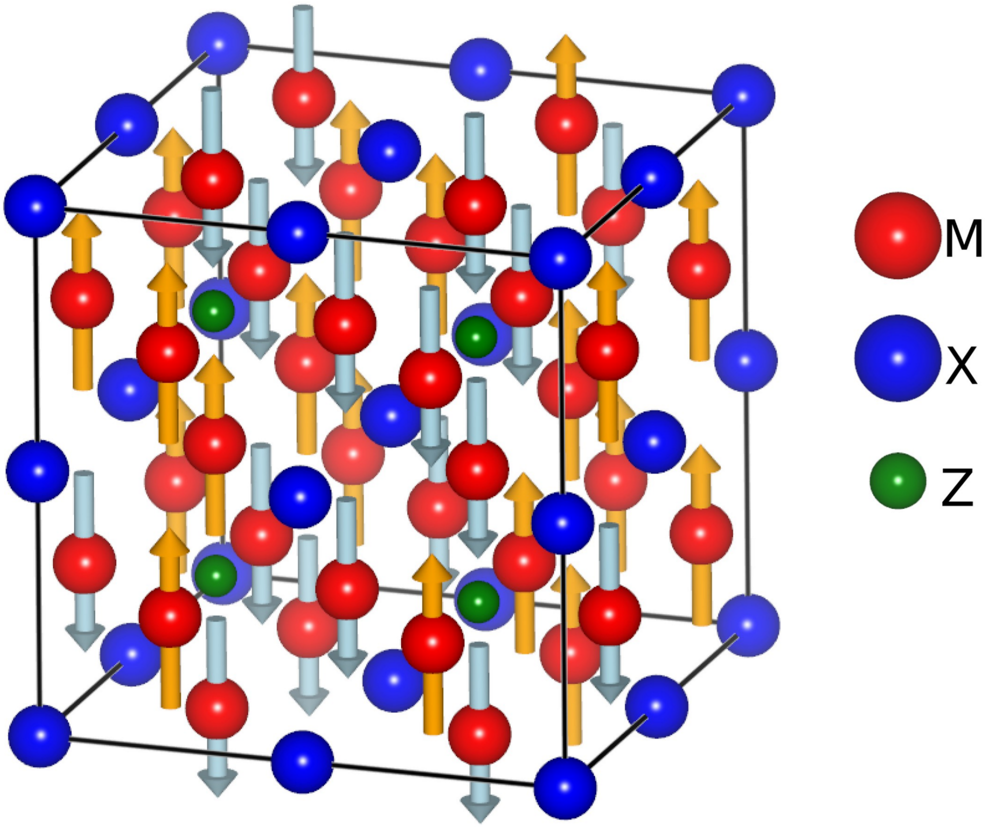

Figure 5.1: (a) The modeled PM structure of APs, obtained by generating a 2×2×2 supercell using ATAT code [179] based on DLM approach.

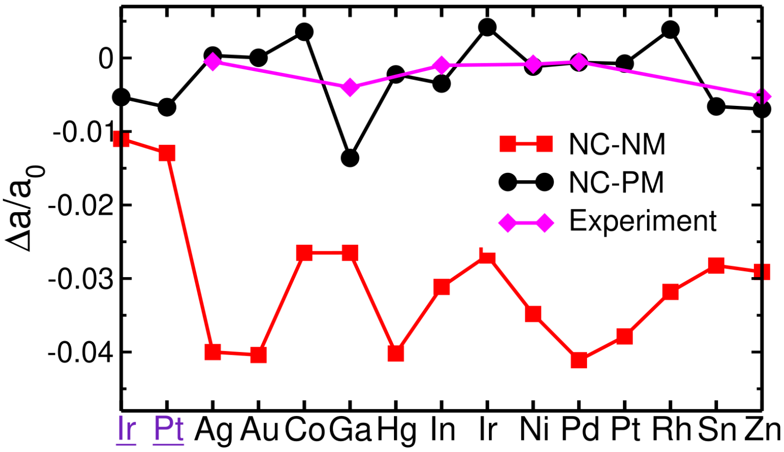

Figure 5.2: The calculated and experimentally measured [170] relative change in the lattice constant ($\Delta a/a_0$) for the $Cr_3\underline{X}N$ and Mn_3XN antiperovskites ($\underline{X}$ and X are the elements present on the x-axis in violet and black, respectively). The lattice constants of non-collinear (NC), paramagnetic (PM), and non-magnetic (NM) states are considered to calculate $\Delta a/a_0$.

5.1.2 Validation on experimentally known NTE antiperovskites

The calculated $\Delta a/a_0$ values are compared with the corresponding values observed in experimental measurements at the transition temperature to the PM state [36, 167, 170]. As shown in Figure 5.2, the calculated $\Delta a/a_0$ values using the PM state modeled based on DLM approach agree well with the experimentally observed values, except for Mn_3GaN. In the study by Takenaka *et al.* [170], Mn_3CoN, Mn_3RhN, and Mn_3SnN exhibit lattice expansion with the increasing temperature. However, the measured $\Delta a/a_0$ values for these compounds are not shown in Figure 5.2 due to difficulties in extracting the data from the referenced study [170]. Our calculations verify the experimental observations for Mn_3CoN and Mn_3RhN where both APs exhibit lattice expansion with positive $\Delta a/a_0$ values. However, Mn_3SnN show lattice contraction in our study (Figure 5.2). We assume that the mismatch with experimental observations for Mn_3GaN and Mn_3SnN can be attributed to finite temperature effects since we calculated the lattice constants of both the non-collinear and PM states at zero Kelvin. On the other hand, the $\Delta a/a_0$ calculated using the NM state are around five times larger than the experimentally measured values (Figure 5.2). Therefore, we posit that the PM state cannot be modeled as the NM state and a better estimation can be attained by considering the PM state as a collinear AFM configuration achieved using the DLM approach.

5.1.3 Prediction of novel NTE APs

Using the PM state based on the DLM approach, we found that Cr-based antiperovskites experience lattice contraction and exhibit $\Delta a/a_0$ values of -0.0053 and -0.0067 for Cr_3IrN and Cr_3Pt respectively, which are comparable to the reported NTE APs Mn_3GaN and Mn_3ZnN (Figure 5.2). Moreover, the $\Delta a/a_0$ values for the unreported Mn-based APs (Mn_3X X = Hg and Pt) are also negative. Thus, these compounds could be potential NTE materials. However, the equilibrium lattice constants for other Mn-based APs (Mn_3X X = Au, and Ir) increase on the transition from their non-collinear magnetic ground state to the PM state (Figure 5.2).

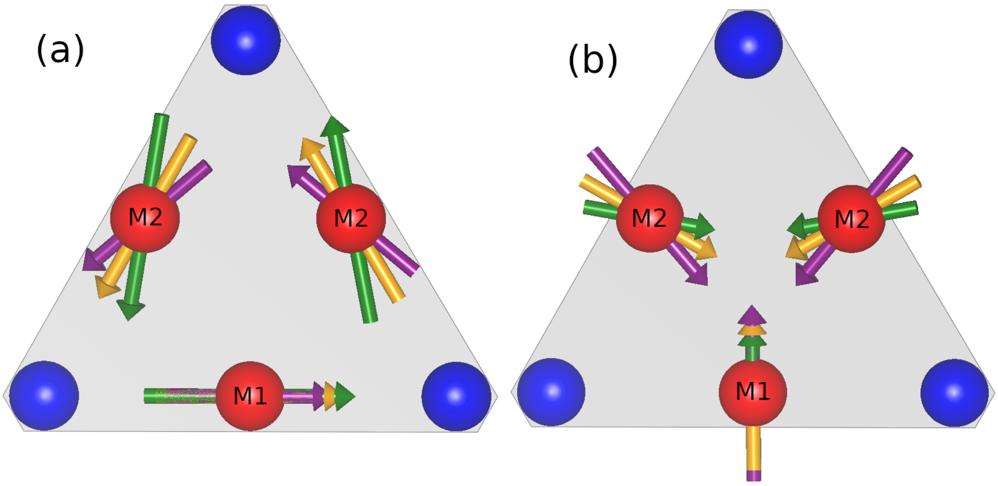

Figure 5.3: Spin configurations of local magnetic moments (LMMs) in the (111) plane for unstrained cubic and biaxially strained tetragonal structures of (a) Γ_{5g} and (b) Γ_{4g} non-collinear states. Yellow arrows indicate LMM direction in the unstrained cubic structure, while purple and green arrows represent magnetic spin direction under compressive and tensile biaxial strains, respectively. For better illustration the magnitude of spin canting angle is considered arbitrary.

5.2 Piezomagnetic effect (PME)

PME provides another effective characterization of the magnetostructural coupling [104], which manifests itself as the response of magnetization to strain. For the non-collinear AFM materials, the total bulk magnetization vanishes due to the cancellation of local magnetic moments. However, a net magnetization can be induced by introducing biaxial strain. The origin of PME in APs is elucidated in terms of symmetry, along with an illustration of spin configurations (Figure 5.3). Upon application of biaxial strain the cubic crystal space group symmetry (Pm$\bar{3}$m) of the AP compounds is lowered to tetragonal (P4/mmm). As a result, the local magnetic moments (LMMs) of the M atoms are reoriented, and the magnetic space group of the Γ_{4g} (Γ_{5g}) configurations is reduced from R$\bar{3}$m$'$ (R$\bar{3}$m) in the cubic structure to C2$'$/m$'$ (C2/m) in the tetragonal structure under biaxial strain.

The tetragonal structure has two in-equivalent crystallographic atomic positions, 1b and 2c, which are occupied by M1 and M2 atoms, respectively, in the (111) plane (Figure 5.3). The LMM of M1 atom in both Γ_{4g} and Γ_{5g} retain their spin direction whereas, the LMM of M2 atoms undergo reorientation of their spins in both non-collinear states. For compressive strain the LMM of the Mn2 atom rotates in the [110] direction while for tensile strainthe LMM rotates in the opposite direction of the compressive strain. Furthermore, in the case of the Γ_{5g} state, the magnetic moment of M1 and M2 atoms decreases with compressive strain and increases with tensile strain. On the other hand, for the Γ_{4g} state, the magnetic moment of M1 and M2 atoms decreases with tensile strain and increases with compressive strain (Figure 5.3).[2]

5.2.1 Validation of PME on reported Mn-Based AP nitrides

In a recent study by Zemen *et al.* [206], the PME of Mn-based APs (Mn_3X where X = Ag, Co, Ga, I Ni, Pd, Rh, S and Zn) were calculated in the Γ_{4g} state for a tensile strain of 1%. The net magnetization obtained from our calculations is in good agreement with their study (Figure 9.2), except for the Mn_3CoN and Mn_3RhN. The net magnetization calculated from our study (in the study by Zemen*et al.*) is 0.646 μ_B/f.u. (0.305 μ_B/f.u.) for Mn_3CoN and 0.214 μ_B/f.u. (-0.143 μ_B/f.u.) for Mn_3RhN. Note that for Mn_3CoN the local magnetic moment of the Co atom is zero in the cubic structure, while a net magnetic moment of 0.362 μ_B/f.u. is induced under 1% tensile strain. Interestingly, the magnetic spin direction of the Co atom is aligned with a plane, similar to the non-collinear magnetic direction of the Mn atom.

---

[2] The PME is evaluated by applying biaxial compressive and tensile strains of 0.5% and 1.0% in the ab plane. The optimal lattice constants along the c-direction are determined through a polynomial Birch-Murnaghan fitting of the energies obtained from a series of calculations, while keeping the atomic positions fixed.

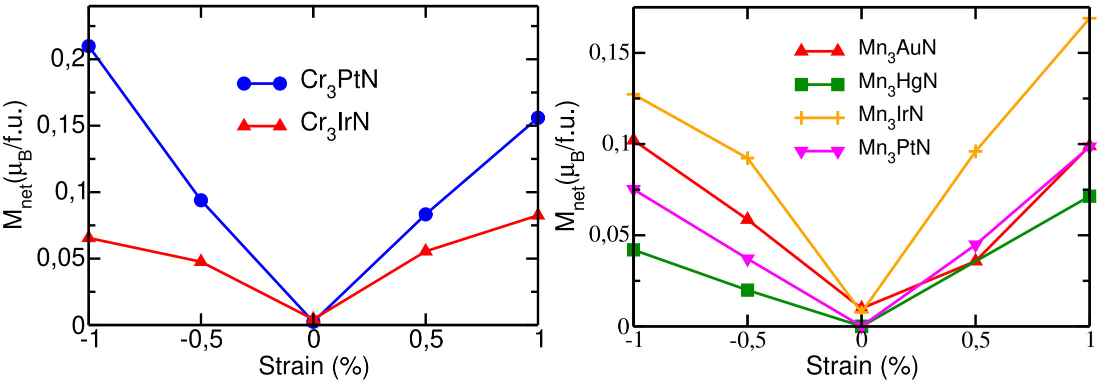

Figure 5.4: The calculated net magnetization for the unreported Cr-based (left) and Mn-based (right) AP nitrides. Mn_3AuN and Mn_3IrN exhibit convergence to a non-zero net magnetization (right).

5.2.2 PME of unreported APs

The net magnetization of unreported APs is presented in Figure 5.4. We found that the net magnetization is asymmetric under compressive and tensile biaxial strains and exhibits a larger PME under tensile strain (Figure 5.4 and 9.3), except for Cr_3PtN. If this system exposed to 1% compressive strain the net magnetization is 0.21 μ_B/f.u., whereas at 1.0% tensile strainit shows 0.15 μ_B/f.u.

5.2.3 Phase transition ($\Gamma_{4g} \leftrightarrow \Gamma_{5g}$)

The total energy difference (ΔE_{tot}) between Γ_{5g} and Γ_{4g} is determined using equation 4.1 to identify the magnetic ground state under compressive and tensile strains. Most of the APs preserve their magnetic ground state of the cubic phase under both biaxial strains. However, as highlighted in Table 9.7, a few APs undergo a magnetic phase transition between $\Gamma_{4g} \leftrightarrow \Gamma_{5g}$ under the given biaxial strain leading to a substantial change in transport properties, as discussed in the next chapter. For example, Mn_3AuN exhibits a Γ_{5g} state in the cubic phase and preserves its magnetic ground state under tensile strains of 0.5% and 1.0%. However, under compressive strain of -0.5% and -1.0%, it undergoes a magnetic phase transition to a Γ_{4g} state, with corresponding ΔE_{tot} values of 0.127 and 0.358 meV/atom, respectively. Lastly, no consistent trend of ΔE_{tot} is observed for APs under biaxial strains.

6 Anomalous Hall conductivity

The anomalous Hall conductivity (AHC) of 35 ferromagnetic (FM) and 14 non-collinear antiperovskites is studied, and the AHC of non-collinear APs is also investigated under compressive and tensile strains. As we know, the AHC in FM compounds originates from the broken time-reversal symmetry in the presence of spin-orbit coupling. Whereas, non-collinear AFM compounds can also show a non-zero AHC depending on the magnetic spin configuration. For example, APs with Γ_{4g} state show a non-zero AHC, while Γ_{5g} phase leads to zero AHC. Under biaxial strain, both Γ_{4g} and Γ_{5g} exhibit a non-zero AHC. In this chapter, we first discuss the reasons for the vanishing or non-vanishing AHC components based on symmetry examination. In this regard, the Berry curvature (Ω) transformation is shown under various symmetry operations. Our AHC calculations correspond well with the symmetry analysis. It is found that FM compounds have a larger AHC than non-collinear APs in the cubic phase. For example, the FM APs show a large AHC of more than 1000 S/cm for Co_3LiN and Co_3ZnN. Lastly, based on electronic structure analysis, we found that the AHC peak originates due to the presence of Weyl nodes in the vicinity of the peak. With the application of biaxial strain, the AHC peak can be shifted to the Fermi-energy attributed to the shift of Weyl points. [1]

6.1 Symmetry analysis

The vanishing or non-vanishing of the AHC tensor elements can be determined based on the symmetry of the magnetic space group, where the corresponding symmetry operations result in a specific distribution of the Berry curvature in **k**-space $\Omega(\mathbf{k})$, which determines whether the AHC is zero or non-zero. The principles governing the transformation of Berry curvature under various symmetry operations are described in Ref [165]. In short, a few fundamental symmetry operations are mentioned. First, the Berry curvature $\Omega(\mathbf{k})$ is invariant under any translation operation of the Bravais lattice. Second, if time-reversal symmetry is present, time-reversal transforms $\Omega(\mathbf{k})$. Third, if spatial inversion symmetry is present, spatial inversion yields $\Omega(\mathbf{k})$ to $\Omega(-\mathbf{k})$. The transformation of the Berry curvature Ω $(\mathbf{k})$ under any symmetry operation depends on the relative orientation between the

---

[1] The results discussed in this chapter are part of published papers [152, 149].

Berry curvature component and the corresponding symmetry operation, which determines whether the Berry curvature is zero or non-zero. For instance, when the Berry curvature is parallel to a mirror plane, the related mirror operation transforms $\Omega(\mathbf{k})$ to -$\Omega(\hat{m}\mathbf{k})$, resulting in zero Berry curvature. This is because the Berry curvature is canceled out at **-k** and **k** by Brillouin-zone integration. Conversely, if the Berry curvature is perpendicular to a mirror plane, it remains invariant, leading to non-zero Berry curvature.

The Berry curvature ($\Omega_{\alpha\beta}$) and AHC ($\sigma_{\alpha\beta}$) can be categorized as pseudo-vectors ({α,β} = {x,y,z}, with $\alpha{\neq}\beta$, represents the Cartesian coordinates), and their vector-form notations can be expressed as $\Omega_{\alpha\beta} = [\Omega_{yz}, \Omega_{zx}, \Omega_{xy}] = [\Omega_x, \Omega_y, \Omega_z]$ and $\sigma_{\alpha\beta} = [\sigma_{yz}, \sigma_{zx}, \sigma_{xy}] = [\sigma_x, \sigma_y, \sigma_z]$, respectively. In the next subsection, the Berry curvature transformation under specific symmetry operations is discussed for the FM and non-collinear magnetic configurations of APs (Figure 4.2 and 4.1). The magnetic space group and AHC tensor elements were calculated using a linear response symmetry code developed by Jakub Železný [99]. The magnetic space group and the corresponding AHC tensor elements for the FM magnetization direction [001], [110], and [111] and for the non-collinear AFM configurations Γ_{4g}/Γ_{5g} are summarized in the Table 9.9 and 9.8, respectively.

6.1.1 Ferromagnetic APs

Magnetization direction [001]

The magnetic space group for the magnetization direction [001] is P4/mm′m′ (123.345) and has sixteen symmetry operations [9]. The Berry curvature components Ω_x and Ω_y are invariant under half of the symmetry operations, and for the other half of the symmetry operations, the sign of Ω_x and Ω_y changes, leading to zero values for the Ω_x and Ω_y components. In contrast, the Ω_z component is invariant under all sixteen symmetry operations, resulting in non-zero values of Ω_z component. For example, the transformation of the Berry curvature is presented under two individual symmetry operations, the two-fold rotation axis ($C_{2_{001}}$) and the mirror plane M_{001}. Under both symmetry operations, the signs of Ω_x and Ω_y change, while Ω_z remains invariant. For $C_{2_{001}}$, the Berry curvature transforms according to the following equations:

$$\begin{aligned}
\Omega_x\left(-k_x,-k_y,k_z\right) &= -\Omega_x\left(k_x,k_y,k_z\right) \\
\Omega_y\left(-k_x,-k_y,k_z\right) &= -\Omega_y\left(k_x,k_y,k_z\right) \\
\Omega_z\left(-k_x,-k_y,k_z\right) &= \Omega_z\left(k_x,k_y,k_z\right)
\end{aligned}$$

For M_{001}, The Berry curvature is described by the following equations:

$$\begin{aligned}
\Omega_x\left(k_x, k_y, k_z\right) &= -\Omega_x\left(k_x, k_y, -k_z\right) \\
\Omega_y\left(k_x, k_y, k_z\right) &= -\Omega_y\left(k_x, k_y, -k_z\right) \\
\Omega_z\left(k_x, k_y, k_z\right) &= \Omega_z\left(k_x, k_y, -k_z\right)
\end{aligned}$$

As a result, k-space integration of Ω_x and Ω_y lead to zero values of σ_x and σ_y, while Ω_z gives rise to a non-zero value of σ_z, confirming the results of our calculations for Fe_3IrN, where σ_z is 852 S/cm at the Fermi energy (E_f) and Ω_x and Ω_y are zero (Figure 9.5).

Magnetization direction [110]

There are eight symmetry operations for the magnetic space group 65.486 (Cmm′m′) [10]. The Ω_x and Ω_y components are invariant under all eight symmetry operations, while the Ω_z component changes sign under four symmetry operationsand remains invariant for the other four, leading to vanishing Ω_z. For example, under the mirror-plane symmetry combined with time-reversal symmetry M'_{001}, Ω_z vanishes, while Ω_x and Ω_y are invariant. The Berry curvature transforms according to the following relation:

$$\begin{aligned}
\Omega_x\left(-k_x, -k_y, k_z\right) &= \Omega_x\left(k_x, k_y, k_z\right) \\
\Omega_y\left(-k_x, -k_y, k_z\right) &= \Omega_y\left(k_x, k_y, k_z\right) \\
\Omega_z\left(-k_x, -k_y, k_z\right) &= -\Omega_z\left(k_x, k_y, k_z\right)
\end{aligned}$$

Therefore, Ω_x and Ω_y result in finite values of σ_x and σ_y, and Ω_z leads to a vanishing value of σ_z, which verifies our calculated AHC for Fe_3IrN. In this case, σ_x is equal to σ_y with a value of 510.1 S/cm, and σ_z is zero (Figure 9.5).

Magnetization direction [111]

The magnetic space group associated with the magnetization direction [111] is R-3m′ (166.101) and has 12 symmetry symmetry operations [11]. The Berry curvature components are invariant under all the corresponding symmetry operations, resulting in a finite AHC for all three components with the same value ($\sigma_x = \sigma_y = \sigma_z$). This agrees well with our calculated AHC for Fe_3IrN, where all three components have the same AHC value of 520 S/cm (Figure 9.5).

6.1.2 Non-collinear APs

The non-collinear AFM structure show finite AHC in presence of spin-orbit coupling for certain magnetic configurations which are discussed in the next subsections.

Cubic Γ_{4g}

For the cubic Γ_{4g} phase, the magnetic space group is R$\bar{3}$m′ (166.101), and none of the corresponding symmetry operations [11] enforce any of the Berry curvature components to vanish. There are three mirror planes: $M_{(0\bar{1}1)}$, $M_{(10\bar{1})}$, and $M_{(\bar{1}10)}$. These mirror planes also combine with time-reversal symmetry to form $M'(0\bar{1}1)$, $M'(10\bar{1})$, and $M'_{(\bar{1}10)}$. The Berry curvature transformation under each mirror symmetry operations are listed in Ref [59]. For instance, the Berry curvature transforms for $M'_{(\bar{1}10)}$ according to the following equations:

$$\begin{aligned}\Omega_x\left(k_y,k_x,k_z\right)=\Omega_y\left(-k_x,-k_y,-k_z\right)\\ \Omega_y\left(k_y,k_x,k_z\right)=\Omega_x\left(-k_x,-k_y,-k_z\right)\\ \Omega_z\left(k_y,k_x,k_z\right)=\Omega_z\left(-k_x,-k_y,-k_z\right)\end{aligned}$$

Therefore, all AHC components are finite, where $\sigma_x=\sigma_y=\sigma_z$. Our calculations are consistent with the symmetry analysis, as illustrated in Figure 9.4, for Cr_3IrN.

Cubic Γ_{5g}

The associated magnetic space group for the Γ_{5g} phase is R$\bar{3}$m (166.97) [12]. There are three mirror planes: $M_{(0\bar{1}1)}$, $M_{(10\bar{1})}$, and $M_{(\bar{1}10)}$. The Berry curvature transforms in case of $M_{(\bar{1}10)}$ according to the following equations:

$$\begin{aligned}\Omega_x\left(k_y,k_x,k_z\right)=-\Omega_y\left(k_x,k_y,k_z\right)\\ \Omega_y\left(k_y,k_x,k_z\right)=-\Omega_x\left(k_x,k_y,k_z\right)\\ \Omega_z\left(k_y,k_x,k_z\right)=-\Omega_z\left(k_x,k_y,k_z\right)\end{aligned}$$

Our calculation verifies the symmetry observation as shown in Figure 9.4 for Mn_3PtN, where all three AHC components have zero value.

Tetragonal Γ_{4g}

The tetragonal Γ_{4g} phase is obtained by applying biaxial strain to the cubic Γ_{4g} phase, resulting in the reduction of the crystal (magnetic) space group symmetry in the cubic phase from Pm$\bar{3}$m (R$\bar{3}$m′) to P4/mmm (C2′/m′) [13]. In the tetragonal Γ_{4g} phase, all the Berry curvature components are invariant under the corresponding symmetry operations. Therefore, the AHC components are finite, where $\sigma_x = \sigma_y$, while the σ_z component has a different value (Figure 9.4(a)).

Tetragonal Γ_{5g}

The Γ_{5g} phase exhibits finite AHC, unlike the cubic Γ_{5g} phase, and the resulting magnetic space group is $C2/m$ (12.58). The corresponding symmetry operations [14], such as $C_{2_{010}}$ and $M_{(010)}$, vanish Ω_z, while Ω_x and Ω_y remain invariant. The Berry curvature transforms as follows:

$$\begin{aligned}
\Omega_x\left(k_y,-k_x,-k_z\right) &= \Omega_y\left(k_x,k_y,k_z\right)\\
\Omega_y\left(k_y,-k_x,-k_z\right) &= \Omega_x\left(k_x,k_y,k_z\right)\\
\Omega_z\left(k_y,-k_x,-k_z\right) &= -\Omega_z\left(k_x,k_y,k_z\right)
\end{aligned}$$

Therefore, the AHC σ_x and σ_y components are finite, where $\sigma_x = -\sigma_y$ with opposite signs, while the σ_z component is zero (Figure 9.4(b)).
Overall, our calculations agree with the symmetry analysis for the 35 FM APs and 14 non-collinear AFM APs.

6.2 Giant AHC in FM APs

The AHC for the FM cubic APs are summarized in Table 9.13.[2] The cubic FM APs exhibit giant AHC values of 1128 S/cm and 1068 S/cm for Co_3LiN and Co_3ZnN, respectively, when the magnetization direction is [111]. The calculated AHC of these two FM compounds is larger than that of bcc Fe (750 S/cm) [199, 188] and close to that of Fe_3Sn_2 (1100 S/cm) [200] and of the Weyl semimetal $Co_3Sn_2S_2$ (1130 S/cm) [101]. Next, we found that the AHC can be significantly altered by changing the direction of magnetization. Taking an example of Co_3LiN, the AHC decreases from 1128 S/cm to 126 S/cm when the magnetization direction is changed from [111] to [110] (Figure 6.1). Additionally, we

---

[2] The AHC is a pseudo-vector which is aligned with the high-symmetry magnetization directions [001], [110], and [111], as has been reported for tetragonal alloys such as 3dPt (3d = Fe, Co, and Ni) [207]. A positive (negative) sign for AHC indicates that it is parallel (anti-parallel) to the magnetization direction. Therefore, we define the AHC for magnetization directions [001], [110], and [111] using these equations: $\sigma_{[001]} = \sigma_z$, $\sigma_{[110]} = \frac{1}{\sqrt{2}}(\sigma_x + \sigma_y)$, and $\sigma_{[111]} = \frac{1}{\sqrt{3}}(\sigma_x + \sigma_y + \sigma_z)$. From now on, for the FM APs, we use AHC values obtained from these equations.

observed that changing the direction of magnetization may not only alter the magnitude of AHC, but also reverse its sign. For instance, in Co_3MgC, the AHC is 283 S/cm for the [001] magnetization direction, but it becomes negative (-291 S/cm) when the magnetization is oriented along the [111] direction (Figure 9.7(9)). A similar AHC behavior is observed for Co_3RhN, Co_3SnC, Co_3ZnC, Fe_3AlC, and Ni_3CuC (Table 9.13). The AHC with respect to the chemical potential are plotted in Figure 9.7.

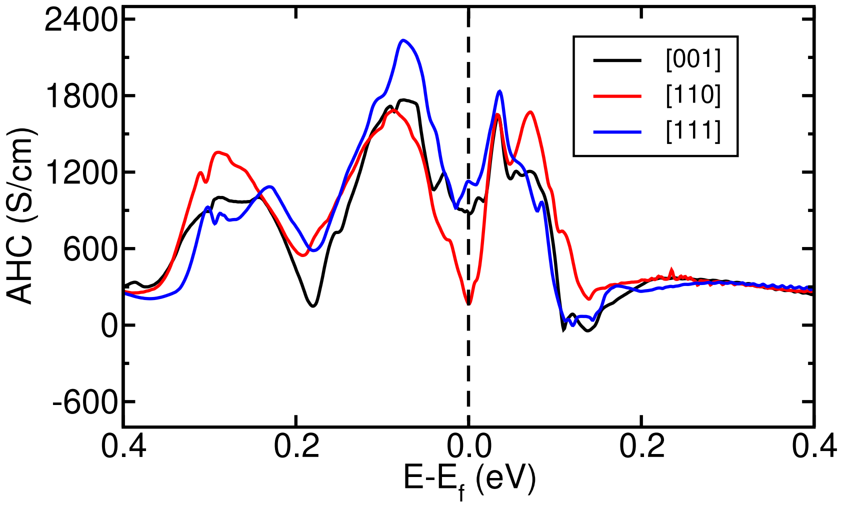

Figure 6.1: The calculated AHC of Co_3LiN for FM [001], [110], and [111] magnetization directions.

6.3 AHC in non-collinear AFM APs

The AHC is calculated for the non-collinear APs in their respective magnetic ground state, as listed in Table 4.1 and 9.7.

6.3.1 AHC in cubic Γ_{4g}/Γ_{5g}

The AHC is zero for the Γ_{5g} AFM state (Mn_3XN, where X = Au, Hg, In, Pt, and Zn (Figure 9.4 and 9.8)). On the other hand, APs with the Γ_{4g} ground state exhibit significantly larger AHC, such as Cr_3IrN and Cr_3PtN, which have AHC values of 414 and 278 S/cm, respectively.

The AHC of non-collinear APs are provided in the Figure 9.4 and 9.8.[3]

Validation on reported cubic Γ_{4g} APs

Our calculated AHC values for Mn_3NiN (-165 S/cm) agree well with those reported by Boldrin *et al.* (-170 S/cm [15]) and Zhou *et al.* (-174 S/cm [213]). Similarly, our calculated AHC value for Mn_3GaN (-60 S/cm) is in good agreement with the value of -57 S/cm reported by Zhou *et al.*. However, the overall comparison of AHC with previous studies for the same compound is scattered, as shown in Table 9.10. For example, our calculated AHC value for Mn_3SnN is 106.5 S/cm, which differs from the value (133 S/cm) obtained by Gurung *et al.* [59]. In contrast, the AHC value reported in the study by Huyen *et al.* [75] is -73.9 S/cm, which is of the opposite sign and smaller in magnitude compared to our calculated AHC value. The discrepancies in AHC values reported in different studies could be due to the use of different lattice constants and numerical parameters in the calculations. The mismatch in the AHC sign might be caused by the chirality of the non-collinear spin configurations considered in the calculations.

6.3.2 AHC in tetragonal Γ_{4g}/Γ_{5g}

The AHC can be manipulated by applying biaxial strain, as shown in Figure 9.8. The Γ_{4g} compounds exhibit significant changes in AHC. For example, Cr_3IrN achieves an AHC value of 693 S/cm (σ_z component) under 1% tensile strain, compared to 414 S/cm in the cubic phase (Figure 9.4(a)). On the other hand, Mn_3InN and Mn_3ZnN exhibit small AHC values for Γ_{5g} due to their weak spin-orbit coupling strength. Additionally, applying biaxial strain can lead to a change in the sign of AHC (σ_z component), as observed for Mn_3AgN and Mn_3CoN under 0.5% compressive and 1% tensile strain, respectively (Figure 9.8).

Correlation between biaxial induced AHC and PME

One interesting question is how biaxial-induced AHC and net magnetization (PME) are correlated (Figure 6.2). To answer this, we evaluated $|\Delta\text{AHC}|$, which is the change in AHC between the tetragonal phase (1% tensile strain) and the cubic phase. We observed that $|\Delta\text{AHC}|$ cannot be directly deduced from the induced net magnetization. For example, in the case of Cr_3IrN, the net magnetization is small (0.082 μ_B/f.u.), but $|\Delta\text{AHC}|$ is large for the σ_z component (278.5 S/cm). In contrast, for Mn_3SnN, the net magnetization

---

[3] In this thesis, the AHC of Mn_3GaN and Mn_3NiN is reproduced and therefore not shown. These compounds have been previously studied and reported in our group's works by Samathrakis *et al.* [140, 15].

is large (0.47 μ_B/f.u.) but |ΔAHC| is small (35.5 S/cm, σ_z component). However, for Mn_3CoN, both the net magnetization (0.646 μ_B/f.u.) and |ΔAHC| (250.7 S/cm, σ_x) are significantly large. Therefore, it can be assumed that |ΔAHC| could be small for large net magnetization and vice versa (Figure 6.2). Interestingly, both the net magnetization and |ΔAHC| are smaller for compounds having Γ_{5g} magnetic ground state, compared to the Γ_{4g} state. For instance, in the case of Mn_3ZnN, the net magnetization and |ΔAHC| are 0.029 μ_B/f.u. and 9.17 S/cm, respectively.

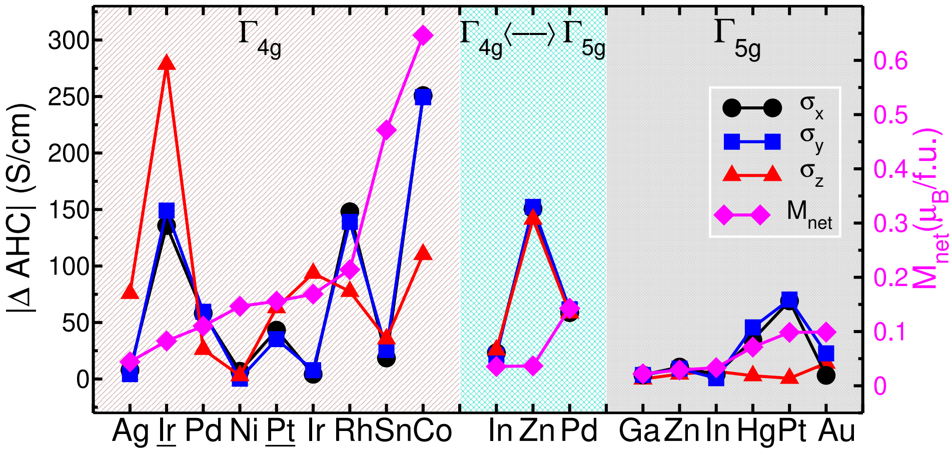

Figure 6.2: The change in AHC (|ΔAHC|) between the tetragonal (1% tensile strain) and cubic phases and the net magnetization at 1% tensile strain (considered to be due to the large net magnetization) are illustrated for the $Cr_3\underline{X}N$ and Mn_3XN antiperovskites (where X̲ and X represent the elements present on the x-axis, respectively). The left, middle, and right panels represent the antiperovskites with Γ_{4g} phase, compounds for which a phase transition occurred between Γ_{4g} and Γ_{5g} state, and Γ_{5g} state, respectively.

6.4 Weyl points analysis

To understand the origin of AHC in both cubic and biaxial-induced tetragonal phases, we performed a detailed analysis of the electronic structure. Our analysis reveals that the tunability of AHC by biaxial strain can be attributed to the presence of Weyl points. For example, Mn_3PdN has 12 Weyl points located at fractional coordinates (0.43, -0.35, -0.49) and equivalent k-points. In the cubic phase, these Weyl points are located -20 meV below the Fermi level. With the application of compressive strain, the Weyl points shift

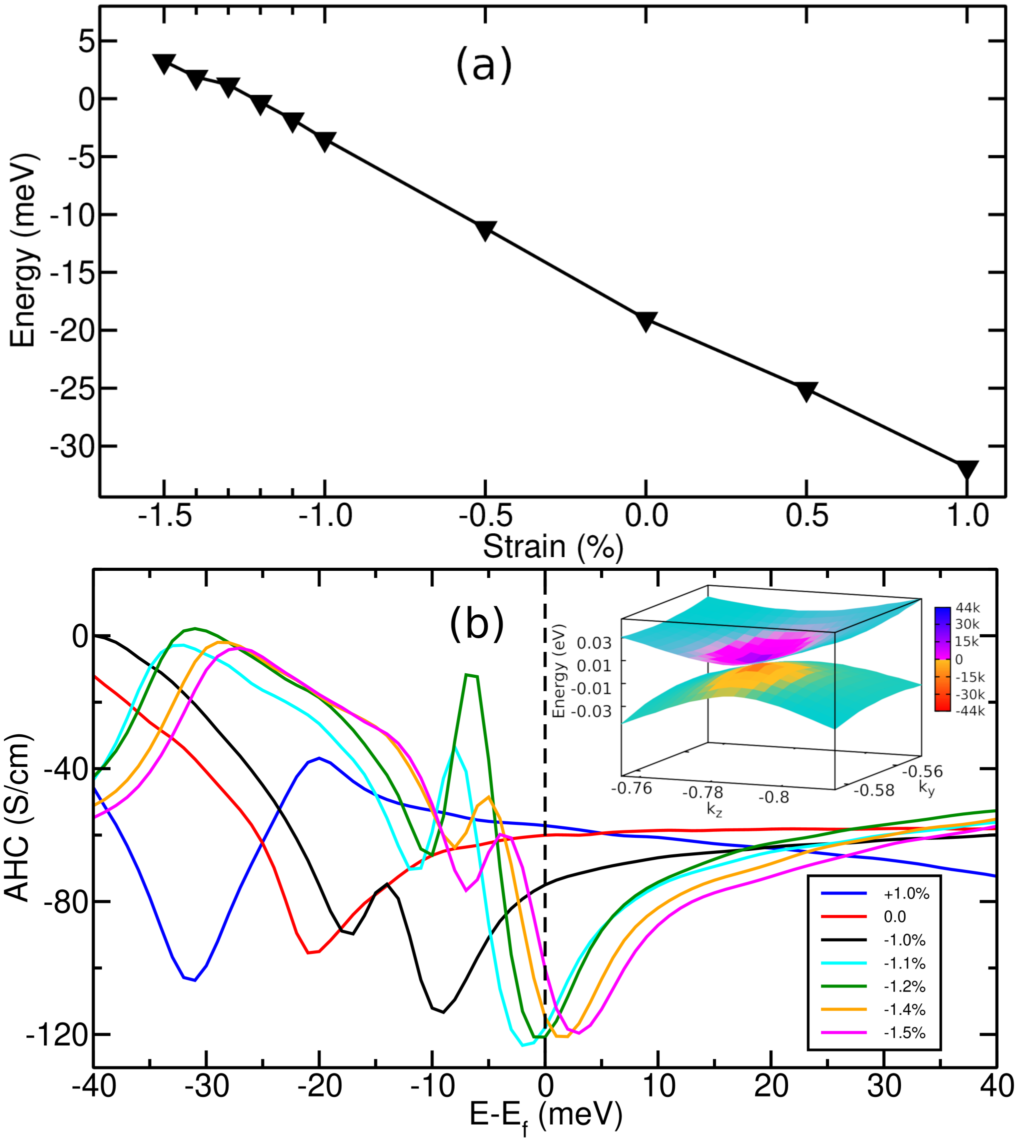

Figure 6.3: Analysis of Mn_3PdN in the Γ_{4g} magnetic state in both cubic and biaxial-induced tetragonal phases. (a) The Weyl points (located at 0.43, −0.35, −0.49, and equivalent coordinates) move across the Fermi-level under compressive strain. (b) The calculated AHC (σ_z component) and Berry curvature (inset above) for -1.4% compressive biaxial strain. The units of the inset color bar are in square angstroms (Å^2).

closer to the Fermi energy at -1.75 meV for -1.3% biaxial strain, cross the Fermi energy between -1.3% and -1.4% strain, reaching 1.87 meV above the Fermi energy at -1.4% strain (Figure 6.3(a)). As a result, the AHC inverted peak also shifts as the Weyl points move towards the Fermi-energy. As shown in the Figure 6.3(b), the AHC inverted peak is situated at -21 meV with an AHC of -95 S/cm for zero strain. Under a compressive strain of -1.2%, the AHC inverted peak is shifted to the Fermi energy and exhibits an AHC of -121 S/cm. For -1.4% strain, the AHC inverted peak has crossed the Fermi energy, and is located at 2 meV and exhibiting an AHC of -121 S/cm. Note that the AHC inverted peak is located in the vicinity of the Weyl points as a consequence of the singular behavior of the Berry curvature at the Weylnodes (Figure 6.3(b) inset).

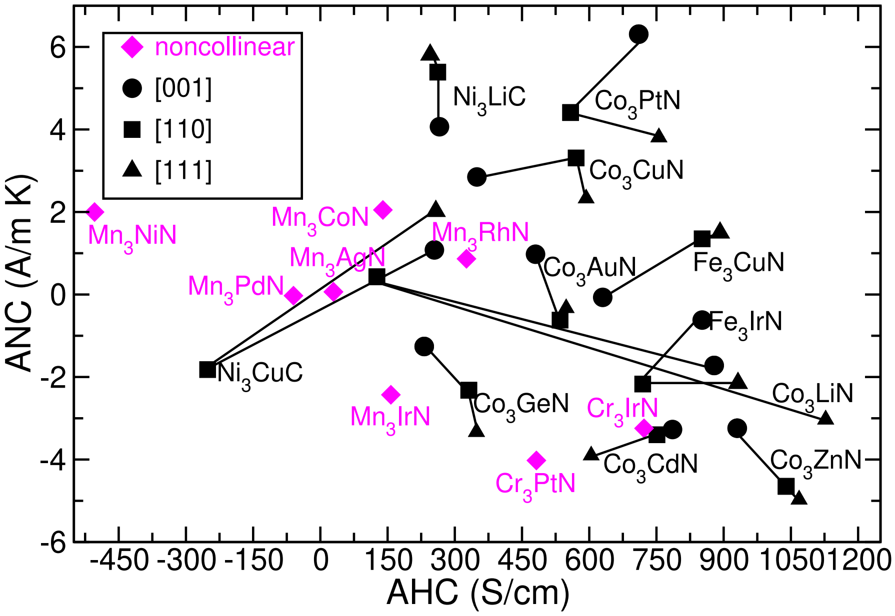

Figure 6.4: The comparison of AHC and ANC between non-collinear and FM antiperovskite compounds. The black solid line connects the FM [001], [110], and [111] magnetization directions for the given AP compound. The AHC and ANC values at the Fermi energy are plotted, the AHC values obtained from the equations in the footnote[2,4] are used. The ANC values are calculated at 300 K (discussed in the next chapter). The plotted FM compounds have either absolute AHC values larger than 300 S/cm or absolute ANC values greater than 2 A/mK.

6.5 Comparison of AHC between FM and non-collinear Γ_{4g}

As shown in the Figure 6.4, the FM cubic APs frequently have larger AHC values compared to the non-collinear AFM compounds.[4] For instance, Co_3LiN exhibits the largest AHC value of 1128 S/cm among FM APs, which is more than 1.5 times larger than the largest AHC value of 722 S/cm obtained for non-collinear AFM Cr_3IrN. We found that six ferromagnetic APs surpass the maximum AHC value (722 S/cm) observed for the non-collinear AFM Cr_3IrN. However, it is not guaranteed that the FM state will have a higher AHC than the non-collinear AFM state when comparing AHC values for a given AP in both the states (Table 9.11). For example, Cr_3IrN has larger AHC in its non-collinear Γ_{4g} (722 S/cm) magnetic ground state compared to the FM state (252 S/cm). Similarly, for Co_3PtN, the AHC is higher (1465 S/cm) in the hypothetical non-collinear Γ_{4g} compared to its FM ground state (710 S/cm) with magnetization direction [001].

---

[4] The AHC values of cubic non-collinear Γ_{4g} APs are converted into hexagonal lattice along (111) plane using the formula $\sigma_{\Gamma_{4g}} = \frac{1}{\sqrt{3}}(\sigma_x + \sigma_y + \sigma_z)$.

7 Anomalous Nernst conductivity

In this chapter, we present the results of anomalous Nernst conductivity (ANC) [152, 149], which is evaluated for 35 FM APs and 8 non-collinear compounds with Γ_{4g} magnetic ground state. The ANC (α) is calculated at 300 K using the generalized Mott formula (Equation 9.3, [196, 212]), which is applicable to a higher temperature range. The symmetry analysis for ANC is similar to that of AHC.[1] However, a finite AHC does not necessarily imply a finite ANC. If the slope of the energy derivative of AHC is zero, then ANC is also zero. We first discuss the ANC of FM APs and its tunability with magnetization direction. Next, we illustrate the interrelation of magnetization ($\mathbf{M}$), thermal gradient ($\nabla\mathbf{T}$), and electric current ($\mathbf{I}$) through a thermopile structure. Then, we demonstrate Weyl point analysis to understand the origin of giant ANC in the FM Co_3PtN compound. Finally, we present the ANC of non-collinear APs and compare them with FM AP compounds.

7.1 Giant ANC in FM APs

The FM APs exhibit giant ANC. For instance, for the magnetization axis [001], Co_3PtN demonstrates an ANC of 6.31 A/mK, which is close to the cubic FM counterpart compound Fe_3Pt (6.2 A/mK) [137] and larger than the experimentally reported ANC in cubic Heusler compounds such as Co_2MnGa (4.0 A/mK) and Co_2FeGe (3.16 A/mK) [57, 122]. Likewise, for the [111] magnetization direction, Co_3ZnN and Ni_3LiC attain an ANC of -4.97 and 5.81 A/mK, respectively. Overall, seven AP compounds exhibit an ANC larger than 3.0 A/mK (Table 9.13). The ANC as a function of chemical potential is summarized in Figure 9.9.

7.1.1 Validation of ANC with previous study

In Ref. [137], the ANC of nine ferromagnetic APs is reported. However, the APs with large ANC from our study were not included in their study (Table 9.12). The provided

---

[1] Like AHC, the ANC can also be defined for magnetization axis [001], [110], and [111] using these equations: $\alpha_{[001]} = \alpha_z$, $\alpha_{[110]} = \frac{1}{\sqrt{2}}(\alpha_x + \alpha_y)$, and $\alpha_{[111]} = \frac{1}{\sqrt{3}}(\alpha_x + \alpha_y + \alpha_z)$. Similarly, the ANC of Γ_{4g} state can be defined as: $\alpha_{[\Gamma_{4g}]} = \frac{1}{\sqrt{3}}(\alpha_x + \alpha_y + \alpha_z)$

ANC values (α_z) in their study were calculated at Fermi-energy below 500 K without any additional details such as the exact temperature, maximum ANC (α_z) values obtained, or AHC plots or data. Therefore, a systematic comparison is not possible for the ANC analysis since we have calculated the ANC at 300 K.[2]

7.1.2 Tuning of ANC via magnetization directions

Similar to AHC, it is possible to tune the ANC by changing the magnetization axis in terms of both magnitude and sign (Table 9.13). For example, in the case of Co_3PtN, the ANC changes from 6.31 A/mK to 3.81 A/mK by switching the magnetization axis from [001] to [111]. The change of ANC sign depends on the derivative of AHC slope ($d\sigma_{xy}/d\epsilon$, equation 9.3). Taking the example of Co_3LiN, tuning the magnetization axis from [111] to [110] changes the ANC ($d\sigma_{xy}/d\epsilon$) and, thus, its sign from -3.03 A/mK (5318 S/cm.eV) to 0.43 A/mK (-5190 S/cm.eV).

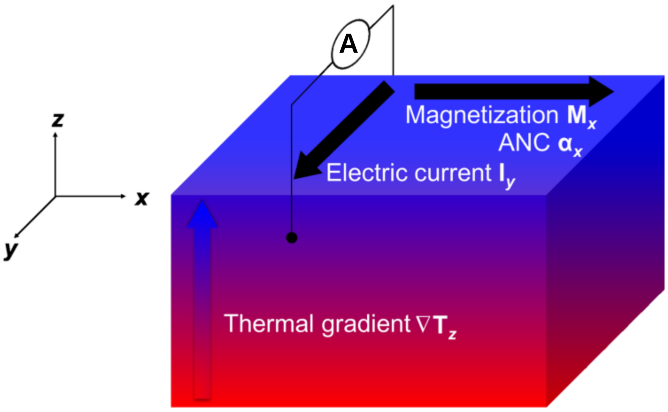

Figure 7.1: Schematic illustration of the thermopile structure for in-plane thermal gradient (∇T_z) and magnetization (M_x) resulting in an electric current (I_y) in the y-direction.

7.1.3 Thermopile structure

The practical thermopile structure shown in Figure 7.1 summarizes the mechanistic interplay between magnetization (**M**), thermal gradient (∇**T**), and electric current (**I**). We

---

[2] The results discussed in this chapter are part of published papers [152, 149].

assume that an out-of-plane thermal gradient ($\nabla \mathbf{T_z}$) is applied, and, the magnetization is aligned in-plane, i.e., $\mathbf{M}_z$, which generates an electric current ($\mathbf{I_y}$) in the y-direction (Fig. 7.1).

Similar to AHC, ANC can also be aligned with the high-symmetric magnetization axis(Chapter 6, footnote 2). For instance, in Co_3LiN, by tuning the magnetization axis from [001] to [110], the negative value of ANC (-1.72 A/mK) changes to a positive value (0.43 A/mK). Concerning the thermopile mechanism, this change leads to the generation of an electric current (**I**) along the -y and y-axes if the thermal gradient ∇T_z is applied along the z-axis for an in-plane magnetization $\mathbf{M}_x \parallel [001]$ (Figure 7.1(a)). In the experimental study conducted by Isogami *et al.* [78], it is demonstrated that the Nernst voltage for the Fe_4N antiperovskite can be altered from 0.58 to 1.2 μV by changing the magnetization axis (**M**) from [100] to [110]. ANE has been experimentally explored for both in-plane and out-of-plane thermal gradients ($\nabla T \| \ x/z$) [90, 107, 138, 139, 108, 176]. However, the functional devices with out-of-plane thermal gradient ∇T_z are more beneficial in the context of practical application for heat harvesting [139, 138, 108].

7.2 Weyl points origin of giant ANC

Recently, it has been discovered that the presence of Weyl points in close proximity to the Fermi energy leads to AHC peaks, resulting in a large ANC [147, 186, 197]. This relationship between a large AHC/ANC and Weyl points near the Fermi-energy has been reported in several recent studies [101, 141, 140]. For instance, in the Weyl semimetal $Co_3Sn_2S_2$, a large AHC peak with a maximum AHC value of 1100 S/cm exists at the Fermi-energy [101], resulting in a large ANC of 10.0 A/mK [198]. This peak is attributed to the presence of Weyl points located only 60 meV above the Fermi-energy [101]. Inspired by these studies, we conducted a comprehensive investigation of the electronic structure of Co_3PtN, which exhibits a giant ANC of 6.31 A/mK at the Fermi-energy. As depicted in Figure 7.2, an AHC peak (1440 S/cm) is observed at 54 meV above the Fermi-energy, accompanied by two linear band crossings around $\sim$20 meV above the Fermi-energy along the R-M Brillouin zone path in the band structure.

7.2.1 Procedure to calculate Weyl points

In order to find the Weyl points contribution to the total AHC:

1. We searched for the Weyl points near the Fermi energy, within the energy range

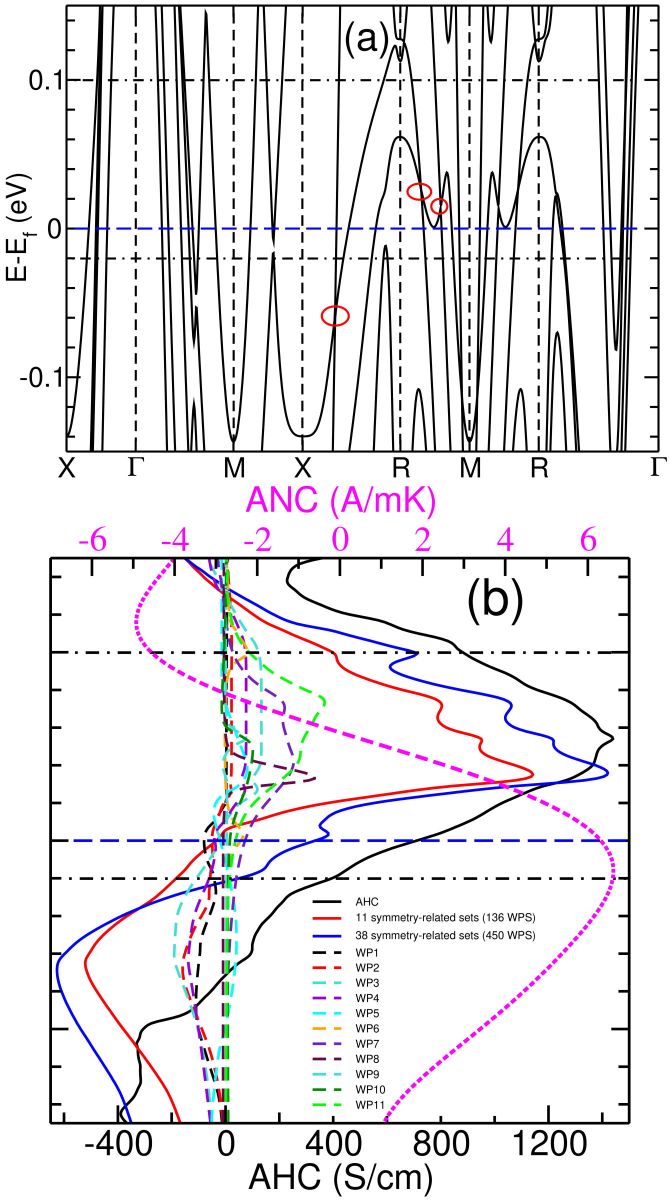

Figure 7.2: Co$_3$PtN with magnetization direction [001]. The horizontal black dot lines at -0.02 eV and 1.0 eV indicate the window range within which the Weyl points are being searched. (a) band structure is shown,with red circles marking the band crossing between R-M and X-R. (b) The AHC is shown along with the analysis of the Weyl points (WP). The AHC in red and blue are obtained by summing the contributions from 136 Weyl points (WP1-WP11), and the 450 Weyl points(38 set of symmetry-related Weyl points. The ANC is calculated at 300 K (magenta).

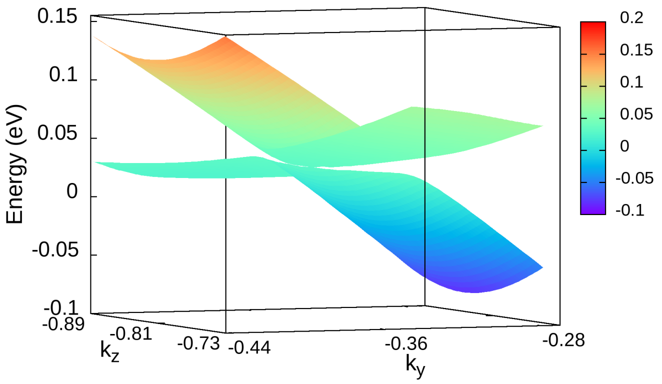

Figure 7.3: The characterization of the Weyl points in the (k_y,k_z) plane for the Weyl point located at (0.499, -0.218, -0.492), along with the corresponding energy dispersion plot demonstrating the bands degeneracies at the Weyl nodes.

of -0.02 eV to 0.1 eV (Figure 7.2(a)), which incorporates the AHC peak located 54 meV above the Fermi energy (Figure 7.2(b)).

2. The corresponding band indices were identified within the specified energy window, resulting in six bands. The calculations were performed using the Wanniertools code to find the Weyl points for all six bands.

3. We identified 450 Weyl points, which can be further classified into 38 sets of symmetry-associated Weyl points, following 16 symmetry operations related to the magnetic space group $P4/mm'm'$ (123.345).

4. For the symmetry-associated Weyl point WP8 (Figure 7.2(b)), the three-dimensional (3D) band structure is shown in Figure 7.3. It consists of 16 symmetry-associated Weyl points located at $(0.499, -0.218, -0.492)$ and equivalent k-points, with an energy of 25 meV above the Fermi energy.

5. For all the 450 Weyl points, the AHC is evaluated by considering a small cube centering at spatial Weyl point position and with the acme of 0.08 (in units of $2\pi/a$).

6. We distinguished 11 sets of symmetry-associated Weyl points (136 Weyl points) that contribute significantly to the total AHC, reproducing the AHC peak above the Fermi-energy (Figure 7.2(b)). However, the sum of AHC from the 38 sets of symmetry-related Weyl points is larger than the total AHC, demonstrating the

significant contribution of Weyl points (Figure 7.2(b)). Therefore, we posit that the giant ANC in Co_3PtN originates from the existence of Weyl points in close proximity to the Fermi-energy.

It is evident that not all Weyl points contribute significantly to the total AHC, as shown in Figure 7.2(b). Specifically, out of 450 Weyl points, only 136 of them contribute significantly to the total AHC. Due to the presence of numerous Weyl points, there is a possibility of overlap in regions during the calculation, which affects the evaluation of Weyl points' contribution to the total AHC. The presence of Weyl points does not necessarily result in a singular AHC. Unlike $Co_3Sn_2S_2$, there exists only six Weyl point, situated at 60 meV above the Fermi-energy, and one pair of Weyl node acts as a monopole sink and source of Berry curvature [101]. However, there are numerous such Weyl points in case of Co_3PtN, which is a common characteristic of FM compounds [53]. Therefore, given that there are so many Weyl nodes in FM compounds, it is challenging to identify dominant contributions from a few singular points. This implies that a large ANC can be further tailored by shifting the Fermi-energy via proper doping for the peak AHC close to the Fermi-energy.

7.3 ANC in non-collinear Γ_{4g} and comparison with FM

The APs with non-collinear Γ_{4g} in cubic structures exhibit ANC values larger than 2.0 A/mK for 4 out of 8 AP compounds. For example, Cr_3IrN and Cr_3PtN have ANC values as large as -3.24 and -4.02 A/mK, respectively (Figure 6.4). In a previous study, Zhou *et al.* [212] found an ANC of 1.80 A/mK at 200 K, while our calculated ANC value is 1.99 at 300 K. However, recent experimental studies on Mn_3NiN thin films have measured an ANC of only 0.00348 Am/K, which contradicts the theoretical observation for Mn_3NiN [8]. According to Beckert et al. [8], the observed inconsistency between the experimental and theoretical ANE values can likely be attributed to the specific position of the Fermi level in the samples. In fact, the measurement of ANC should serve as a more sensitive probe for the Berry curvature in the vicinity of the Fermi level (E_f) [201].

The FM compounds frequently have larger ANC compared to non-collinear compounds. The largest ANC of 6.31 A/mK is achieved for FM Co_3PtN, and 13 FM compounds have ANC larger than 2.0 A/mK. However, large ANC is not solely restricted to the FM state (Table 9.11). For instance, Mn_3NiN has ANC of 1.99 A/mK in non-collinear Γ_{4g} magnetic ground state and 0.73 A/mK in the FM state for [110] magnetization axis. Therefore, a large ANC is not guaranteed in the FM state when compared to the ANC of APs with non-collinear magnetic ground states.

8 Summary and Outlook

In summary, we firstly carried out a high-throughput screening of 630 cubic APs and conducted DFT calculations to examine three stability parameters: thermodynamic, mechanical, and dynamical stability. Consequently, we predicted 11 new magnetic APs that fulfilled all three stability criteria. Three out of the 11 predicted compounds were later synthesized in experiments, thereby validating our predictions. Additionally, our calculations confirmed the stabilities of 76 experimentally known APs, with a few discrepancies. We believe that considering all three stability criteria is crucial in the design of new materials.

Secondly, we analyzed the magnetic ground state of the 54 APs, which include 43 experimentally reported compounds and 11 predicted compounds. We considered seven different magnetic configurations for our analysis. As a result, we found that 14 AP compounds stabilized in either Γ_{4g} or Γ_{5g} non-collinear AFM states, and we identified four new non-collinear APs. Non-collinear magnetic configurations had previously only been reported for Mn-based APs. Interestingly, we observed that Cr-based APs, such as Cr_3IrN and Cr_3PtN, stabilized in the non-collinear Γ_{4g} AFM state. In addition, we performed a detailed analysis of the total energy (ΔE_{tot}) difference between the Γ_{5g} and Γ_{4g} states. Our findings revealed that ΔE_{tot} is mainly attributed to strong spin-orbit coupling, which is responsible for the non-collinear AFM structure in APs. Furthermore, as expected, the maximum magnetic anisotropy energy (MAE) of cubic ferromagnetic (FM) APs is less than 10 μeV/atom for 28 out of 35 APs, with Fe_3IrN having the largest MAE of -59.8 μeV/atom.

Third, we focused on the magnetic properties of APs with non-collinear AFM states, driven by strong magnetostructural coupling. Specifically, we examined the negative thermal expansion (NTE) and piezomagnetic effect (PME), which arise from isotropic and anisotropic magnetostructural coupling, respectively. The NTE behavior investigated using $\Delta a/a_0$ between AFM and DLM based PM states provides a better agreement with experimental observations compared to the PM state approximated as a NM state. We propose Cr_3IrN and Cr_3PtN as potential NTE materials with large $\Delta a/a_0$ values. The application of biaxial strain leads to a significant piezomagnetic effect (PME) in non-collinear APs, with the largest net magnetization of 0.646 μB observed for Mn_3CoN. In addition, cubic non-collinear APs undergo phase transition under biaxial strain between $\Gamma_{4g} \leftrightarrow \Gamma_{5g}$.

Fourth, we determined the AHC for non-collinear AFM and FM APs. Symmetry analysis was conducted to explain the reasons for the vanishing or non-vanishing AHC components, which are consistent with our calculations. Generally, FM APs exhibit comparably larger AHCs than non-collinear AFM APs. The largest AHCs obtained in FM and non-collinear APs are 1128 S/cm (Co_3LiN) and 722 S/cm (Cr_3IrN), respectively. For non-collinear APs, the calculated AHC under biaxial strain is enhanced with no strong correlation between the net magnetization and AHC. A thorough analysis of Weyl points indicates that the magnitude of AHC can be correlated to the fine-tuning of energies for the Weyl points, illustrated for Mn_3PdN.

Finally, we investigated the ANC using the generalized Mott formula. Similar to AHC, FM APs have larger ANC than non-collinear AFM APs. The largest ANC values obtained in FM and non-collinear APs are 6.31 A/mK (Co_3PtN) and -4.02 A/mK (Cr_3PtN), respectively. It was observed that the large ANC in Co_3PtN is due to the existence of Weyl points in close proximity to the Fermi level. Furthermore, we observed that the magnitude and sign of AHC/ANC can be changed by adjusting the magnetization axis.

This work presents a comprehensive analysis of magnetic APs, including the prediction of new AP materials and the calculations of various magnetic properties. We propose potential materials such as Cr-based APs for further analysis and hope that our findings will inspire experimental efforts to confirm our observations.

9 Appendices

9.1 Computational details

9.1.1 Chapter 3

DFT calculations were performed using the Projector Augmented Wave PAW method implemented in the VASP package [93, 92]. The energy cutoff for plane wave basis was set at 500 eV and 14 × 14 × 14 k-points were used for the Brillouin zone integrations using Monkhorst-Pack scheme. To ensure consistency, the same calculation setup was used for all competing phases. All stability calculations were performed considering the ferromagnetic state without spin-orbit coupling. The exchange-correlation functional was approximated with the generalized gradient approximation (GGA) parameterized by Perdew-Burke-Ernzerhof (PBE) [130]. The partial occupancies of the electronic states were smeared by using the order one Methfessel-Paxton smearing width of 0.06 eV. The total energy convergence criterion was fixed at 10^{-07} eV. The lattice dynamics calculations were performed within the harmonic approximation based on the frozen phonon approach using VASP and Phonopy [172]. The forces on each atom were determined using the Hellmann-Feynman theorem by explicitly displacing the atoms of 2 × 2 × 2 supercells and calculating the force constant matrix [29]. The convergence of the phonon spectra was tested by comparison with larger supercells (not shown) and density function perturbation theory (DFPT) methods. We also tested our phonon calculations by comparisons with the Quantum Espresso code [52].

9.1.2 Chapter 4 and 5

The magnetic ground state analysis was done using the VASP code and a similar calculation as in Chapter 3 was used, with a few parameter values changed, such as using a k-point mesh of 13× 13 × 13. The MAE of FM cubic APs were calculated using an energy cutoff of 600 eV and a k-mesh of 17× 17 × 17.

9.1.3 Chapter 6 and 7

The DFT calculations were performed using the same parameters as in chapter 4 and 5. We used the Wannier90 code to obtain the maximally localized Wannier functions and get the tight-binding model Hamiltonian [110]. In total, 80 maximally localized Wannier functions were constructed for every AP system by projecting the s, p, and d orbitals of M and X atoms and the s and p orbitals for the N or C atom. The AHC was computed using the WannierTools code [192]. A uniform k-mesh of 401×401×401 was used for the Berry curvature integration [195]. The AHC was determined in conformity with the following equation:

$$\sigma_{\alpha\beta} = -\frac{e^2}{\hbar} \int \frac{d\mathbf{k}}{(2\pi)^3} \sum_n f\left[\epsilon\left(\mathbf{k}\right) - \mu\right] \Omega_{n,\alpha\beta}\left(\mathbf{k}\right) \tag{9.1}$$

$$\Omega_{n,\alpha\beta}\left(\mathbf{k}\right) = -2\mathrm{Im} \sum_{m \neq n} \frac{\langle\psi_{\mathbf{k}n}|v_\alpha|\psi_{\mathbf{k}m}\rangle\langle\psi_{\mathbf{k}m}|v_\beta|\psi_{\mathbf{k}n}\rangle}{\left[\epsilon_m\left(\mathbf{k}\right) - \epsilon_n\left(\mathbf{k}\right)\right]^2} \tag{9.2}$$

where e is elementary charge, μ is the chemical potential, $\psi_{n/m}$ denotes the Bloch wave function with energy eigenvalue $\epsilon_{n/m}$, $v_{\alpha/\beta}$ is the velocity operator along Cartesian α/β direction, and $f[\epsilon\left(\mathbf{k}\right) - \mu]$ is the Fermi-Dirac distribution function. Here, $\{\alpha,\beta\}$ = {x,y,z} denotes the Cartesian coordinates. The ANC was computed using an in-house developed python code. The validation of code was done by reproducing the ANC of Mn_3NiN of Zhou *et al.* [212] (Figure 9.6). The ANC was determined using the following equation:

$$\alpha_{\alpha\beta} = -\frac{1}{e} \int d\epsilon \frac{\partial f}{\partial \mu} \sigma_{\alpha\beta}\left(\epsilon\right) \frac{\epsilon - \mu}{T}, \tag{9.3}$$

where T is the temperature, μ the Fermi level, and ϵ is the point of the energy grid.

9.2 Figures

9.2.1 Formation energies (E_f) of APs

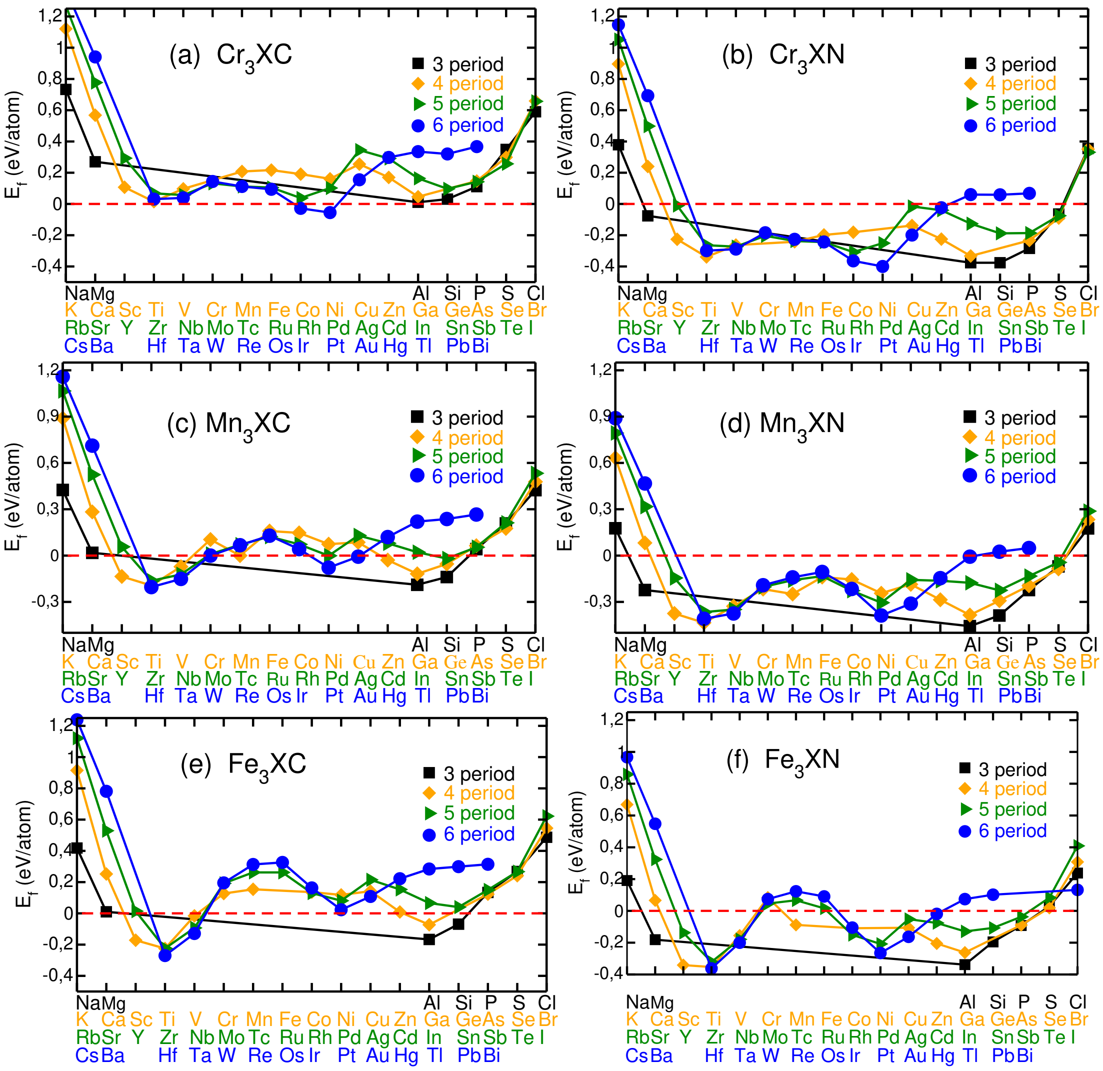

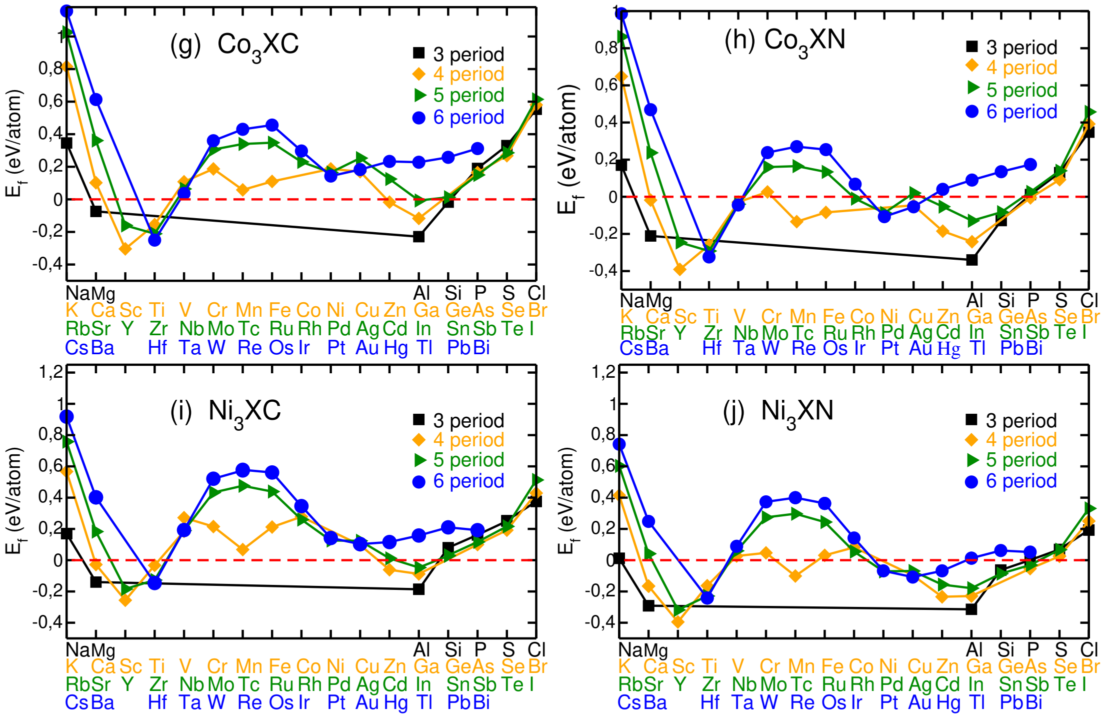

Figure 9.0: The formation energies of the antiperovskites M_3XZ, where X belongs to the elements present on the x-axis of each plot.

9.2.2 Convex hull distance ($\triangle E_h$) of APs

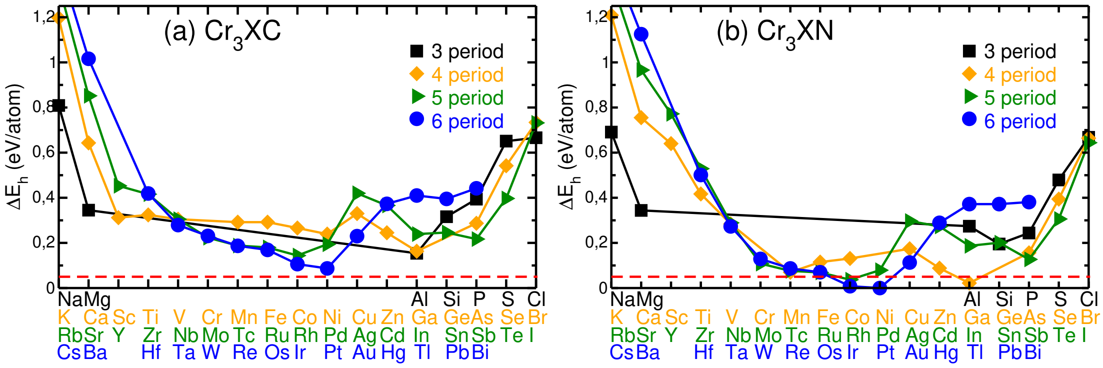

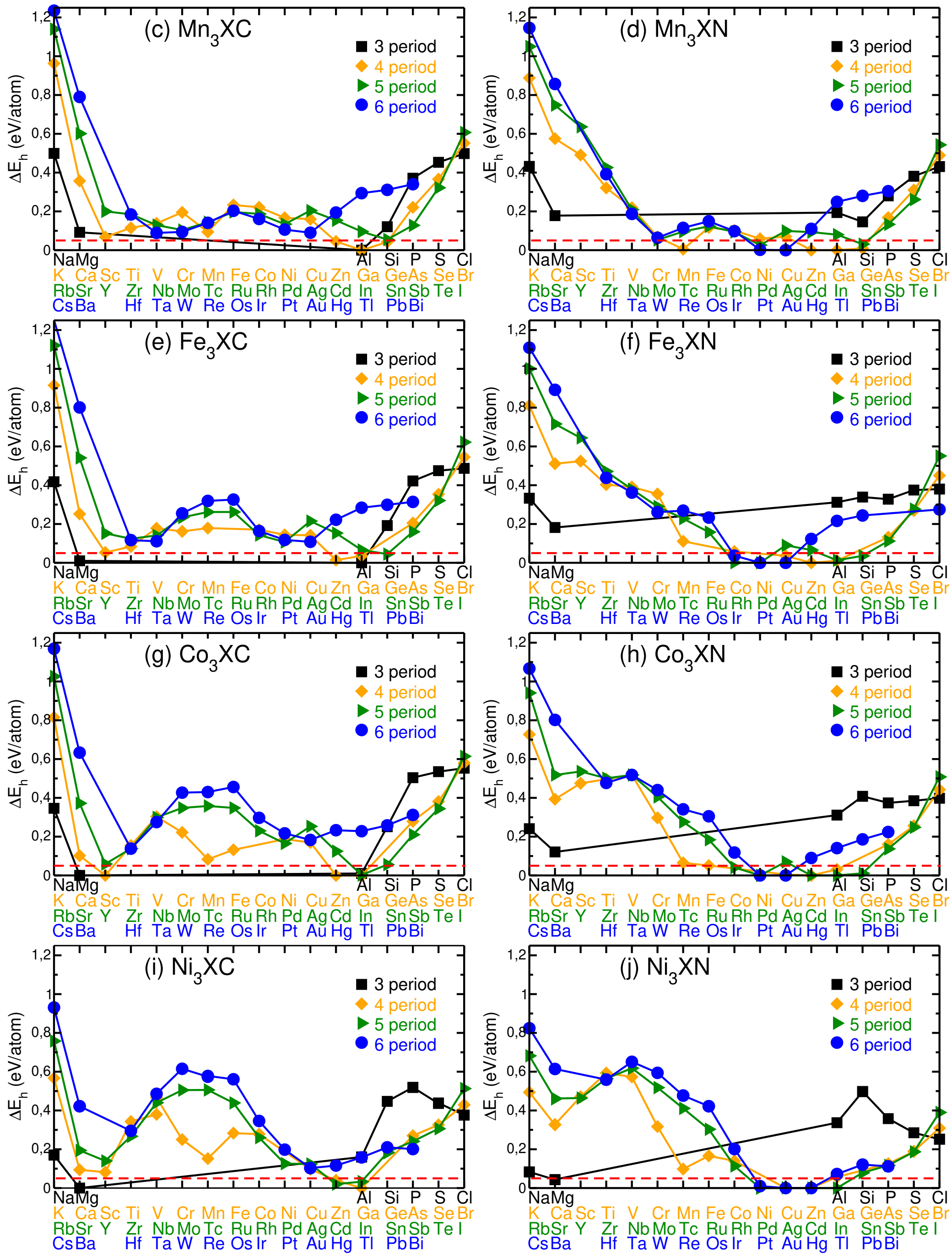

Figure 9.1: The distance to convex hull of the antiperovskites M$_3$XZ, where X belongs to the elements present on the x-axis of each plot.

9.2.3 Validation of PME with previous study on APs

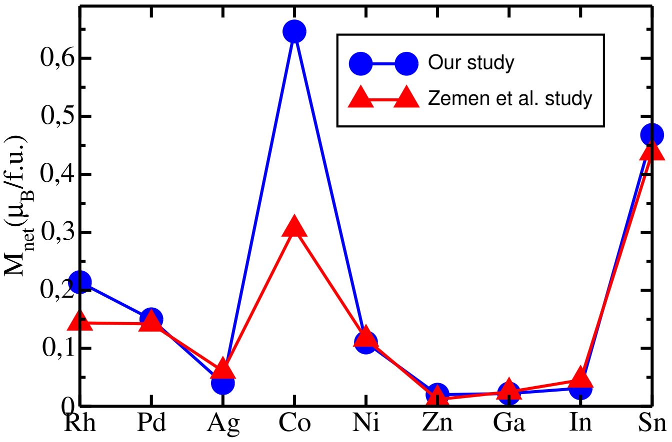

Figure 9.2: Comparison of the net magnetization calculated in our study and Zemen *et al.* study [206] for Mn_3XN APs for an applied tensile strain of 1%, where X represents the elements on the x-axis.

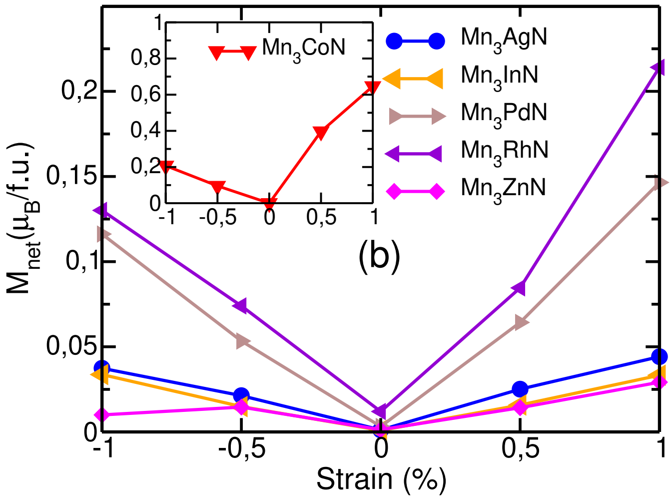

Figure 9.3: The calculated net magnetization for Mn_3XN APs studied by Zemen et al. for 1% tensile strain where X represents the elements on the x-axis.

9.2.4 AHC of non-collinear Cr_3IrN and Mn_3PtN to verify symmetry analysis

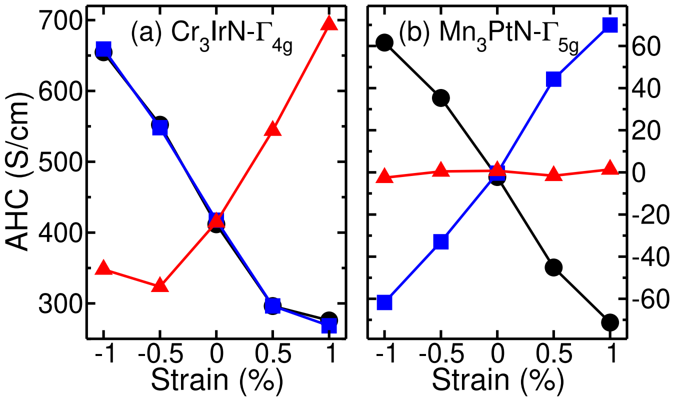

Figure 9.4: The calculated AHC of Mn_3PtN for (a) Γ_{4g} and (b) Γ_{5g} phase. The circle, square, and triangle correspond to the σ_x, σ_y, and σ_z AHC components, respectively.

9.2.5 AHC of FM Fe_3IrN to verify symmetry analysis

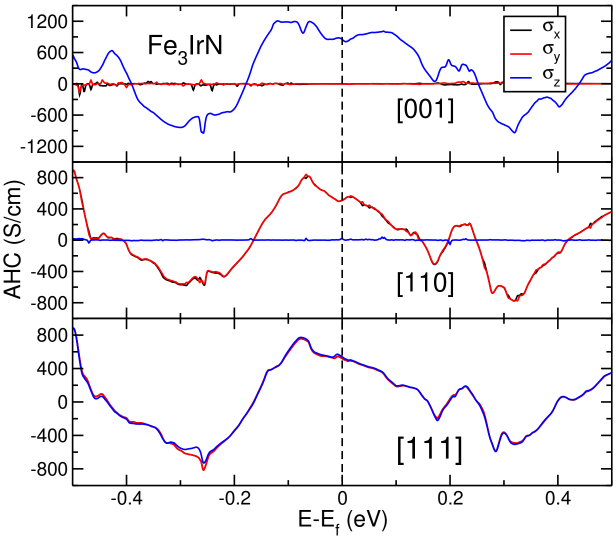

Figure 9.5: The calculated anomalous Hall conductivity of ferromagnetic compound Fe_3IrN for the [001], [110], and [111] magnetization directions.

9.2.6 Validation of ANC of Mn_3NiN with previous study

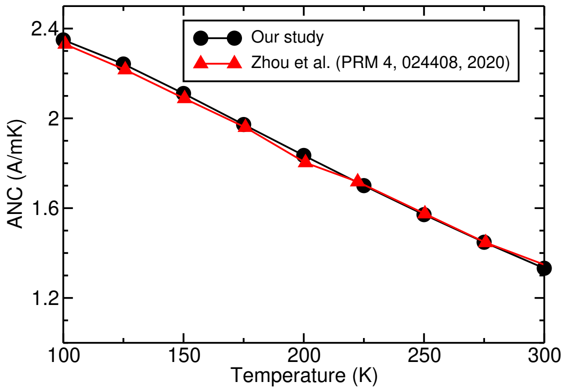

Figure 9.6: Comparison of the calculated ANC for Mn_3NiN with Γ_{4g} magnetic ground state from our study and Zhou *et al.* [212].

9.2.7 AHC of FM APs as a function of chemical potential

Figure 9.7: The AHC of AP compounds M_3XZ for the [001], [110], and [111] magnetization directions.

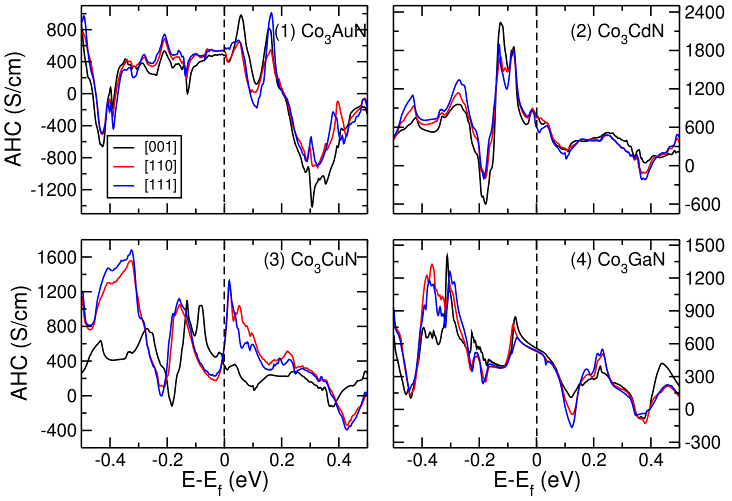

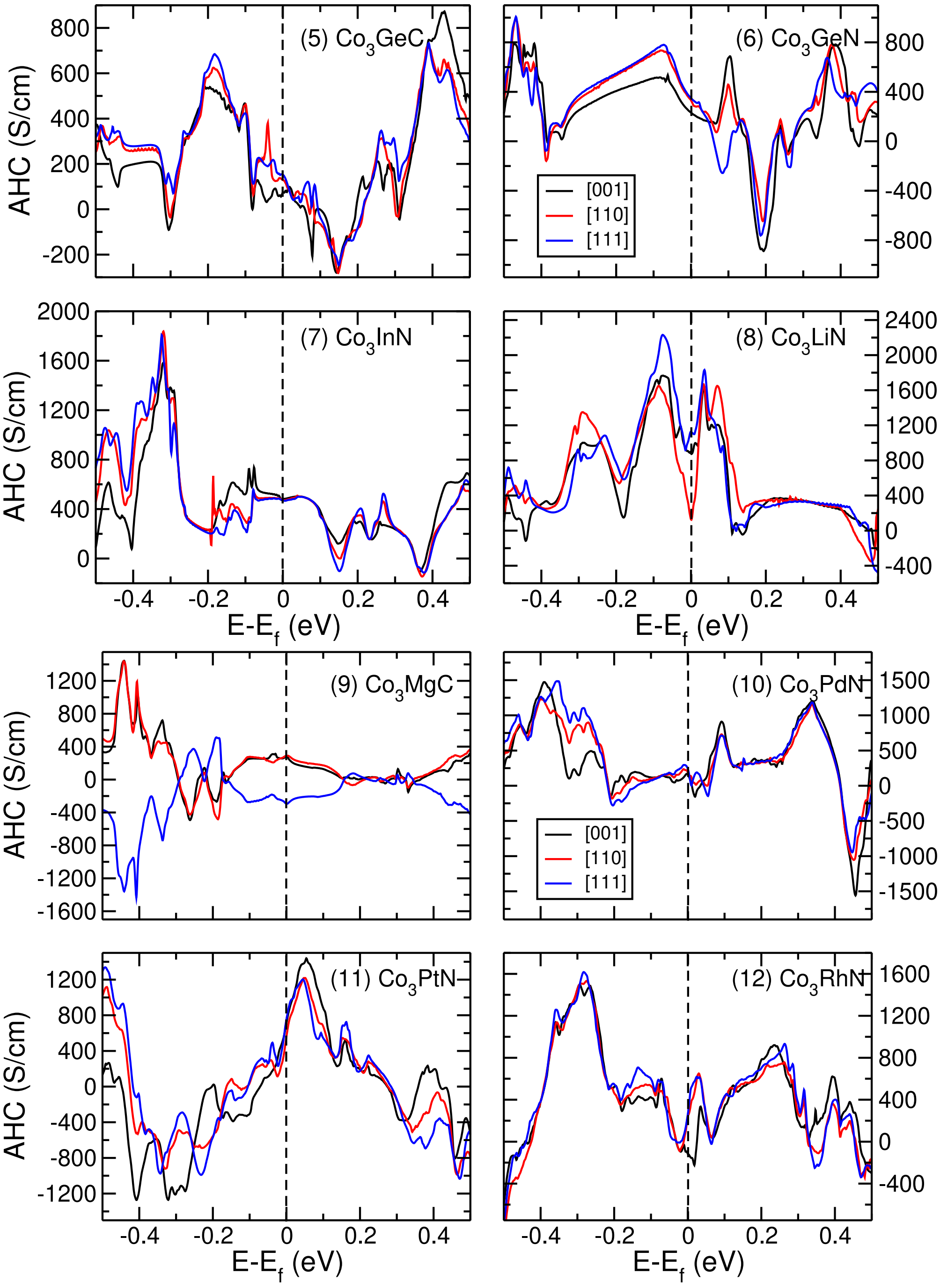

(5) Co$_3$GeC
(6) Co$_3$GeN
(7) Co$_3$InN
(8) Co$_3$LiN
(9) Co$_3$MgC
(10) Co$_3$PdN
(11) Co$_3$PtN
(12) Co$_3$RhN
AHC (S/cm)
E-E$_f$ (eV)
[001]
[110]
[111]
800
600
400
200
0
-200
-400
-800
2000
1600
1200
2400
1500
1000
500
-500
-1000
-1500
-1200
-1600
-0.4
-0.2
0.2
0.4

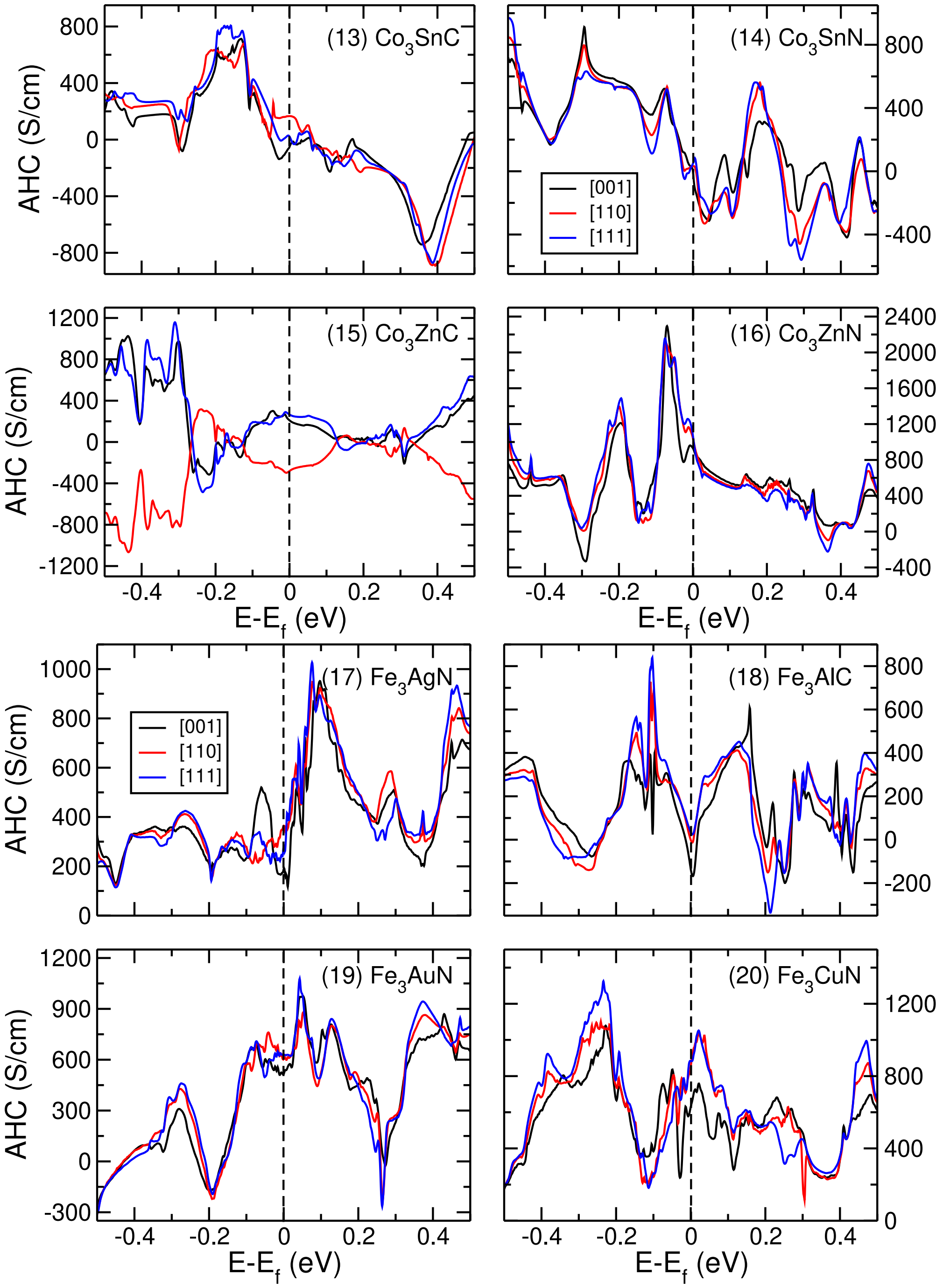
(13) Co_3SnC
(14) Co_3SnN
(15) Co_3ZnC
(16) Co_3ZnN
(17) Fe_3AgN
(18) Fe_3AlC
(19) Fe_3AuN
(20) Fe_3CuN
[001]
[110]
[111]
AHC (S/cm)
$E-E_f$ (eV)
-0.4
-0.2
0
0.2
0.4
800
400
0
-400
-800
1200
-1200
2400
2000
1600
1000
600
200
-200
900
300
-300

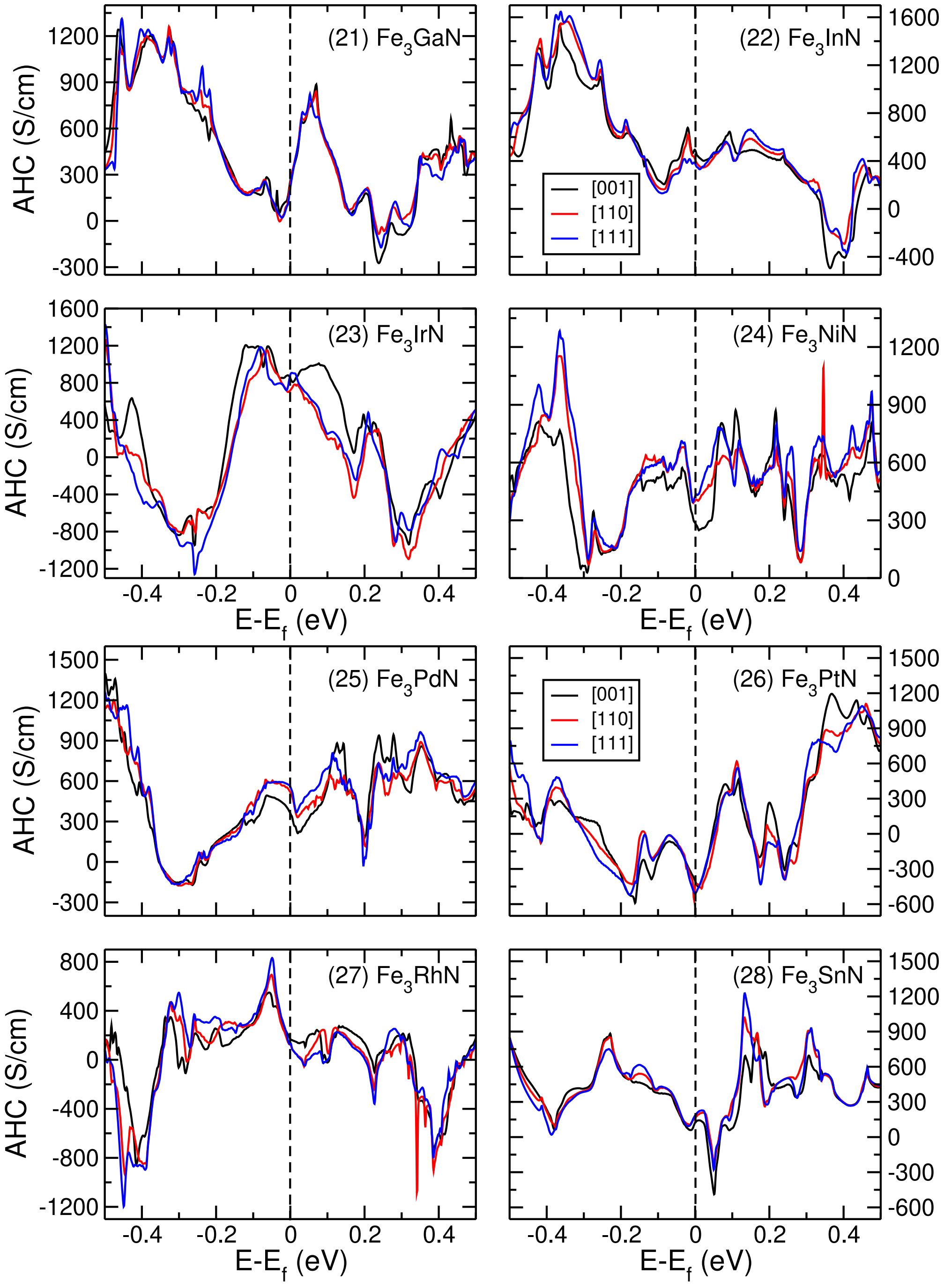
(21) Fe$_3$GaN
(22) Fe$_3$InN
(23) Fe$_3$IrN
(24) Fe$_3$NiN
(25) Fe$_3$PdN
(26) Fe$_3$PtN
(27) Fe$_3$RhN
(28) Fe$_3$SnN
[001]
[110]
[111]
AHC (S/cm)
E-E$_f$ (eV)
-0.4
-0.2
0
0.2
0.4
-1200
-800
-400
0
400
800
1200
1600
-300
300
600
900
1500
-600

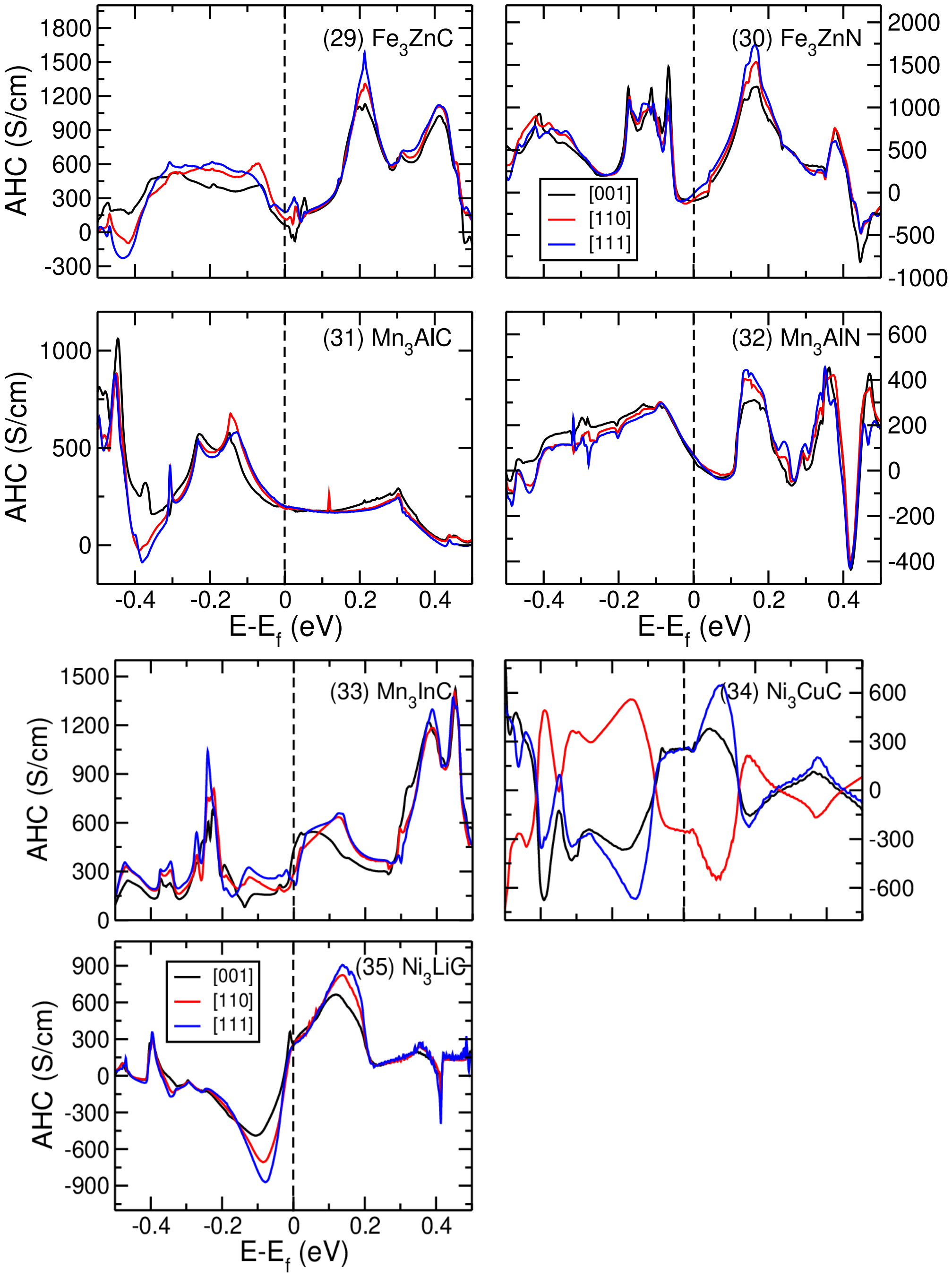
(29) Fe$_3$ZnC
(30) Fe$_3$ZnN
(31) Mn$_3$AlC
(32) Mn$_3$AlN
(33) Mn$_3$InC
(34) Ni$_3$CuC
(35) Ni$_3$LiC
AHC (S/cm)
E-E$_f$ (eV)
[001]
[110]
[111]
1800
1500
1200
900
600
300
0
-300
2000
1500
1000
500
0
-500
-1000
1000
500
0
600
400
200
0
-200
-400
-0.4
-0.2
0
0.2
0.4
1500
1200
900
600
300
0
600
300
0
-300
-600
900
600
300
0
-300
-600
-900

Figure 9.8: The calculated AHC of APs (M3XN) in the $\Gamma5g$ and Γ_{4g} magnetic ground states are shown. The circle, square, and triangle correspond to the σ_x, σ_y, and σ_z AHC components, respectively. For the Γ_{5g} cubic phase, the σ_x, σ_y, and σ_z components are not exactly zero due to numerical error. The AHC calculations of Mn_3AuN did not converge for the compressive strain.

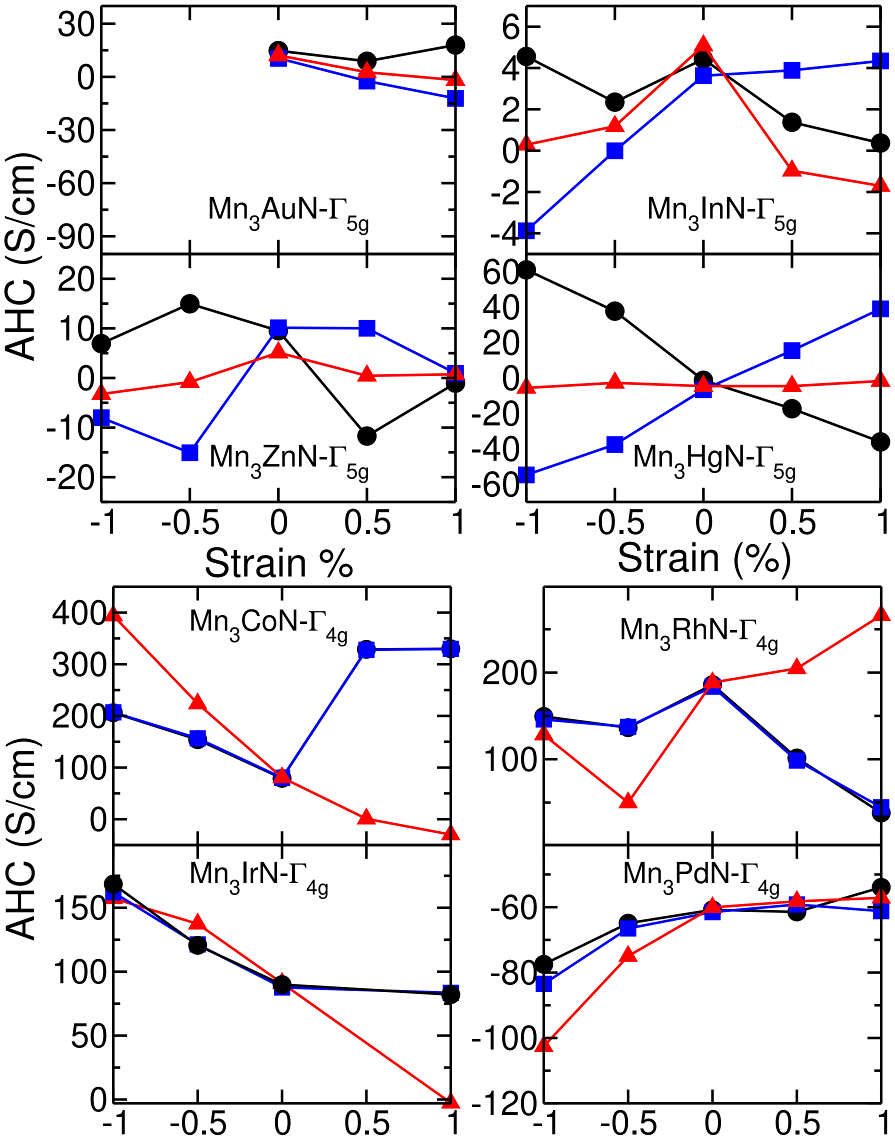

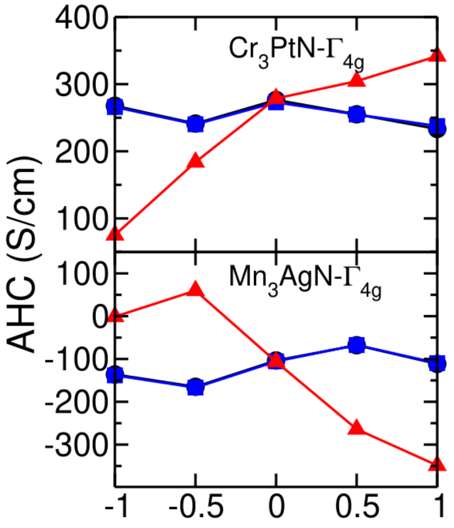

9.2.9 ANC of FM APs as a function of chemical potential

Figure 9.9: The ANC of AP compounds M_3XZ for the [001], [110], and [111] magnetization directions. The ANC is calculated at 300 K.

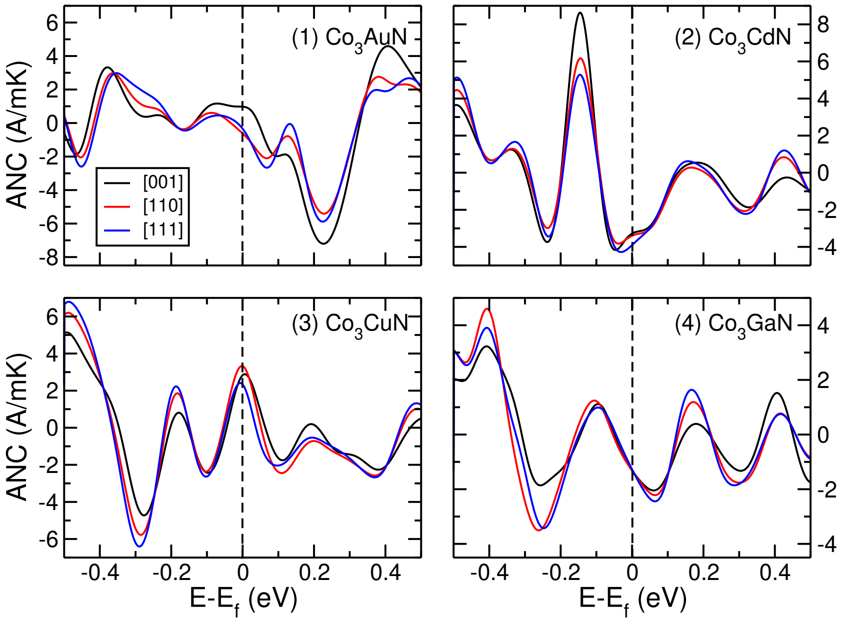

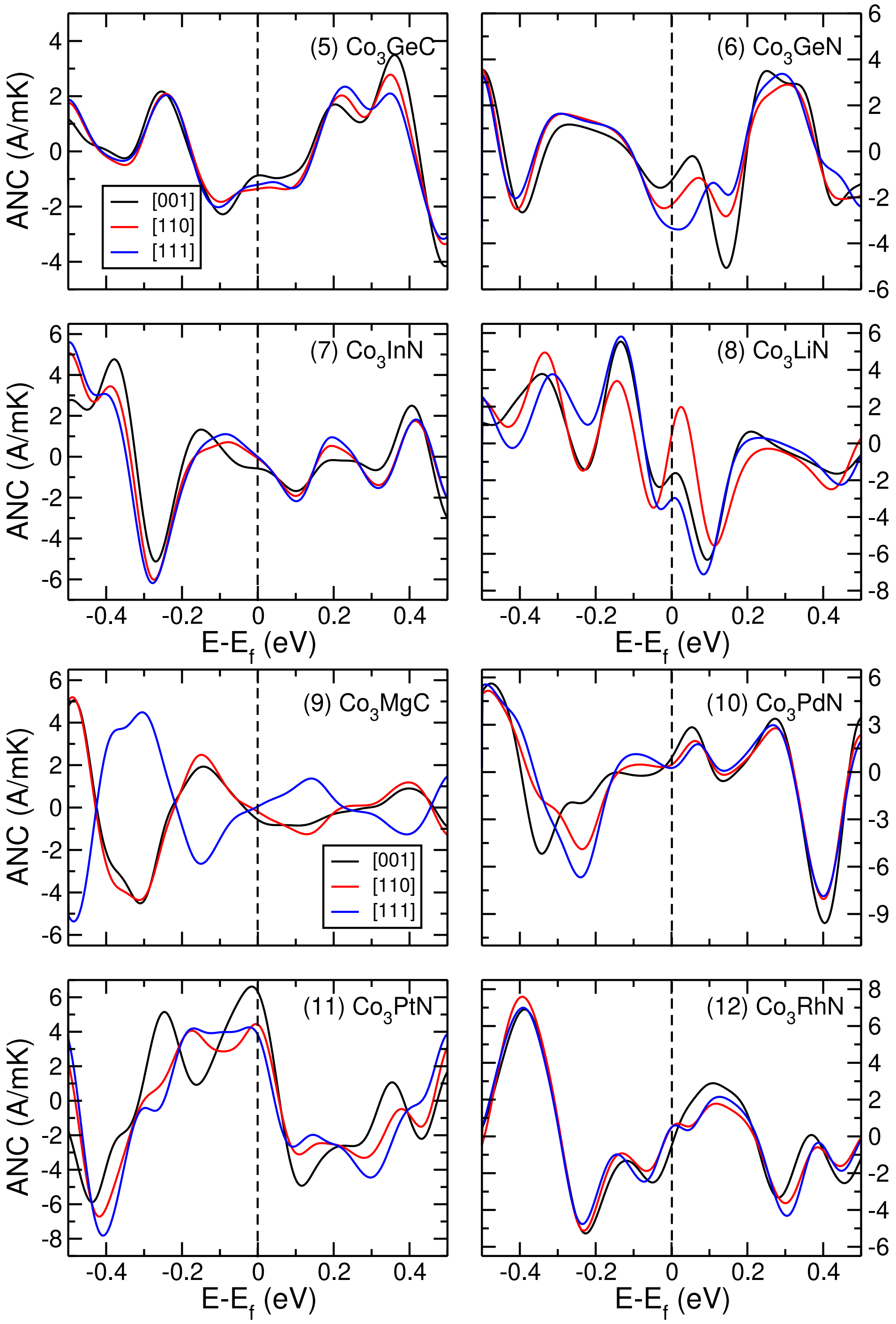
(5) Co_3GeC
(6) Co_3GeN
(7) Co_3InN
(8) Co_3LiN
(9) Co_3MgC
(10) Co_3PdN
(11) Co_3PtN
(12) Co_3RhN
[001]
[110]
[111]
ANC (A/mK)
E-E_f (eV)
-0.4
-0.2
0
0.2
0.4

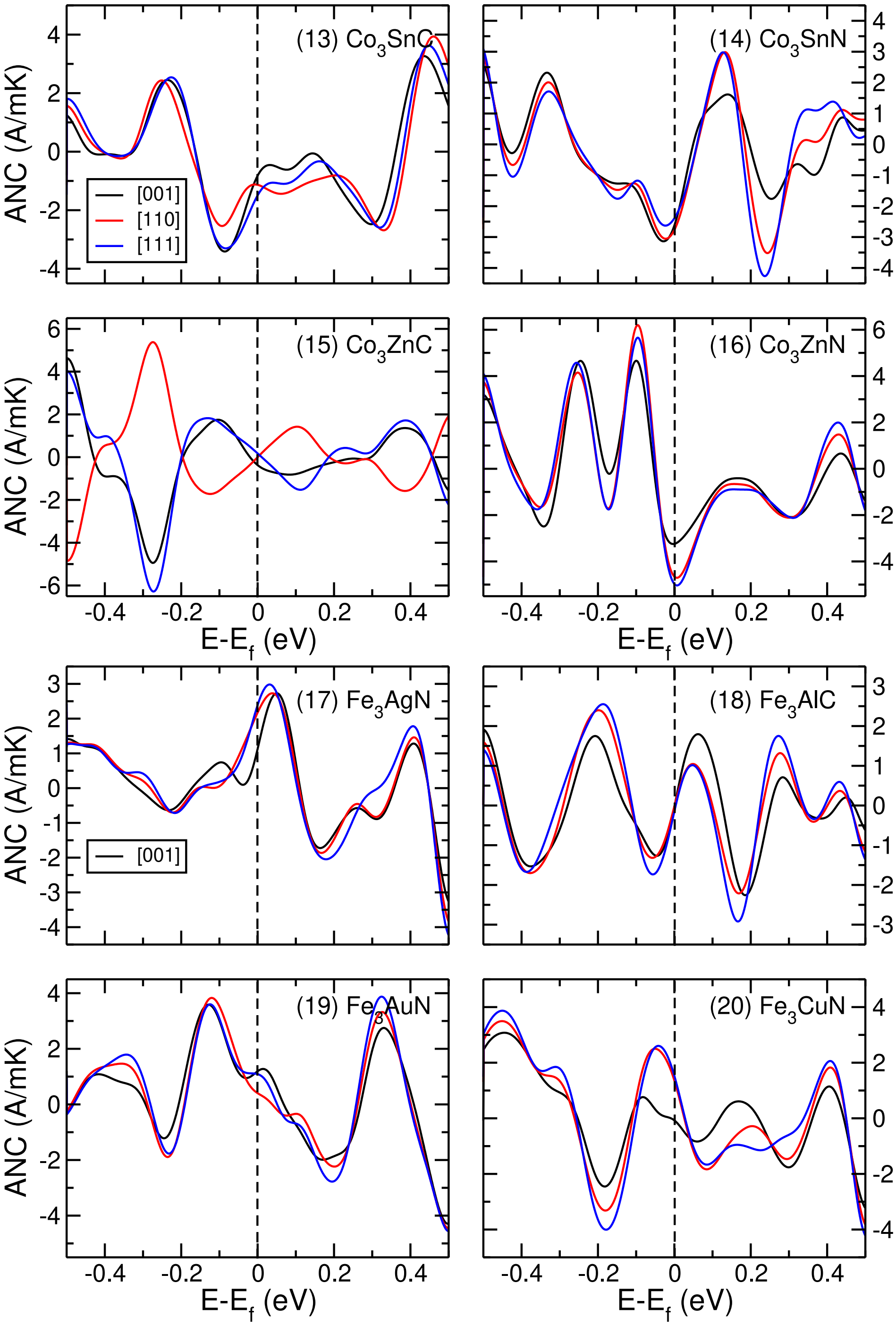
(13) Co_3SnC
(14) Co_3SnN
(15) Co_3ZnC
(16) Co_3ZnN
(17) Fe_3AgN
(18) Fe_3AlC
(19) Fe_3AuN
(20) Fe_3CuN
[001]
[110]
[111]
ANC (A/mK)
$E-E_f$ (eV)
-0.4
-0.2
0
0.2
0.4

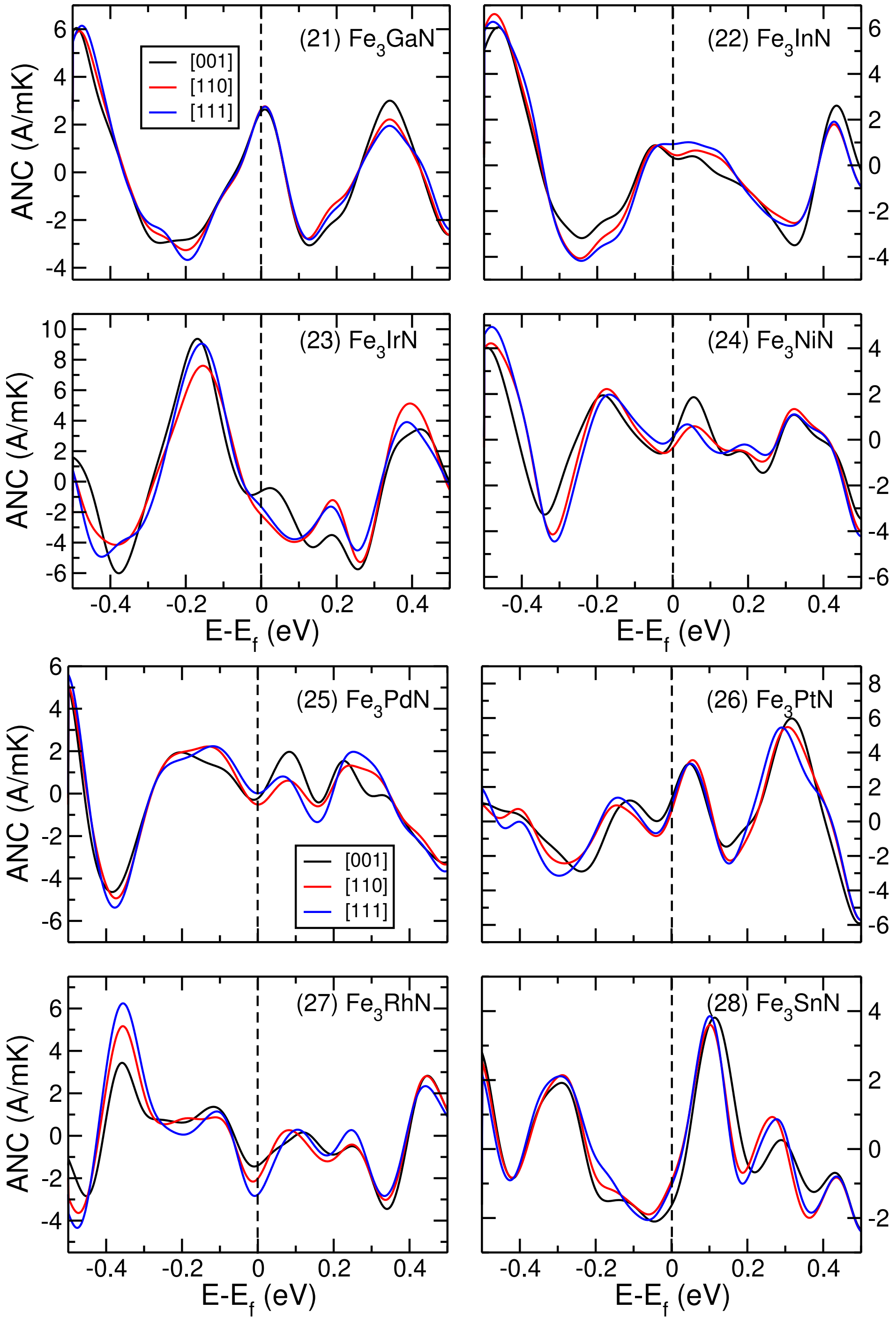
(21) Fe_3GaN
(22) Fe_3InN
(23) Fe_3IrN
(24) Fe_3NiN
(25) Fe_3PdN
(26) Fe_3PtN
(27) Fe_3RhN
(28) Fe_3SnN
[001]
[110]
[111]
ANC (A/mK)
E-E_f (eV)
-0.4
-0.2
0
0.2
0.4

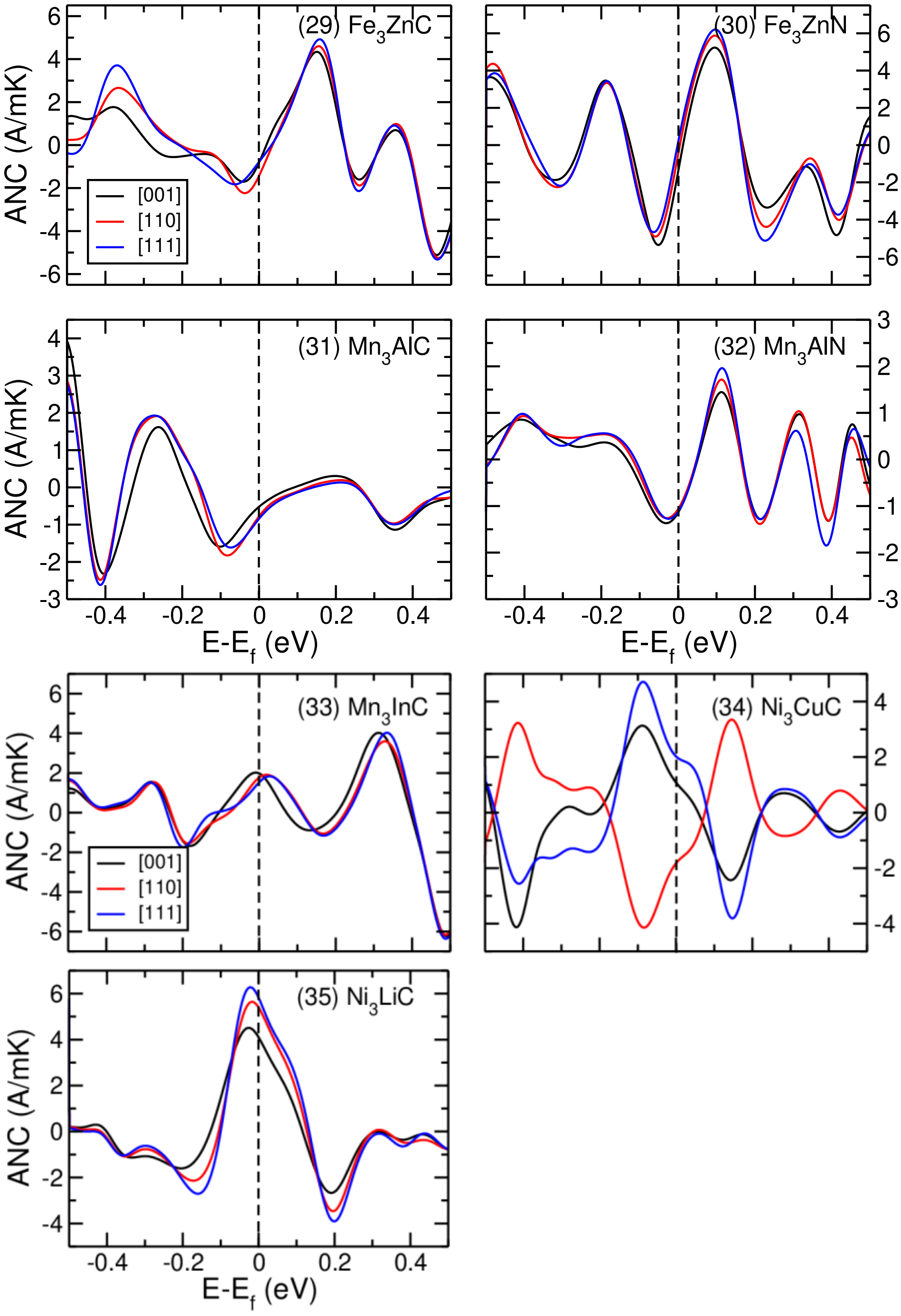
(29) Fe$_3$ZnC
(30) Fe$_3$ZnN
(31) Mn$_3$AlC
(32) Mn$_3$AlN
(33) Mn$_3$InC
(34) Ni$_3$CuC
(35) Ni$_3$LiC
[001]
[110]
[111]
ANC (A/mK)
E-E$_f$ (eV)
-0.4
-0.2
0
0.2
0.4
6
4
2
0
-2
-4
-6
3
1
-1
-3

9.3 Tables

9.3.1 Experimental APs lattice parameters and thermodynamical stability

Table 9.1: The experimentally reported **stoichiometric** cubic antiperovskites are listed, summarizing the calculated and the experimental lattice constants, calculated magnetic moment (μ_B/f.u.), calculated formation energy (E_f in eV/atom), and calculated convex hull distance (ΔE_h in eV/atom).

Compounds	Calculated lattice constant (Å)	Experimental lattice constant (Å)	Magnetic moment (μ_B/f.u.)	E_f (eV/atom)	ΔE_h (eV/atom)
Co_3CdN	3.84	3.841 [63]	3.24	−0.050	0.000
Co_3CuN	3.73	3.75 [72]	4.07	−0.042	0.005
Co_3GeN	3.77	3.629 [215]	3.42	−0.079	0.043
Co_3InN	3.84	3.854 [27]	2.72	−0.123	0.022
Co_3MgC	3.77	3.81 [74]	1.08	−0.072	0.000
Co_3ZnC	3.73	3.72 [73]	1.07	−0.019	0.000
Cr_3GaN	3.83	3.879 [96]	NM	−0.329	0.020
Cr_3IrN	3.81	3.843 [116]	0.42	−0.365	0.007
Cr_3PdN	3.83	3.889 [116]	NM	−0.253	0.081
Cr_3PtN	3.84	3.879 [116]	1.46	−0.400	0.000
Cr_3RhN	3.81	3.854 [116]	NM	−0.310	0.036
Cr_3SnN	3.94	3.974 [116]	0.25	−0.189	0.123
Fe_3AlC	3.75	3.79 [131]	3.10	−0.165	0.000
Fe_3AuN	3.89	3.841 [35]	7.50	−0.161	0.000
Fe_3GaN	3.79	3.797 [67]	5.21	−0.255	0.016
Fe_3InN	3.89	3.867 [94]	5.50	−0.129	0.012
Fe_3NiN	3.78	3.79 [190]	8.01	−0.139	0.025
Fe_3PdN	3.86	3.866 [157]	8.25	−0.208	0.000
Fe_3PtN	3.86	3.857 [190]	8.19	−0.263	0.000
Fe_3RhN	3.84	3.833 [68]	8.77	−0.150	0.000
Fe_3SnC	3.83	3.85 [158]	NM	−0.238	0.049
Fe_3SnN	3.89	3.837 [210]	5.09	−0.104	0.037
Fe_3ZnC	3.77	3.80 [158]	4.10	0.010	0.016
Fe_3ZnN	3.77	3.800 [67]	4.76	−0.204	0.000
Fe_4N	3.79	3.790 [79]	9.92	−0.121	0.020
Mn_3AgN	4.00	4.020 [40]	9.90	−0.158	0.096
Mn_3AlN	3.77	3.854 [95]	2.95	−0.454	0.195
Mn_3AuN	4.00	4.024 [117]	10.05	−0.312	0.000
Mn_3CuN	3.83	3.904 [169]	7.59	−0.186	0.068
Continued	on next	page			

Compounds	Calculated lattice constant (Å)	Experimental lattice constant (Å)	Magnetic moment (μ_B/f.u.)	E_f (eV/atom)	ΔE_h (eV/atom)
Mn_3GaN	3.77	3.898 [24]	3.07	−0.376	0.000
Mn_3InC	3.95	3.993 [88]	6.03	0.020	0.093
Mn_3InN	4.01	4.029 [164]	7.84	−0.184	0.070
Mn_3IrN	3.89	3.913 [116]	8.73	−0.217	0.097
Mn_3NiN	3.84	3.886 [191]	8.83	−0.224	0.059
Mn_3PdN	3.93	3.979 [170]	9.51	−0.307	0.024
Mn_3PtN	3.94	3.972 [116]	9.65	−0.387	0.003
Mn_3RhN	3.89	3.938 [116]	8.78	−0.228	0.092
Mn_3SnC	3.89	3.989 [86]	3.28	−0.014	0.059
Mn_3SnN	3.87	4.060 [116]	3.00	−0.221	0.033
Mn_3ZnC	3.87	3.930 [86]	7.03	−0.030	0.044
Mn_4N	3.75	3.865 [48]	1.21	−0.249	0.005
Ni_3CdC	3.87	3.844 [178]	NM	−0.020	0.023
Ni_3CdN	3.86	3.848 [63]	NM	−0.187	0.000
Ni_3CuN	3.74	3.742 [62]	3.74	−0.094	0.000
Ni_3GaC	3.78	3.6 [159]	NM	−0.110	0.000
Ni_3GeC	3.81	3.58 [159]	NM	−0.111	0.318
Ni_3InN	3.87	3.844 [27]	NM	−0.206	0.000
Ni_3MgC	3.82	3.805 [64]	NM	−0.143	0.000
Ni_3ZnN	3.77	3.756 [177]	NM	−0.266	0.000
Ni_4N	3.73	3.72 [113]	1.57	0.008	0.068

9.3.2 Experimental non-stoichiometric APs lattice parameters and stability

Table 9.2: The experimentally reported **non-stoichiometric** cubic antiperovskites are listed, summarizing the calculated and the experimental lattice constants, magnetic moment (μ_B/f.u.), formation energy (E_f in eV/atom), calculated convex hull distance (ΔE_h in eV/atom), and dynamical stability.

Compounds	Calculated lattice constant (Å)	Experimental lattice constant (Å)	Magnetic moment (μ_B/f.u.)	E_f (eV/ atom)	ΔE_h (eV/ atom)	Dynamically Stable
$Co_3AlC_{0.59}$	3.72	3.69 [74]	NM	−0.359	0.000	Unstable
$Co_3GaC_{0.5}$	3.73	3.65 [159]	NM	−0.236	0.000	Unstable
$Co_3GeC_{0.25}$	3.75	3.6 [73]	1.76	0.055	0.139	Unstable
$Co_3InC_{0.75}$	3.83	3.86 [73]	NM	−0.128	0.099	Stable
$Co_3SnC_{0.7}$	3.84	3.77 [158]	1.68	0.013	0.058	Stable
$Fe_{3.64}Ag_{0.36}N$	3.88	3.800 [35]	7.38	−0.050	0.091	Stable
$Mn_3CoN_{0.74}$	3.82	3.879 [170]	9.26	−0.156	0.099	Unstable
$Mn_3Al_{0.9}C$	3.80	3.871 [89]	3.99	−0.187	0.000	Stable
$Mn_3Ga_{0.97}C$	3.81	3.897 [89]	4.16	−0.110	0.000	Stable
$Mn_3Zn_{0.80}N$	3.79	3.912 [184]	4.24	−0.284	0.000	Stable
$Ni_3AlC_{0.29}$	3.77	3.61	NM	−0.218	0.164	Unstable
$Ni_3InC_{0.50}$	3.87	3.78 [73]	NM	−0.073	0.038	Stable
$Ni_3ZnC_{0.70}$	3.77	3.65 [158]	NM	−0.093	0.042	Stable

9.3.3 Experimental non-cubic APs thermodynamical stability

Table 9.3: The experimentally reported **non-cubic** antiperovskites are listed, summarizing the magnetic moment calculated in cubic *Pm*$\bar{3}$*m*, the formation energy E$_f$ *Pm*$\bar{3}$*m* (non-cubic), and the convex hull distance ΔE$_h$ in *Pm*$\bar{3}$*m* (non-cubic). The last column lists the crystal structure reported in experimental studies.

Compounds	Magnetic moment (μ_B/f.u.)	E$_f$ (eV/atom) Pm$3\bar{m}$ (non-cubic)	ΔE$_h$ (eV/atom) Pm$3\bar{m}$ (non-cubic)	Experimentally crystal structure
Cr_3AsC	1.81	0.147 (-0.109)	0.288 (0.032)	Cmcm [20]
Cr_3AsN	2.58	-0.232 (-0.383)	0.157 (0.006)	I4/mcm [116, 19]
Cr_3GeC	5.58	0.069 (-0.058)	0.173 (0.046)	Cmcm [96]
Cr_3GeN	NM	-0.290 (-0.331)	0.056 (0.015)	P4$2_1$ m [116, 96]
Cr_3PC	NM	0.108 (-0.286)	0.390 (0.00)	Cmcm [20, 214]
Cr_3PN	2.11	-0.283 (-0.558)	0.245 (0.00))	Cmcm [20, 214]
Fe_3GeN	6.13	-0.144 (-0.430)	0.058 (0.00)	I4/mcm [19]
Mn_3AsN	4.51	-0.194	0.167	(I4/mcm) [121, 116]
Mn_3GeC	2.99	-0.054 (-0.132)	0.042 (0.00)	I4/mcm [19]
Mn_3GeN	2.51	-0.292 (-0.314)	0.009 (0.00)	I4/mcm [116, 19]
Mn_3SbN	4.48	-0.132	0.133	P4/mmm [163]
Ni_3FeN	4.16	0.032	0.166	Thin films [166]

9.3.4 Novel APs lattice constant and thermodynamical stability

Table 9.4: The list of novel antiperovskites that do not meet the criterion of dynamical stability but fulfill the criteria of thermodynamical and mechanical stability. Tabulated the calculated lattice constants, magnetic moments (μ_B/f.u.), formation energy (E$_f$ in eV/atom), and convex hull energy (ΔE$_h$ in eV/atom). The calculations were performed considering a cubic structure (Pm$\bar{3}$m) in a ferromagnetic state.

Compounds	Lattice Constant (Å)	Magnetic moment (μ_B/f.u.)	E$_f$ (eV/atom)	ΔE$_h$ (eV/atom)
Co_3NiN	3.72	5.1	-0.038	0.014
Co_4 N	3.72	6.3	-0.004	0.043
Fe_3GaC	3.76	3.16	-0.063	0.044
Fe_3ScC	3.85	3.0	-0.162	0.022
Ni_3AgN	3.83	0.8	-0.067	0.000
Ni_3AuN	3.84	0.7	-0.106	0.000
Ni_3HgN	3.88	0.0	-0.065	0.000
Ni_3LiN	3.75	0.9	-0.235	0.007
Ni_3MgN	3.82	0.0	-0.291	0.044
Ni_3PdN	3.80	1.3	-0.074	0.000
Ni_3PtN	3.80	0.4	-0.067	0.011

9.3.5 MAE and Curie temperature of FM APs

Table 9.5: The MAE of the FM APs calculated using equation 4.3 and the list of Curie temperature (T_c) for which T_c measured experimentally for known APs.

		MAE (μeV/atom)			
S.No.	M_3XZ	[001-111]	[001-110]	[110-111]	T_c (K)
(1)	Co_3AuN	-4.4	-4.2	-0.2	
(2)	Co_3CdN	-0.2	0.8	-1.0	
(3)	Co_3CuN	6.6	-0.8	7.4	650.0 [72]
(4)	Co_3GaN	-0.8	-1.4	0.6	
(5)	Co_3GeC	-8.0	-11.4	3.4	
(6)	Co_3GeN	-3.4	-2.8	-0.6	
(7)	Co_3InN	-3.8	-5.0	1.2	
(8)	Co_3LiN	12.0	-42.4	54.4	
(9)	Co_3MgC	-1.2	-1.0	-0.2	
(10)	Co_3PdN	-1.0	-2.6	1.6	
(11)	Co_3PtN	-41.6	-33.0	-8.6	
(12)	Co_3RhN	6.0	4.8	1.2	
(13)	Co_3SnC	1.2	25.2	-24.0	3.6 [180]
(14)	Co_3SnN	3.0	-19.0	22.0	
(15)	Co_3ZnC	-0.8	-0.6	-0.2	
(16)	Co_3ZnN	0.8	4.6	-3.8	
(17)	Fe_3AgN	-3.6	-5.0	1.4	
(18)	Fe_3AlC	1.0	0.6	0.4	100.0 [55]
(19)	Fe_3AuN	-4.2	-1.0	-3.2	
(20)	Fe_3CuN	3.4	6.8	-3.4	
(21)	Fe_3GaN	-1.8	-1.2	0.6	
(22)	Fe_3InN	1.0	0.8	0.2	662.0 [25]
(23)	Fe_3IrN	-59.8	-59.2	-1.6	
(24)	Fe_3NiN	-1.2	0.2	-1.4	
(25)	Fe_3PdN	52.0	0.6	51.4	601.0 [112]
(26)	Fe_3PtN	-3.8	-0.8	-3.0	
(27)	Fe_3RhN	-3.6	-0.4	-3.2	505.0 [69]
(28)	Fe_3SnN	-2.4	-1.6	-0.8	
(29)	Fe_3ZnC	0.4	-1.2	1.6	200.0 [55]
(30)	Fe_3ZnN	-3.6	7.2	3.8	762.0 [50]
(31)	Mn_3AlC	-0.4	1.2	-1.6	287.0 [183]
(32)	Mn_3AlN	-2.8	-0.4	-2.4	818.0 [95]
(33)	Mn_3InC	-8.6	-1.0	-7.6	272.0 [87]
(34)	Ni_3CuC	5.2	4.0	1.2	
(35)	Ni_3LiC	6.2	5.2	1.0	

9.3.6 Total energies of seven different magnetic configurations

Table 9.6: The total energies (eV/f.u.) of AP (M_3XZ) compounds (Cmpds.) are listed for the non-collinear configurations (Γ_{4g} and Γ_5), ferromagnetic (FM), collinear antiferromagnetic-1 (cAFM-1), collinear antiferromagnetic-2 (cAFM-2), collinear AFM (cAFM-3), and M-1 phases. The first 43 compounds are experimentally known and with serial number 44-54 are newly predicted compounds. The blue color indicates the lowest energy state. In the last colum the text in brackets means that the M-1 phase for the given compounds converges to either the cAFM or the FM state.

No.	Cmpds.	Γ_{4g}	Γ_{5g}	FM	cAFM-1	cAFM-2	cAFM-3	M-1
1	Cr_3IrN	-47.7837	-47.7816	-47.6925	-47.6786	-47.6776	-47.7149	-47.7341
2	Cr_3PtN	-47.0719	-47.069	-46.7972	-46.7509	-46.7548	-46.9028	-46.8057
3	Mn_3AgN	-38.726	-38.7259	-38.5672	-38.5978	-38.6714	-38.3731	-38.6833
4	Mn_3AuN	-40.0991	-40.1014	-39.9552	-39.9924	-40.0586	-39.7331	-40.0464
5	Mn_3CoN	-42.9536	-42.9524	-42.6792	-42.7662	-42.6199	-42.5641	-42.7152 (cAFM)
6	Mn_3GaN	-39.7573	-39.7596	-39.6471	-39.5595	-39.5981	-39.6232	-39.5961
7	Mn_3HgN	-36.33	-36.3316	-36.1247	-36.1302	-36.2742	-36.1009	-36.2077
8	Mn_3InN	-38.7633	-38.7651	-38.466	-38.5422	-38.6572	-38.6325	-38.5621
9	Mn_3IrN	-45.9684	-45.9578	-45.2177	-45.7121	-45.6592	-45.6093	-45.7631 (cAFM)
10	Mn_3NiN	-41.7562	-41.7555	-41.4489	-41.4809	-41.4945	-41.3223	-41.5854
11	Mn_3PdN	-42.2359	-42.2356	-41.7667	-42.1710	-41.9722	-41.6828	42.0212
12	Mn_3PtN	-45.465	-45.47	-44.9928	-45.2871	-45.2865	-45.0145	-45.0029
13	Mn_3RhN	-44.1175	-44.1158	-43.4131	-43.8916	-43.8249	-43.7355	-41.0891 (cAFM)
14	Mn_3ZnN	-37.5949	-37.5964	-37.3752	-37.3831	-37.5495	-37.3819	-37.5063
15	Cr_3SnN	-41.4732	-41.4727	-41.3767	-41.4337	-41.4890	-41.5514	-41.4482
16	Mn_3SnN	-40.0801	-40.0799	-39.8572	-40.0477	-39.8170	-40.1037	-39.9304 (cAFM)
17	Co_3CdN	-29.9256	-29.926	-30.0676	-30.0053	-29.9656	-29.9165	-30.0625 (FM)
18	Co_3CuN	-32.7569	-32.758	-32.9805	-32.8922	-32.8564	-32.7960	-32.8049 (cAFM)
19	Co_3GeC	-34.5598	-34.5604	-34.5887	-31.5871	-34.5892	-34.5576	-34.5885 (FM)
20	Co_3GeN	-33.7962	-33.7961	-33.9573	-33.8180	-33.8178	-33.8267	-33.9372 (FM)
21	Co_3InN	-32.127	-32.1264	-32.25	-32.1372	-32.1328	-32.1273	-32.2502 (FM)
22	Co_3MgC	-32.1651	-32.1649	-32.2027	-32.1726	-32.1720	-32.1659	-32.2029 (FM)
23	Co_3SnC	-34.1079	-34.1086	-34.1389	-34.1006	-34.0996	-34.0991	-34.1390 (FM)
24	Co_3ZnC	-31.5084	-31.5118	-31.5458	-31.5174	-31.5183	-31.5094	-31.5452 (FM)
25	Fe_3AgN	-35.2929	-35.2934	-35.8109	-35.4104	-35.6641	-35.5844	-35.6629
26	Fe_3AlC	-38.3948	-38.3931	-38.4958	-38.4297	-38.4478	-38.3956	-38.4717
27	Fe_3AuN	-36.4848	-36.4891	-36.9848	-36.7654	-36.8544	-36.7527	-36.7971
28	Fe_3InN	-35.5792	-35.5838	-35.8826	-35.7859	-35.7600	-35.7186	-35.7398
29	Fe_3GaN	-36.6713	-36.6791	-36.8257	-36.7347	-36.7334	-36.6342	-36.7290 (cAFM)
30	Fe_3NiN	-38.2967	-38.2987	-38.8023	-38.5186	-38.5609	-38.4172	-38.6058
31	Fe_3PdN	-38.5393	-38.54	-39.0584	-38.7725	-38.8392	-38.6472	-38.8253
32	Fe_3PtN	-41.6476	-41.6557	-42.1517	-41.7493	-41.9643	-41.7505	-41.9203
33	Fe_3RhN	-40.4095	-40.4092	-40.8109	-40.6339	-40.6926	-40.4959	-40.6601
34	Fe_3SnN	-36.9627	-36.9707	-37.0554	-37.0475	-37.0344	-36.9530	-36.9964 (cAFM)
35	Fe_3ZnC	-34.572	-34.5712	-34.9983	-34.8561	-34.8720	-34.8363	-34.8045
36	Fe_3ZnN	-34.4532	-34.451	-34.7846	-34.7131	-34.6959	-34.6729	-34.7366
37	Mn_3AlC	-40.6746	-40.6759	-40.8369	-40.7411	-40.8729	-40.7500	-40.8352
38	Mn_3AlN	-40.814	-40.8162	-40.8669	-40.8016	-40.8008	-40.8170	-40.8073
39	Mn_3GaC	-39.5474	-39.5513	-39.6182	-39.4823	-39.6752	-39.5541	-39.6479
40	Mn_3InC	-38.632	-38.6358	-38.6486	-38.6020	-38.7221	-38.5563	-38.6690
41	Mn_3SnC	-40.1201	-40.1276	-40.1238	-40.0502	-40.0701	-40.1165	-40.1067
	Continued	on the	next	page				

No.	Cmpds.	Γ_{4g}	Γ_{5g}	FM	cAFM-1	cAFM-2	cAFM-3	M-1
42	Mn_3ZnC	-37.2127	-37.2132	-37.4072	-37.2372	-37.3802	-37.2126	-37.3195
43	Ni_3CuN	-28.5426	-28.5421	-28.5454	-28.5419	-28.5424	-28.5422	-28.5445
44	Co_3AuN	-32.4956	-32.4956	-32.8302	-32.6535	-32.6004	-32.5526	-32.8309
45	Co_3GaN	-32.9898	-32.9906	-33.0998	-33.0145	-33.0376	-33.0183	-33.0954 (FM)
46	Co_3LiN	-31.5237	-31.524	-31.6199	-31.5871	-31.5718	-31.5195	-31.6008 (FM)
47	Co_3PdN	-34.4021	-34.4017	-34.8368	-34.5951	-34.5396	-34.4296	-34.8331 (FM)
48	Co_3PtN	-37.355	-37.3623	-37.7702	-37.5283	-37.4931	-37.3626	-37.7671 (FM)
49	Co_3RhN	-36.0835	-36.0838	-36.4937	-36.1917	-36.1869	-36.0658	-36.2779
50	Co_3SnN	-33.231	-33.2294	-33.3208	-33.2465	-33.2466	-33.2501	-33.3218 (FM)
51	Co_3ZnN	-30.9974	-30.998	-31.064	-31.0423	-31.0214	-30.9895	-31.0013
52	Fe_3CuN	-36.6546	-36.4989	-36.8915	-36.7889	-36.8764	-36.7484	-36.7501
53	Fe_3IrN	-42.1038	-42.1034	-42.4219	-42.3595	-42.4072	-42.1830	-42.3073
54	Ni_3LiC	-27.8376	-27.8377	-27.8492	-27.8375	-27.8373	-27.8367	-27.8492

9.3.7 Energy difference ΔE_{tot} between Γ_{5g} and Γ_{4g}

Table 9.7: The total energy difference (ΔE_{tot}) between Γ_{5g} and Γ_{4g} is summarized, where positive and negative ΔE_{tot} values indicate Γ_{4g} and Γ_{5g} magnetic ground state, respectively. The text highlighted in blue indicates the phase transition ($\Gamma_{4g} \leftrightarrow \Gamma_{5g}$) under the given biaxial strain. All energies are given in meV/atom

M_3XN	Compressive -1.0%	Compressive -0.5%	Unstrained 0.0%	Tensile 0.5%	Tensile 1.0%
Cr_3IrN	0.477	0.474	0.437	0.483	0.494
Cr_3PtN	0.633	0.626	0.574	0.592	0.557
Mn_3AgN	0.071	0.023	0.013	0.029	0.066
Mn_3AuN	0.358	0.127	-0.334	-0.405	-0.633
Mn_3CoN	-0.438	0.130	0.244	0.235	0.269
Mn_3HgN	-0.382	-0.439	-0.310	-0.427	-0.459
Mn_3InN	-0.069	-0.091	-0.370	-0.133	0.067
Mn_3IrN	2.247	2.361	2.110	2.435	2.382
Mn_3NiN	0.066	0.050	0.029	0.001	0.025
Mn_3PdN	0.035	0.020	0.071	0.006	-0.014
Mn_3PtN	-1.253	-1.290	-0.994	-1.301	-1.296
Mn_3RhN	0.384	0.319	0.340	0.318	0.395
Mn_3ZnN	-0.233	-0.139	-0.290	-0.062	0.005

9.3.8 Magnetic space group, AHC and ANC tensors for non-collinear APs

Table 9.8: The magnetic space group, AHC tensors, and ANC tensors for cubic Γ_{5g}, cubic Γ_{4g}, tetragonal Γ_{5g} (under biaxial strain), and tetragonal Γ_{4g} (under biaxial strain) configurations of non-collinear antiferromagnetic APs are summarized. The AHC and ANC components can be represented as ($\sigma_{yz} = \sigma_x$, $\sigma_{zx} = \sigma_y$, and $\sigma_{xy} = \sigma_z$) and ($\alpha_{yz} = \alpha_x$, $\alpha_{zx} = \alpha_y$, and $\alpha_{xy} = \alpha_z$) tensors, respectively. In the case of cubic Γ_{4g}, $\sigma_{xy} = \sigma_{yz} = \sigma_{zx}$, and for tetragonal Γ_{5g}, $\sigma_{zx} = \sigma_{zy}$, for tetragonal Γ_{4g}, $\sigma_{xy} = \sigma_{yz} = \sigma_{zx}$, and the same applies to ANC (α).

Magnetic configuration	**Magnetic space group**	**AHC tensor**	**ANC tensor**
Cubic Γ_{5g}	R$\bar{3}$m (166.97)	$\begin{bmatrix} 0 & 0 & 0 \\ 0 & 0 & 0 \\ 0 & 0 & 0 \end{bmatrix}$	$\begin{bmatrix} 0 & 0 & 0 \\ 0 & 0 & 0 \\ 0 & 0 & 0 \end{bmatrix}$
Cubic Γ_{4g}	R$\bar{3}$m$'$ (166.101)	$\begin{bmatrix} 0 & \sigma_{xy} & -\sigma_{xy} \\ -\sigma_{xy} & 0 & \sigma_{xy} \\ \sigma_{xy} & -\sigma_{xy} & 0 \end{bmatrix}$	$\begin{bmatrix} 0 & \alpha_{xy} & -\alpha_{xy} \\ -\alpha_{xy} & 0 & \alpha_{xy} \\ \alpha_{xy} & -\alpha_{xy} & 0 \end{bmatrix}$
Tetragonal Γ_{5g}	C2/m (12.58)	$\begin{bmatrix} 0 & 0 & -\sigma_{zx} \\ 0 & 0 & -\sigma_{zx} \\ \sigma_{zx} & \sigma_{zx} & 0 \end{bmatrix}$	$\begin{bmatrix} 0 & 0 & -\alpha_{zx} \\ 0 & 0 & -\alpha_{zx} \\ \alpha_{zx} & \alpha_{zx} & 0 \end{bmatrix}$
Tetragonal Γ_{4g}	C2$'$/m$'$ (12.62)	$\begin{bmatrix} 0 & \sigma_{xy} & -\sigma_{zx} \\ -\sigma_{xy} & 0 & \sigma_{zx} \\ \sigma_{zx} & -\sigma_{zx} & 0 \end{bmatrix}$	$\begin{bmatrix} 0 & \alpha_{xy} & -\alpha_{zx} \\ -\alpha_{xy} & 0 & \alpha_{zx} \\ \alpha_{zx} & -\alpha_{zx} & 0 \end{bmatrix}$

9.3.9 Magnetic space group, AHC and ANC tensors for FM APs

Table 9.9: The magnetic space group, AHC tensors, and ANC tensors for ferromagnetic [001], [110], and [111] directions are summarized. The AHC and ANC components can be represented as ($\sigma_{yz} = \sigma_x$, $\sigma_{zx} = \sigma_y$, and $\sigma_{xy} = \sigma_z$) and ($\alpha_{yz} = \alpha_x$, $\alpha_{zx} = \alpha_y$, and$_{xy} = \alpha_z$) tensors, respectively. In the case of [110] direction, $\sigma_{zx} = \sigma_{zy}$, and for [111] direction, $\sigma_{xy} = \sigma_{yz} = \sigma_{zx}$, and the same applies to ANC (α).

FM directions	**Magnetic space group**	**AHC tensor**	**ANC tensor**
[001]	P4/mm′m′ (123.345)	$\begin{bmatrix} 0 & \sigma_{xy} & 0 \\ -\sigma_{xy} & 0 & 0 \\ 0 & 0 & 0 \end{bmatrix}$	$\begin{bmatrix} 0 & \alpha_{xy} & 0 \\ -\alpha_{xy} & 0 & 0 \\ 0 & 0 & 0 \end{bmatrix}$
[110]	Cmm′m′ (65.486)	$\begin{bmatrix} 0 & 0 & \sigma_{zx} \\ 0 & 0 & \sigma_{zx} \\ -\sigma_{zx} & -\sigma_{zx} & 0 \end{bmatrix}$	$\begin{bmatrix} 0 & 0 & \alpha_{zx} \\ 0 & 0 & \alpha_{zx} \\ -\alpha_{zx} & -\alpha_{zx} & 0 \end{bmatrix}$
[111]	R$\bar{3}$m′ (166.101)	$\begin{bmatrix} 0 & \sigma_{xy} & -\sigma_{xy} \\ -\sigma_{xy} & 0 & \sigma_{xy} \\ \sigma_{xy} & -\sigma_{xy} & 0 \end{bmatrix}$	$\begin{bmatrix} 0 & \alpha_{xy} & -\alpha_{xy} \\ -\alpha_{xy} & 0 & \alpha_{xy} \\ \alpha_{xy} & -\alpha_{xy} & 0 \end{bmatrix}$

9.3.10 Comparison of AHC with previous studies

Table 9.10: The comparison of AHC σ_{xy} component (S/cm) with the previously reported study from Gurung *et al.*, [59] Huyen *et al.*, [75], Zhou *et al.* [213], and Boldrin *et al.* [15] is summarized. The AHC values reported by Huyen *et al.* and Zhou *et al.* are converted into AHC of σ_{xy} component using the following equation: $\sigma_{xy} = \sigma_{111}/\sqrt{3}$.

Compounds	Our study	Gurung *et al.*	Huyen *et al.*	Zhou *et al.*	Boldrin *et al.*
Mn_3AgN	-106			-207	
Mn_3GaN	-60	-40	56	-57	
Mn_3NiN	-165	130	216	-174	-170
Mn_3IrN	90		-332		
Mn_3PdN	-60		146		
Mn_3SnN	106	133	-74		

9.3.11 Comparison of AHC and ANC between FM and non-collinear AFM

Table 9.11: The AHC and ANC of antiperovskites are listed at the Fermi-energy for the different magnetic configurations ferromagnetic ([001], [110], and [111]) and non-collinear antiferromagnetic (Γ_{4g}). The ANC is calculated at 300 K. The blue text corresponds to the AHC and ANC values in their magnetic ground state.

Compounds	AHC (S/cm)				ANC (A/mK)			
	[001]	[110]	[111]	Γ_{4g}	[001]	[110]	[111]	Γ_{4g}
Co_3PtN	710	558	755	1465	6.31	4.41	3.81	-2.66
Co_3ZnN	930	1039	1068	65	-3.24	-4.65	-4.97	1.07
Cr_3IrN	135	252	173	722	0.88	1.66	1.16	-3.24
Mn_3NiN	-117	-152	-135	-503	0.007	0.73	0.38	1.99

9.3.12 Comparison of ANC with reported study

Table 9.12: The list of APs reported in a recent study [137] provided the maximum ANC (α_z) values calculated at the Fermi energy below 500 K, whereas our ANC calculations were performed at 300 K.

List of reported antiperovskites				
S.No.	Compounds	Materials Project ID	Reported ANC [137] (A/mK)	Our study (A/mK)
1.	Co_3SnC	mp-20679	1.981	-0.82
2.	Co_3ZnC	mp-10271	0.315	-0.37
3.	Fe_3AlC	mp-4593	0.936	-0.51
4.	Fe_3NiN	mp-510381	1.992	-0.014
5.	Fe_3PdN	mp-16334	1.309	-0.22
6.	Fe_3PtN	mp-579496	0.815	1.28
7.	Fe_3RhN	mp-580234	1.352	-1.40
8.	Fe_3ZnC	mp-10266	1.566	-0.81
9.	Mn_3AlC	mp-4593	0.936	-0.37

9.3.13 AHC and ANC of FM APs

Table 9.13: The Compilation AHC and ANC values of the AP compounds at the Fermi-energy. The ANC is calculated at 300 K.

S.No.	M_3XZ Compounds	AHC (S/cm) [001]	[110]	[111]	ANC (A/mK) [001]	[110]	[111]
(1)	Co_3AuN	480.2	534.9	548.5	0.97	-0.62	-0.33
(2)	Co_3CdN	785.9	751.2	604.4	-3.27	-3.39	-3.90
(3)	Co_3CuN	349.3	570.8	593.1	2.84	3.31	2.33
(4)	Co_3GaN	559.2	529.2	536.2	-1.31	-1.31	-1.27
(5)	Co_3GeC	72.9	129.0	152.8	-0.87	-1.35	-1.20
(6)	Co_3GeN	231.7	331.3	348.4	-1.26	-2.32	-3.33
(7)	Co_3InN	482.6	474.8	470.0	-0.57	-0.08	-0.006
(8)	Co_3LiN	878.8	126.4	1127.6	-1.72	0.43	-3.03
(9)	Co_3MgC	283.4	288.8	-290.8	-0.57	-0.19	0.05
(10)	Co_3PdN	158.6	190.6	241.6	0.90	0.46	0.25
(11)	Co_3PtN	710.4	558.4	755.4	6.31	4.41	3.81
(12)	Co_3RhN	-116.1	243.7	258.7	-0.52	0.48	0.49
(13)	Co_3SnC	-51.7	166.3	22.3	-0.82	-1.13	-1.49
(14)	Co_3SnN	-0.03	32.3	48.2	-2.62	-2.77	-2.39
(15)	Co_3ZnC	209.4	-280.7	266.4	-0.37	-0.002	0.17
(16)	Co_3ZnN	930.4	1039.7	1068.4	-3.24	-4.65	-4.97
(17)	Fe_3AgN	189.4	364.9	283.1	1.12	2.17	2.38
(18)	Fe_3AlC	-135.8	-0.94	33.7	-0.036	-0.021	-0.14
(19)	Fe_3AuN	514.7	603.2	626.4	1.19	0.40	1.08
(20)	Fe_3CuN	630.1	852.7	883.0	-0.07	1.35	1.52
(21)	Fe_3GaN	262.2	242.1	215.4	2.53	2.65	2.63
(22)	Fe_3InN	491.1	411.9	376.3	0.34	0.48	0.92
(23)	Fe_3IrN	852.0	719.3	888.1	-0.62	-2.17	-1.64
(24)	Fe_3NiN	286.1	402.9	29.5	-0.01	-0.35	0.10
(25)	Fe_3PdN	361.9	517.0	559.5	-0.22	-0.51	0.01
(26)	Fe_3PtN	-401.6	-445.1	-510.2	1.28	0.60	0.91
(27)	Fe_3RhN	170.6	124.5	134.2	-1.40	-2.01	-2.77
(28)	Fe_3SnN	123.9	161.8	185.1	-1.63	-0.92	-1.05
(29)	Fe_3ZnC	63.5	119.6	181.2	-0.81	-1.43	-0.77
(30)	Fe_3ZnN	-94.2	-75.0	-14.4	-1.43	-0.50	0.15
(31)	Mn_3AlC	199.4	188.2	199.8	-0.51	-0.77	-0.84
(32)	Mn_3AlN	51.4	72.0	68.9	-1.14	-1.06	-1.12
(33)	Mn_3InC	434.9	287.9	235.6	1.97	1.77	1.52
(34)	Ni_3CuC	254.4	-251.6	257.7	1.08	-1.82	2.02
(35)	Ni_3LiC	265.8	262.1	245.0	4.09	5.39	5.81

Bibliography

[1] Björn Alling, Tobias Marten, and IA Abrikosov. "Effect of magnetic disorder and strong electron correlations on the thermodynamics of CrN". In: *Physical Review B* 82.18 (2010), p. 184430.

[2] Vladimir Antropov, Liqin Ke, and Daniel Åberg. "Constituents of magnetic anisotropy and a screening of spin–orbit coupling in solids". In: *Solid State Commun.* 194 (2014), pp. 35–38.

[3] Tomoya Asaba et al. "Colossal anomalous Nernst effect in a correlated noncentrosymmetric kagome ferromagnet". In: *Science Advances* 7.13 (2021), eabf1467.

[4] K Asano, K Koyama, and K Takenaka. "Magnetostriction in Mn_3CuN". In: *Applied Physics Letters* 92.16 (2008), p. 161909.

[5] J Paul Attfield. "Mechanisms and Materials for NTE". In: *Frontiers in chemistry* 6 (2018), p. 371.

[6] CK Barman et al. "Topologically nontrivial phase in the hexagonal antiperovskites A_3BiB (A= Ba, Sr; B= P, N)". In: *Physical Review B* 98.24 (2018), p. 245149.

[7] Gerrit EW Bauer, Eiji Saitoh, and Bart J Van Wees. "Spin caloritronics". In: *Nature materials* 11.5 (2012), pp. 391–399.

[8] Sebastian Beckert et al. "Anomalous Nernst effect in Mn_3NiN thin films". In: *arXiv preprint arXiv:2212.02129* (2022).

[9] *Bilbao Crystallographic Server*. `https://www.cryst.ehu.es/cgi-bin/cryst/programs/nph-magtrgen?gnum=123.345`.

[10] *Bilbao Crystallographic Server*. `https://www.cryst.ehu.es/cgi-bin/cryst/programs/nph-magtrgen?gnum=65.486`.

[11] *Bilbao Crystallographic Server*. `https://www.cryst.ehu.es/cgi-bin/cryst/programs/nph-magtrgen?gnum=166.101`.

[12] *Bilbao Crystallographic Server*. `https://www.cryst.ehu.es/cgi-bin/cryst/programs/nph-magtrgen?gnum=166.97`.

[13] *Bilbao Crystallographic Server*. `https://www.cryst.ehu.es/cgi-bin/cryst/programs/nph-magtrgen?gnum=12.62`.

[14] *Bilbao Crystallographic Server*. `https://www.cryst.ehu.es/cgi-bin/cryst/programs/nph-magtrgen?gnum=12.58`.

[15] David Boldrin et al. "Anomalous Hall effect in noncollinear antiferromagnetic Mn_3NiN thin films". In: *Physical Review Materials* 3.9 (2019), p. 094409.

[16] David Boldrin et al. "Barocaloric properties of quaternary Mn_3(Zn, In)N for room-temperature refrigeration applications". In: *Physical Review B* 104.13 (2021), p. 134101.

[17] David Boldrin et al. "Giant piezomagnetism in Mn_3NiN". In: *ACS applied materials & interfaces* 10.22 (2018), pp. 18863–18868.

[18] David Boldrin et al. "Multisite exchange-enhanced barocaloric response in Mn_3NiN". In: *Physical Review X* 8.4 (2018), p. 041035.

[19] H Boller. "Komplexcarbide und-nitride mit aufgefulltem U3Si-Typ". In: *Monatshefte fur Chemie/Chemical Monthly* 99 (1968), pp. 2444–2449.

[20] H Boller and H Nowotny. "Komplexcarbide und-nitride mit aufgefülltem Re_3B-Typ". In: *Monatshefte für Chemie-Chemical Monthly* 99.2 (1968), pp. 721–725.

[21] Stephen R Boona, Roberto C Myers, and Joseph P Heremans. "Spin caloritronics". In: *Energy & Environmental Science* 7.3 (2014), pp. 885–910.

[22] Max Born. "On the stability of crystal lattices. I". In: *Mathematical Proceedings of the Cambridge Philosophical Society*. Vol. 36. 2. Cambridge University Press. 1940, pp. 160–172.

[23] Max Born, Kun Huang, and M Lax. "Dynamical theory of crystal lattices". In: *American Journal of Physics* 23.7 (1955), pp. 474–474.

[24] Jean-Pierre Bouchaud. "Propriétés Magneétiques et Structurales des Carbonitrures de Manganése et des Perowskites Mn_3GaC et Mn_3GaN". In: *Ann. Chim. France* 3 (1968), pp. 81–105.

[25] Jens Burghaus, Julian Kleemann, and Richard Dronskowski. "The Ternary Nitrides $In_xFe_{4-x}N$ (0<x<0.8): Synthesis, Magnetic Properties, and Theoretical Considerations". In: *Zeitschrift für anorganische und allgemeine Chemie* 637 (2011), pp. 935–939.

[26] AA Burkov. "Anomalous Hall effect in Weyl metals". In: *Physical Review Letters* 113.18 (2014), p. 187202.

[27] WH Cao et al. "Preparation and properties of antiperovskite-type nitrides: $InNNi_3$ and $InNCo_3$". In: *Journal of Solid State Chemistry* 182.12 (2009), pp. 3353–3357.

[28] Luis Casillas-Trujillo, Rickard Armiento, and Björn Alling. "Identification of materials with strong magnetostructural coupling using computational high-throughput screening". In: *Physical Review Materials* 5.3 (2021), p. 034417.

[29] Laurent Chaput et al. "Phonon-phonon interactions in transition metals". In: *Physical Review B* 84.9 (2011), p. 094302.

[30] Hua Chen, Qian Niu, and Allan H MacDonald. "Anomalous Hall effect arising from noncollinear antiferromagnetism". In: *Physical Review Letters* 112.1 (2014), p. 017205.

[31] Jun Chen et al. "Negative thermal expansion in functional materials: controllable thermal expansion by chemical modifications". In: *Chemical Society Reviews* 44.11 (2015), pp. 3522–3567.

[32] Taishi Chen et al. "Large anomalous Nernst effect and nodal plane in an iron-based kagome ferromagnet". In: *Science advances* 8.2 (2022), eabk1480.

[33] Luca Cirillo, Adriana Greco, and Claudia Masselli. "Cooling Through Barocaloric Effect: A Review of the State of the Art Up To 2022". In: *Thermal Science and Engineering Progress* (2022), p. 101380.

[34] Muneyuki Date, Junjiro Kanamori, and Masashi Tachiki. "Origin of magnetoelectric effect in Cr_2O_3". In: *Journal of the Physical Society of Japan* 16.12 (1961), pp. 2589–2589.

[35] RS De Figueiredo, CA Kuhnen, and AV Dos Santos. "Crystallographic, magnetic and electronic structure of iron-silver and iron-gold perovskite nitrides". In: *Journal of magnetism and magnetic materials* 173.1-2 (1997), pp. 141–154.

[36] Sihao Deng et al. "Frustrated triangular magnetic structures of Mn_3ZnN: applications in thermal expansion". In: *The Journal of Physical Chemistry C* 119.44 (2015), pp. 24983–24990.

[37] Sihao Deng et al. "The evolution of magnetic transitions, negative thermal expansion and unusual electronic transport properties in $Mn_3Ag_xMn_yN$". In: *Solid State Communications* 222 (2015), pp. 37–41.

[38] Volker L Deringer, Andrei L Tchougréeff, and Richard Dronskowski. "Crystal orbital Hamilton population (COHP) analysis as projected from plane-wave basis sets". In: *The journal of physical chemistry A* 115.21 (2011), pp. 5461–5466.

[39] ET Dias et al. “Effect of local structural distortions on magnetostructural transformation in Mn_3SnC”. In: *Journal of Physics D: Applied Physics* 48.29 (2015), p. 295001.

[40] WJ Feng et al. “Structure, magnetic and electrical transport properties of Mn4-xAgxN compounds.” In: *Materials Science (0137-1339)* 27.2 (2009).

[41] Manfred Fiebig et al. “The evolution of multiferroics”. In: *Nature Reviews Materials* 1.8 (2016), pp. 1–14.

[42] Debra Anne Fleming, David Wilfred Johnson Jr, and Paul Joseph Lemaire. *Article comprising a temperature compensated optical fiber refractive index grating*. US Patent 5,694,503. 1997.

[43] L Flórez-Gómez, W Ibarra-Hernández, and AC Garcia-Castro. “Lattice dynamics and spin–phonon coupling in the noncollinear antiferromagnetic antiperovskite Mn_3NiN”. In: *Journal of Magnetism and Magnetic Materials* 562 (2022), p. 169813.

[44] V Franco et al. “The magnetocaloric effect and magnetic refrigeration near room temperature: materials and models”. In: *Annual Review of Materials Research* 42 (2012), pp. 305–342.

[45] D Fruchart and E F. Bertaut. “Magnetic studies of the metallic perovskite-type compounds of manganese”. In: *Journal of the physical society of Japan* 44.3 (1978), pp. 781–791.

[46] D Fruchart et al. “Structure magnetique de Mn_3GaC”. In: *Solid State Communications* 8.2 (1970), pp. 91–99.

[47] D Fruchart et al. “Structure magnetique et rotation de spin de Mn_3NiN”. In: *Solid State Communications* 9.21 (1971), pp. 1793–1797.

[48] D Fruchart et al. “The non-collinear component in the magnetic structure of Mn_4N”. In: *Journal of Physics F: Metal Physics* 9.12 (1979), p. 2431.

[49] Daniel Fruchart et al. “Magnetic studies on the metallic perovskite-type compound Mn_3SnN”. In: *Journal de Physique Lettres* 38.1 (1977), pp. 21–23.

[50] Yankun Fu, Shuai Lin, and Bosen Wang. “High-temperature soft magnetic properties of antiperovskite nitrides $ZnNFe_3$ and $AlNFe_3$”. In: *Journal of Magnetism and Magnetic Materials* 378 (2015), pp. 54–58.

[51] Qiang Gao, Ingo Opahle, and Hongbin Zhang. “High-throughput screening for spin-gapless semiconductors in quaternary Heusler compounds”. In: *Physical Review Materials* 3.2 (2019), p. 024410.

[52] Paolo Giannozzi et al. “QUANTUM ESPRESSO: a modular and open-source software project for quantum simulations of materials”. In: *Journal of physics: Condensed matter* 21.39 (2009), p. 395502.

[53] Daniel Gosálbez-Martínez, Ivo Souza, and David Vanderbilt. “Chiral degeneracies and Fermi-surface Chern numbers in bcc Fe”. In: *Physical Review B* 92.8 (2015), p. 085138.

[54] Y Goto, A Daisley, and JSJ Hargreaves. “Towards anti-perovskite nitrides as potential nitrogen storage materials for chemical looping ammonia production: Reduction of Co_3ZnN, Ni_3ZnN, Co_3InN and Ni_3InN under hydrogen”. In: *Catalysis Today* 364 (2021), pp. 196–201.

[55] F Grandjean and A Gerard. “Study by Mossbauer spectroscopy of the series of perovskite carbides $M_3M'C$ with M= Fe or Mn, and M’= Al, Ga, Ge, Zn, Sn”. In: *Journal of Physics F: Metal Physics* 6.3 (1976), p. 451.

[56] Göran Grimvall et al. “Lattice instabilities in metallic elements”. In: *Reviews of Modern Physics* 84.2 (2012), p. 945.

[57] Satya N Guin et al. “Anomalous Nernst effect beyond the magnetization scaling relation in the ferromagnetic Heusler compound Co_2MnGa”. In: *NPG Asia materials* 11.1–9 (2019), pp. 11–16.

[58] Gautam Gurung, Ding-Fu Shao, and Evgeny Y Tsymbal. “Extraordinary Tunneling Magnetoresistance in Antiferromagnetic Tunnel Junctions with Antiperovskite Electrodes”. In: *arXiv preprint arXiv:2306.03026* (2023).

[59] Gautam Gurung et al. “Anomalous Hall conductivity of noncollinear magnetic antiperovskites”. In: *Physical Review Materials* 3.4 (2019), p. 044409.

[60] SV Halilov et al. “Magnetocrystalline anisotropy energy in cubic Fe, Co, and Ni: Applicability of local-spin-density theory reexamined”. In: *Physical Review B* 57.16 (1998), p. 9557.

[61] Huimin Han et al. “Sign reversal of the anomalous Hall effect in antiperovskite (110)-oriented Mn3.19Ga0.81N1-δ film”. In: *Journal of Applied Physics* 132.23 (2022), p. 233902.

[62] Bing He et al. “$CuNNi_3$: a new nitride superconductor with antiperovskite structure”. In: *Superconductor Science and Technology* 26.12 (2013), p. 125015.

[63] Bing He et al. “Preparation and physical properties of antiperovskite-type compounds CdNCo3-zNiz(0$\leq$ z$\leq$ 3)”. In: *Journal of Solid State Chemistry* 184.8 (2011), pp. 1939–1945.

[64] T He et al. “Superconductivity in the non-oxide perovskite $MgCNi_3$”. In: *Nature* 411.6833 (2001), pp. 54–56.

[65] Daigorou Hirai et al. “Synthesis of anti-perovskite-type carbides and nitrides from metal oxides and melamine”. In: *RSC advances* 8.73 (2018), pp. 42025–42031.

[66] Atsufumi Hirohata et al. “Review on spintronics: Principles and device applications”. In: *Journal of Magnetism and Magnetic Materials* 509 (2020), p. 166711.

[67] Andreas Houben, Jens Burghaus, and Richard Dronskowski. “The ternary nitrides $GaFe_3N$ and $AlFe_3N$: Improved synthesis and magnetic properties”. In: *Chemistry of Materials* 21.18 (2009), pp. 4332–4338.

[68] Andreas Houben et al. “Itinerant Ferromagnet $RhFe_3N$: Advanced Synthesis and 57Fe Mössbauer Analysis”. In: *Chemistry of Materials* 21.5 (2009), pp. 784–788.

[69] Andreas Houben et al. “Synthesis, crystal structure, and magnetic properties of the semihard itinerant ferromagnet $RhFe_3N$”. In: *Angewandte Chemie International Edition* 44.44 (2005), pp. 7212–7215.

[70] Timothy H Hsieh, Junwei Liu, and Liang Fu. “Topological crystalline insulators and Dirac octets in antiperovskites”. In: *Physical Review B* 90.8 (2014), p. 081112.

[71] Dan Huang et al. “Carbon deficiency-induced changes of structure and magnetism of Mn_3SnC”. In: *Journal of materials science* 55 (2020), pp. 8363–8375.

[72] Zhenzhen Hui et al. “Self-assembled c-axis oriented antiperovskite soft-magnetic $CuNCo_3$ thin films by chemical solution deposition”. In: *Journal of Materials Chemistry C* 3.17 (2015), pp. 4438–4444.

[73] Leo J Hüiter and Hans H Stadelmaier. “Über ternäre Karbide der T-Metalle Nickel, Kobalt, Eisen und Mangan mit Germanium und Indium”. In: *International Journal of Materials Research* 50.4 (1959), pp. 199–203.

[74] Leo J Hütter and HH Stadelmaier. “Ternary carbides of transition metals with aluminum and magnesium”. In: *Acta Metallurgica* 6.5 (1958), pp. 367–370.

[75] Vu Thi Ngoc Huyen et al. “Topology analysis for anomalous Hall effect in the noncollinear antiferromagnetic states of Mn_3AN (A= Ni, Cu, Zn, Ga, Ge, Pd, In, Sn, Ir, Pt)”. In: *Physical Review B* 100 (9 2019), pp. 094426–094434.

[76] Muhammad Ikhlas et al. “Large anomalous Nernst effect at room temperature in a chiral antiferromagnet”. In: *Nature Physics* 13.11 (2017), pp. 1085–1090.

[77] Hiroki Isobe and Liang Fu. “Quantum critical points of j= 3/2 Dirac electrons in antiperovskite topological crystalline insulators”. In: *Physical Review B* 93.24 (2016), p. 241113.

[78] Shinji Isogami, Koki Takanashi, and Masaki Mizuguchi. “Dependence of anomalous Nernst effect on crystal orientation in highly ordered γ’-Fe_4N films with anti-perovskite structure”. In: *Applied Physics Express* 10.7 (2017), p. 073005.

[79] H Jacobs, D Rechenbach, and U Zachwieja. “Structure determination of γ'-Fe_4N and ϵ-Fe_3N”. In: *Journal of Alloys and Compounds* 227.1 (1995), pp. 10–17.

[80] Anubhav Jain et al. “Commentary: The Materials Project: A materials genome approach to accelerating materials innovation”. In: *APL materials* 1.1 (2013), p. 011002.

[81] Michael B Jakubinek et al. “Temperature excursions at the pulp–dentin junction during the curing of light-activated dental restorations”. In: *Dental Materials* 24.11 (2008), pp. 1468–1476.

[82] F Johnson et al. “Identifying the octupole antiferromagnetic domain orientation in Mn_3NiN by scanning anomalous Nernst effect microscopy”. In: *Applied Physics Letters* 120.23 (), p. 232402.

[83] F Johnson et al. “Strain dependence of Berry-phase-induced anomalous Hall effect in the non-collinear antiferromagnet Mn3NiN”. In: *Applied Physics Letters* 119.22 (2021), p. 222401.

[84] Kenji Kamishima et al. “Magnetic behavior of Mn_3GaC under high magnetic field and high pressure”. In: *Journal of the Physical Society of Japan* 67.5 (1998), pp. 1748–1754.

[85] Kenji Kamishima et al. “Pressure Induced Magnetic Transition of Mn3Ga1-xAlxC”. In: *Journal of the Physical Society of Japan* 71.3 (2002), pp. 922–926.

[86] Takejiro Kaneko, Takeshi Kanomata, and Kiwamu Shirakawa. “Pressure effect on the magnetic transition temperatures in the intermetallic compounds Mn_3MC (M= Ga, Zn and Sn)”. In: *Journal of the Physical Society of Japan* 56.11 (1987), pp. 4047–4055.

[87] T Kanomata, T Kaneko, and Y Nakagawa. “Magnetic properties of the intermetallic compound Mn_3InC”. In: *Journal of Solid State Chemistry* 96.2 (1992), pp. 451–454.

[88] T Kanomata, H Yasui, and T Kaneko. “Thermal expansion and Pressure Effect on the Curie temperature of Mn_3InC”. In: *physica status solidi (a)* 126.1 (1991), K83–k86.

[89] Akihiro Kenmotsu, Takeshi Shinohara, and Hiroshi Watanabe. “Nuclear magnetic resonance of ferromagnetic Mn_3AlC and Mn_3GaC”. In: *Journal of the Physical Society of Japan* 32.2 (1972), pp. 377–381.

[90] T Kikkawa et al. “Separation of longitudinal spin Seebeck effect from anomalous Nernst effect: Determination of origin of transverse thermoelectric voltage in metal/insulator junctions”. In: *Physical Review B* 88.21 (2013), p. 214403.

[91] WS Kim et al. “Close correlation among lattice, spin, and charge in the manganese-based antiperovskite material”. In: *Solid state communications* 119.8-9 (2001), pp. 507–510.

[92] Georg Kresse and Jürgen Furthmüller. “Efficiency of ab-initio total energy calculations for metals and semiconductors using a plane-wave basis set”. In: *Computational materials science* 6.1 (1996), pp. 15–50.

[93] Georg Kresse and Jürgen Furthmüller. “Efficient iterative schemes for ab initio total-energy calculations using a plane-wave basis set”. In: *Physical review B* 54.16 (1996), p. 11169.

[94] CA Kuhnen, RS De Figueiredo, and AV Dos Santos. “Mössbauer spectroscopy, crystallographic, magnetic and electronic structure of $ZnFe_3N$ and $InFe_3N$”. In: *Journal of magnetism and magnetic materials* 219.1 (2000), pp. 58–68.

[95] JC Lin et al. “AlN_xMn_3: A possible high-temperature soft magnetic material and strongly correlated system”. In: *Applied Physics Letters* 98.9 (2011), p. 092507.

[96] S Lin et al. “Synthesis and characterization of Ge–Cr-based intermetallic compounds: $GeCr_3$, $GeCCr_3$, and $GeNCr_3$”. In: *Journal of alloys and compounds* 584 (2014), pp. 308–314.

[97] Shuai Lin et al. “Critical behavior in the itinerant ferromagnet $AsNCr_3$ with tetragonal-antiperovskite structure”. In: *Physical Review B* 98.1 (2018), p. 014412.

[98] Shuai Lin et al. “Good thermoelectric performance in strongly correlated system $SnCCo_3$ with antiperovskite structure”. In: *Inorganic chemistry* 53.7 (2014), pp. 3709–3715.

[99] *Linear response symmetry*. `https://bitbucket.org/zeleznyj/linear-response-symmetry/src/master/`.

[100] Chaocheng Liu et al. “Spin-glass behavior in Co-based antiperovskite compound $SnNCo_3$”. In: *Applied Physics Letters* 116.5 (2020), p. 052401.

[101] Enke Liu et al. “Giant anomalous Hall effect in a ferromagnetic kagome-lattice semimetal”. In: *Nature physics* 14.11 (2018), pp. 1125–1131.

[102] X Liu et al. “External control of the direction of magnetization in ferromagnetic InMnAs/GaSb heterostructures”. In: *Physica E: Low-dimensional Systems and Nanostructures* 20.3-4 (2004), pp. 370–373.

[103] Pavel Lukashev, Kirill D Belashchenko, and Renat F Sabirianov. “Large magneto-electric effect in ferroelectric/piezomagnetic heterostructures”. In: *Physical Review B* 84.13 (2011), p. 134420.

[104] Pavel Lukashev, Renat F. Sabirianov, and Kirill Belashchenko. “Theory of the piezomagnetic effect in Mn-based antiperovskites”. In: *Physical Review B* 78 (18 2008), pp. 184414–184418.

[105] Stefan Maintz et al. “LOBSTER: A tool to extract chemical bonding from plane-wave based DFT”. In: *Journal of Computational Chemistry* 37.11 (2016), pp. 1030–1035.

[106] Daichi Matsunami et al. “Giant barocaloric effect enhanced by the frustration of the antiferromagnetic phase in Mn_3GaN”. In: *Nature materials* 14.1 (2015), pp. 73–78.

[107] Daniel Meier et al. “Influence of heat flow directions on Nernst effects in Py/Pt bilayers”. In: *Physical Review B* 88.18 (2013), p. 184425.

[108] Masaki Mizuguchi and Satoru Nakatsuji. “Energy-harvesting materials based on the anomalous Nernst effect”. In: *Science and Technology of Advanced Materials* 20.1 (2019), pp. 262–275.

[109] FR Morral. “The Constitution of Iron-Rich Fe-Al-C Alloys”. In: *Journal Iron and Steel Institute* 130 (1934), p. 419.

[110] Arash A Mostofi et al. “wannier90: A tool for obtaining maximally-localised Wannier functions”. In: *Comput. Phys. Commun.* 178.9 (2008), pp. 685–699.

[111] Felix Mouhat and Franccois-Xavier Coudert. “Necessary and sufficient elastic stability conditions in various crystal systems”. In: *Physical review B* 90.22 (2014), p. 224104.

[112] D Music et al. “Thermal expansion and elasticity of $PdFe_3N$ within the quasiharmonic approximation”. In: *European Physical Journal B* 77.3 (2010), pp. 401–406.

[113] Sigemaro Nagakura, Nobuo Otsuka, and Yoshihiko Hirotsu. “Electron state of Ni_4N studied by electron diffraction”. In: *Journal of the Physical Society of Japan* 35.5 (1973), pp. 1492–1495.

[114] Naoto Nagaosa et al. “Anomalous hall effect”. In: *Reviews of modern physics* 82.2 (2010), p. 1539.

[115] Satoru Nakatsuji, Naoki Kiyohara, and Tomoya Higo. “Large anomalous Hall effect in a non-collinear antiferromagnet at room temperature”. In: *Nature* 527.7577 (2015), pp. 212–215.

[116] M Nardin et al. “Retude de cinq nouveaux nitrures MCr_3N de type perovskite”. In: *Comptes Rendus Hebdomadaires des Seances des Sciences, Serie C, Sciences Chimiques* 274 (1972), pp. 2168–2171.

[117] M Nardin et al. “Six new ternary manganese nitrides. study of first order transitions in complex nitrides and carbides with perowskite structure”. In: *Comptes Rendus Hebdomadaires des Seances des Sciences Serie C Sciences Chimiques* 264 (1967), p. 308.

[118] Alexandra Navrotsky and Donald J Weidner. “Perovskite: a structure of great interest to geophysics and materials science”. In: *Washington DC American Geophysical Union Geophysical Monograph Series* 45 (1989).

[119] Ajaya K Nayak et al. “Large anomalous Hall effect driven by a nonvanishing Berry curvature in the noncolinear antiferromagnet Mn_3Ge”. In: *Science advances* 2.4 (2016), e1501870.

[120] Walther Nernst. “Ueber die electromotorischen Kräfte, welche durch den Magnetismus in von einem Wärmestrome durchflossenen Metallplatten geweckt werden”. In: *Annalen der Physik* 267.8 (1887), pp. 760–789.

[121] Rainer Niewa. “Metal-Rich Ternary Perovskite Nitrides”. In: *European Journal of Inorganic Chemistry* 2019.32 (2019), pp. 3647–3660.

[122] Jonathan Noky et al. “Characterization of topological band structures away from the Fermi level by the anomalous Nernst effect”. In: *Physical Review B* 98 (24 2018), pp. 241106–241110.

[123] Dominik Ohmer. “High-throughput DFT design of MAX compounds”. en. MA thesis. Darmstadt: Technische Universität, 2017.

[124] Dominik Ohmer et al. “High-throughput design of 211-M_2AX compounds”. In: *Physical Review Materials* 3.5 (2019), p. 053803.

[125] Dominik Ohmer et al. “Stability predictions of magnetic M_2AX compounds”. In: *Journal of Physics: Condensed Matter* 31.40 (2019), p. 405902.

[126] Ingo Opahle, Georg KH Madsen, and Ralf Drautz. “High throughput density functional investigations of the stability, electronic structure and thermoelectric properties of binary silicides”. In: *Physical Chemistry Chemical Physics* 14.47 (2012), pp. 16197–16202.

[127] Ingo Opahle et al. "Effect of N, C, and B interstitials on the structural and magnetic properties of alloys with Cu_3Au structure". In: *Physical Review Research* 2.2 (2020), p. 023134.

[128] Mohamed Oudah et al. "Superconductivity in the antiperovskite Dirac-metal oxide $Sr_{3-x}SnO$". In: *Nature communications* 7.1 (2016), pp. 1–6.

[129] Wolfgang Pannhorst. "Glass ceramics: state-of-the-art". In: *Journal of Non-Crystalline Solids* 219 (1997), pp. 198–204.

[130] John P Perdew, Kieron Burke, and Matthias Ernzerhof. "Generalized gradient approximation made simple". In: *Physical Review Letters* 77.18 (1996), p. 3865.

[131] AA Putyatin, VE Davydov, and SN Nesterenko. "High temperature interactions in the Fe-Al-C system at 6 GPa pressure". In: *Journal of alloys and compounds* 179.1-2 (1992), pp. 165–175.

[132] Camilo X Quintela et al. "Epitaxial antiperovskite/perovskite heterostructures for materials design". In: *Science Advances* 6.30 (2020), eaba4017.

[133] Upasana Rani et al. "Emerging potential antiperovskite materials ANX_3 (A= P, As, Sb, Bi; X= Sr, Ca, Mg) for thermoelectric renewable energy generators". In: *Journal of Solid State Chemistry* 300 (2021), p. 122246.

[134] Manuel Richter. *Handbook of magnetic materials (Density Functional Theory applied to 4f and 5f Elements and Metallic Compounds)*. Vol. 13. Elsevier, 2003, pp. 87–228.

[135] Berthold H Rimmler et al. "Atomic Displacements Enabling the Observation of the Anomalous Hall Effect in a Non-Collinear Antiferromagnet". In: *Advanced Materials* (2023), p. 2209616.

[136] Akito Sakai et al. "Giant anomalous Nernst effect and quantum-critical scaling in a ferromagnetic semimetal". In: *Nature physics* 14.11 (2018), pp. 1119–1124.

[137] Akito Sakai et al. "Iron-based binary ferromagnets for transverse thermoelectric conversion". In: *Nature* 581.7806 (2020), pp. 53–57.

[138] Yuya Sakuraba. "Potential of thermoelectric power generation using anomalous Nernst effect in magnetic materials". In: *Scripta Materialia* 111 (2016), pp. 29–32.

[139] Yuya Sakuraba et al. "Anomalous Nernst effect in L10-FePt/MnGa thermopiles for new thermoelectric applications". In: *Applied Physics Express* 6.3 (2013), p. 033003.

[140] Ilias Samathrakis and Hongbin Zhang. "Tailoring the anomalous Hall effect in the noncollinear antiperovskite Mn 3 GaN". In: *Physical Review B* 101.21 (2020), p. 214423.

[141] Ilias Samathrakis et al. “Enhanced anomalous Nernst effects in ferromagnetic materials driven by Weyl nodes”. In: *Journal of Physics D: Applied Physics* 55.7 (2021), p. 074003.

[142] Ch Samson, JP Bouchaud, and R Fruchart. “QUATRE NOUVEAUX NITRURES A STRUCTURE PEROWSKITE-Mn3CuN Mn3AgN Mn3GaN Cr3GaN”. In: *Comptes Rendus Hebdomadaires Des Seances De L academie Des Science* 259.2 (1964), p. 392.

[143] KM Seemann et al. “Origin of the planar Hall effect in nanocrystalline $Co_{60}Fe_{20}B_{20}$”. In: *Physical Review Letters* 107.8 (2011), p. 086603.

[144] Ding-Fu Shao et al. “Electrically reversible magnetization at the antiperovskite/perovskite interface”. In: *Physical Review Materials* 3.2 (2019), p. 024405.

[145] Chen Shen et al. “Designing of magnetic MAB phases for energy applications”. In: *Journal of Materials Chemistry A* 9.13 (2021), pp. 8805–8813.

[146] Kewen Shi et al. “Baromagnetic effect in antiperovskite $Mn_3Ga_{0.95}N_{0.94}$ by neutron powder diffraction analysis”. In: *Advanced Materials* 28.19 (2016), pp. 3761–3767.

[147] Wujun Shi et al. “Prediction of a magnetic Weyl semimetal without spin-orbit coupling and strong anomalous Hall effect in the Heusler compensated ferrimagnet Ti_2MnAl”. In: *Physical Review B* 97.6 (2018), p. 060406.

[148] T Shibayama and K Takenaka. “Giant magnetostriction in antiperovskite Mn_3CuN”. In: *Journal of applied physics* 109.7 (2011), 07A928.

[149] Harish K Singh et al. “Giant anomalous Hall and anomalous Nernst conductivities in antiperovskites and their tunability via magnetic fields”. In: *Physical Review Materials* 6.4 (2022), p. 045402.

[150] Harish K Singh et al. “High-throughput screening of half-antiperovskites with a stacked kagome lattice”. In: *Acta Materialia* 242 (2023), p. 118474.

[151] Harish K Singh et al. “High-throughput screening of magnetic antiperovskites”. In: *Chemistry of Materials* 30.20 (2018), pp. 6983–6991.

[152] Harish K Singh et al. “Multifunctional antiperovskites driven by strong magnetostructural coupling”. In: *npj Computational Materials* 7.1 (2021), p. 98.

[153] Bo Song et al. “Observation of spin-glass behavior in antiperovskite Mn_3GaN”. In: *Applied Physics Letters* 92.19 (2008), p. 192511.

[154] Xiaoyan Song et al. “Adjustable zero thermal expansion in antiperovskite manganese nitride”. In: *Advanced Materials* 23.40 (2011), pp. 4690–4694.

[155] Yuzhu Song et al. “Negative thermal expansion in magnetic materials”. In: *Progress in Materials Science* 121 (2021), p. 100835.

[156] Nicola A Spaldin and Manfred Fiebig. “The renaissance of magnetoelectric multiferroics”. In: *Science* 309.5733 (2005), pp. 391–392.

[157] Hans H Stadelmaier and AC Fraker. *Nitrides of Iron with Nickel, Palladium, and Platinum*. 1960.

[158] Hans H Stadelmaier and LJ Huetter. “Ternary carbides of the transition metals nickel, cobalt, iron, manganese with zinc and tin”. In: *Acta Metallurgica* 7.6 (1959), pp. 415–419.

[159] Hans H Stadelmaier, Leo J Hutter, and Navin C Kothari. “Ueber ternaere Karbide der T-Metalle Nickel, Kobalt, Eisen und Mangan mit Gallium”. In: *International Journal of Materials Research* 51.1 (1960), pp. 41–45.

[160] Harold T Stokes et al. “Group-theoretical analysis of octahedral tilting in ferroelectric perovskites”. In: *Acta Crystallographica Section B: Structural Science* 58.6 (2002), pp. 934–938.

[161] “Structure, magnetic and electronic transport properties in antiperovskite cubic γ'-$CuFe_3N$ polycrystalline films”. In: *Intermetallics* 121 (2020), p. 106779.

[162] Ying Sun et al. “Lattice contraction and magnetic and electronic transport properties of $Mn3Zn1 - xGexN$”. In: *Applied Physics Letters* 91.23 (2007), p. 231913.

[163] Ying Sun et al. “Thermodynamic, electromagnetic, and lattice properties of antiperovskite Mn_3SbN”. In: *Advances in Condensed Matter Physics* 2013 (2013).

[164] YS Sun et al. “Magnetic and electrical properties of antiperovskite Mn_3InN synthesized by a high-pressure method”. In: *Journal of Physics: Conference Series*. Vol. 400. 3. IOP Publishing. 2012, p. 032094.

[165] M-T Suzuki et al. “Cluster multipole theory for anomalous Hall effect in antiferromagnets”. In: *Physical Review B* 95.9 (2017), p. 094406.

[166] Fumiya Takata et al. “Epitaxial growth and magnetic properties of $Ni_xFe_{4-x}N$ (x= 0, 1, 3, and 4) films on $SrTiO_3$ (001) substrates”. In: *Journal of applied physics* 120.8 (2016), p. 083907.

[167] K. Takenaka and H. Takagi. “Giant negative thermal expansion in Ge-doped antiperovskite manganese nitrides”. In: *Appl. Phys. Lett* 87.26 (2005), pp. 261902–261904.

[168] Koshi Takenaka. “Negative thermal expansion materials: technological key for control of thermal expansion”. In: *Science and technology of advanced materials* (2012).

[169] Koshi Takenaka and Hidenori Takagi. “Magnetovolume effect and negative thermal expansion in $Mn_3Cu_{(1-x)}Ge_xN$”. In: *Materials transactions* 47.3 (2006), pp. 471–474.

[170] Koshi Takenaka et al. “Magnetovolume effects in manganese nitrides with antiperovskite structure”. In: *Science and Technology of Advanced Materials* 15.1 (2014), pp. 015009–015019.

[171] Kun Tao et al. “Giant reversible barocaloric effect with low hysteresis in antiperovskite $PdNMn_3$ compound”. In: *Scripta Materialia* 203 (2021), p. 114049.

[172] Atsushi Togo and Isao Tanaka. “First principles phonon calculations in materials science”. In: *Scripta Materialia* 108 (2015), pp. 1–5.

[173] T Tohei, H Wada, and T Kanomata. “Negative magnetocaloric effect at the antiferromagnetic to ferromagnetic transition of Mn_3GaC”. In: *Journal of Applied Physics* 94.3 (2003), pp. 1800–1802.

[174] Peng Tong, Bo-Sen Wang, and Yu-Ping Sun. “Mn-based antiperovskite functional materials: Review of research”. In: *Chinese Physics B* 22.6 (2013), p. 067501.

[175] D Torres-Amaris et al. “Anomalous Hall conductivity control in Mn 3 NiN antiperovskite by epitaxial strain along the kagome plane”. In: *Physical Review B* 106.19 (2022), p. 195113.

[176] Sa Tu et al. “Anomalous Nernst effect in $Ir_22Mn_78/Co_20Fe_60B_20$/MgO layers with perpendicular magnetic anisotropy”. In: *Applied Physics Letters* 111.22 (2017), p. 222401.

[177] Masatomo Uehara et al. “New antiperovskite superconductor ZnNNi3, and related compounds $CdNNi_3$ and $InNNi_3$”. In: *Physica C: Superconductivity and its applications* 470 (2010), S688–S690.

[178] Masatomo Uehara et al. “Superconducting properties of $CdCNi_3$”. In: *Journal of the Physical Society of Japan* 76.3 (2007), p. 034714.

[179] AAMACG Van De Walle, M Asta, and G Ceder. “The alloy theoretic automated toolkit: A user guide”. In: *Calphad* 26.4 (2002), pp. 539–553.

[180] Bosen Wang et al. “Weak ferromagnetism and possible non-Fermi-liquid behavior in the itinerant electronic material Co_3SnC”. In: *Physical Review B* 102.8 (2020), p. 085153.

[181] BS Wang et al. “Large magnetic entropy change near room temperature in antiperovskite $SnCMn_3$”. In: *EPL (Europhysics Letters)* 85.4 (2009), p. 47004.

[182] BS Wang et al. “Observation of spin-glass behavior in antiperovskite compound $SnCFe_3$”. In: *Applied Physics Letters* 97.4 (2010), p. 042508.

[183] BS Wang et al. “Structural, magnetic, electrical transport properties, and reversible room-temperature magnetocaloric effect in antipervoskite compound $AlCMn_3$”. In: *Journal of Applied Physics* 108.9 (2010), p. 093925.

[184] Cong Wang et al. “Tuning the range, magnitude, and sign of the thermal expansion in intermetallic $Mn_3(Zn, M)_xN$ (M= Ag, Ge)”. In: *Physical Review B* 85.22 (2012), p. 220103.

[185] JBNJ Wang et al. “Epitaxial $BiFeO_3$ multiferroic thin film heterostructures”. In: *science* 299.5613 (2003), pp. 1719–1722.

[186] Qi Wang et al. “Large intrinsic anomalous Hall effect in half-metallic ferromagnet $Co_3Sn_2S_2$ with magnetic Weyl fermions”. In: *Nature communications* 9.1 (2018), pp. 1–8.

[187] *Web of Science*. `https://www.webofscience.com/wos/woscc/summary/fd2a4606-fa59-44ca-a264-53b974f8505a-93c15a8e/date-descending/1`.

[188] Jürgen Weischenberg et al. “Ab initio theory of the scattering-independent anomalous Hall effect”. In: *Physical Review Letters* 107.10 (2011), p. 106601.

[189] B Wiendlocha et al. “Electronic structure, superconductivity and magnetism study of Cr_3GaN and Cr_3RhN”. In: *Journal of alloys and compounds* 442.1-2 (2007), pp. 289–291.

[190] George W Wiener and J Aldred Berger. “Structure and magnetic properties of some transition metal nitrides”. In: *JOM* 7 (1955), pp. 360–368.

[191] Meimei Wu et al. “Magnetic structure and lattice contraction in Mn_3NiN”. In: *Journal of Applied Physics* 114.12 (2013).

[192] QuanSheng Wu et al. “WannierTools : An open-source software package for novel topological materials”. In: *Comput. Phys. Commun.* 224 (2018), pp. 405–416. ISSN: 0010-4655.

[193] Christoph Wuttke et al. “Berry curvature unravelled by the anomalous Nernst effect in Mn_3Ge”. In: *Physical Review B* 100.8 (2019), p. 085111.

[194] Wei Xia et al. “Antiperovskite Electrolytes for Solid-State Batteries”. In: *Chemical Reviews* 122.3 (2022), pp. 3763–3819.

[195] Di Xiao, Ming-Che Chang, and Qian Niu. “Berry phase effects on electronic properties”. In: *Rev. Mod. Phys.* 82 (3 2010), pp. 1959–2007.

[196] Di Xiao et al. “Berry-phase effect in anomalous thermoelectric transport”. In: *Physical Review Letters* 97.2 (2006), p. 026603.

[197] Yuanfeng Xu et al. “High-throughput calculations of magnetic topological materials”. In: *Nature* 586.7831 (2020), pp. 702–707.

[198] Haiyang Yang et al. “Giant anomalous Nernst effect in the magnetic Weyl semimetal $Co_3Sn_2S_2$”. In: *Physical Review Materials* 4.2 (2020), p. 024202.

[199] Yugui Yao et al. “First principles calculation of anomalous Hall conductivity in ferromagnetic bcc Fe”. In: *Physical Review Letters* 92.3 (2004), p. 037204.

[200] Linda Ye et al. “Massive Dirac fermions in a ferromagnetic kagome metal”. In: *Nature* 555.7698 (2018), pp. 638–642.

[201] Yunfeng You et al. “Anomalous Nernst Effect in an Antiperovskite Antiferromagnet”. In: *Physical Review Applied* 18.2 (2022), p. 024007.

[202] Yunfeng You et al. “Room temperature anomalous Hall effect in antiferromagnetic Mn_3SnN films”. In: *Applied Physics Letters* 117.22 (2020), p. 222404.

[203] Ming-Hui Yu, LH Lewis, and AR Moodenbaugh. “Large magnetic entropy change in the metallic antiperovskite Mn_3GaC”. In: *Journal of applied physics* 93.12 (2003), pp. 10128–10130.

[204] Rui Yu et al. “Topological node-line semimetal and Dirac semimetal state in antiperovskite Cu_3PdN”. In: *Physical Review Letters* 115.3 (2015), p. 036807.

[205] Jakub Zelezny et al. “High-throughput study of the anomalous Hall effect”. In: *arXiv preprint arXiv:2205.14907* (2022).

[206] J. Zemen, Z. Gercsi, and K. G. Sandeman. “Piezomagnetism as a counterpart of the magnetovolume effect in magnetically frustrated Mn-based antiperovskite nitrides”. In: *Physical Review B* 96 (2 2017), pp. 024451–024458.

[207] Hongbin Zhang, Stefan Blügel, and Yuriy Mokrousov. “Anisotropic intrinsic anomalous Hall effect in ordered 3d Pt alloys”. In: *Physical Review B* 84.2 (2011), p. 024401.

[208] XH Zhang et al. “Magnetoresistance reversal in antiperovskite compound $Mn_3Cu_{0.5}Zn_{0.5}N$”. In: *Journal of Applied Physics* 115.12 (2014), p. 123905.

[209] Yang Zhang et al. “Strong anisotropic anomalous Hall effect and spin Hall effect in the chiral antiferromagnetic compounds Mn_3X (X= Ge, Sn, Ga, Ir, Rh, and Pt)”. In: *Physical Review B* 95.7 (2017), p. 075128.

[210] Zhenjie Zhao et al. “Preparation and Characterization of γ'-Fe_3SnN”. In: *physica status solidi (a)* 174.1 (1999), pp. 249–253.

[211] Jingfeng Zheng, Brian Perry, and Yiying Wu. "Antiperovskite superionic conductors: a critical review". In: *ACS Materials Au* 1.2 (2021), pp. 92–106.

[212] Xiaodong Zhou et al. "Giant anomalous Nernst effect in noncollinear antiferromagnetic Mn-based antiperovskite nitrides". In: *Physical review materials* 4.2 (2020), p. 024408.

[213] Xiaodong Zhou et al. "Spin-order dependent anomalous Hall effect and magneto-optical effect in the noncollinear antiferromagnets Mn_3XN with X= Ga, Zn, Ag, or Ni". In: *Physical Review B* 99 (10 2019), pp. 104428–104440.

[214] L Zu et al. "Synthesis and physical properties of Cr–P-based intermetallic compounds: Cr_3P, Cr_3PC, and Cr_3PN". In: *Journal of Alloys and Compounds* 630 (2015), pp. 310–315.

[215] Lin Zu et al. "Observation of the spin-glass behavior in co-based antiperovskite nitride $GeNCo_3$". In: *Inorganic chemistry* 55.18 (2016), pp. 9346–9351.

[216] Alex Zunger et al. "Special quasirandom structures". In: *Physical Review Letters* 65.3 (1990), p. 353.

[217] Igor Žutić, Jaroslav Fabian, and S Das Sarma. "Spintronics: Fundamentals and applications". In: *Reviews of modern physics* 76.2 (2004), p. 323.